UNIVERSITÀ DEGLI STUDI DI SALERNO

University of Salerno

Department of Chemistry and Biology "A. Zambelli"

Ph.D. course in Chemistry

XXXIII Doctoral Cycle

Ph.D. Thesis in Chemistry:

Elucidation of Crystal Structures and Structural Changes using X-ray Powder Diffraction

Supervisors:
Prof. Consiglia Tedesco
Prof. Robert E. Dinnebier
Dr. Bernd Hinrichsen

PhD Student:
Gianpiero Gallo
Matr. 8800100039

Coordinator:
Prof. Claudio Pellecchia

Academic year 2019/2020

Preface

This PhD thesis is the result of collaboration with the Max Planck Institute for Solid State Research in Stuttgart (Germany) and BASF SE in Ludwigshafen am Rhein (Germany).

Contents

Index of abbreviations

2PPL	Two photon photoluminescence
CNpy	4-cyanopyridine
4PAzP	4-phenylazopyridine
DMABN	4-(dimethylamino) benzonitrile
ABN	4-aminobenzonitrile
acac	Acetylacetonate
ATR	Attenuated total reflection
BPE	4,4'-bipyridylethylene
BSE	Backscattered electrons
btc	1,3,5-benzenetricarboxylate
CBTA	1,2,3,4-cyclobutane-tetracarboxylic acid
CTE	Coefficient of thermal expansion
DFT	Density functional theory
DMF	Dimethylformamide
DTA	Differential thermal analysis
DTG	Derivative thermogravimetry
EDX	Energy dispersive X-ray
FWHM	Full width at half maximum

gly	Glycine
Himd	Imidazole
IR	Infrared
MOF	Metal-organic framework
NCS	Thiocyanate
NLO	Non-linear optics
NTE	Negative thermal expansion
PBU	Primary building unit
PDF	Pair distribution function
PDNB	Poly(1,4-phenylenazine-N,N-dioxide)
PE	Photosalient effect
PHA	(phenylazophenyl)Pd(hexafluoroacetylacetonate)
PTE	Positive thermal expansion
res	Resorcinol
SBU	Secondary building unit
SCR	Selective catalytic reduction
SC-XRD	Single crystal X-ray diffraction
SEM	Scanning electron microscopy
SHG	Second-harmonic generation
SOF	Site occupancy factor
spy	Styrylpyridine
TE	Thermosalient effect
TGA	Thermal gravimetric analysis
UV	Ultraviolet

VTE	Volume thermal expansion
WBG	Wide-bandgap
XRPD	X-ray powder diffraction

Abstract

In the process of understanding the properties and behaviour of a compound, and designing improved materials, probing the atomic-level structure is a decisive step. Single crystal X-ray diffraction, a widespread, non-destructive technique, can certainly satisfy this requirement. However, suitable single crystals cannot always be obtained, especially in cases where compounds are synthesised *in situ* or investigated while they are subjected to external stimuli that can compromise the integrity of the crystal. In these cases, X-ray powder diffraction (XRPD) can be used. This method allows for analysis of the bulk material, regardless of the degree of the structural order in the compound (crystalline or amorphous), and delivers information about the crystal structure, local structure, microstructure, and phase composition.

In the present PhD thesis, several compounds belonging to different classes of materials such as organic molecules, coordination compounds, inorganic compounds, and polymers have been analyzed with the main aim of extracting structural details and determining structural changes. XRPD was used as the main technique, and complementary analyses such as thermal analysis (TGA, DTA, DSC), scanning electron microscopy (SEM), and vibrational spectroscopy (IR) supported the results.

This PhD thesis is divided in six main chapters. In the introduction and in the second chapter, a brief overview of techniques, methods, and instruments, extensively used in this PhD, is given. An illustration of the devices for *in situ* and *operando* experiments, designed and built during this thesis, is also provided.

The third chapter discusses the characterization of two compounds: ferrous glycine sulfate pentahydrate, currently used as an iron supplement, and glycolaldehyde ammonia, recently synthesized in the lab of BASF SE in Ludwigshafen am Rhein (Germany). In both cases, a careful characterization of the morphology by SEM, and the structural details by XRPD and IR were performed. For the first case study, the use of the SEM coupled with BSE and

EDX, confirmed the stoichiometry (Fe:S:N ratio) and showed the presence of heavily scattering particles, attributed to by-products of the synthesis. IR revealed the denticity of the glycine is in the zwitterionic form, and the crystal structure of the iron compound was determined by XRPD analysis. Upon heating, the compound transforms to the anhydrous coordination complex, through a less hydrated crystal form, as observed by TGA/DTA analysis and temperature dependent *in situ* XRDP measurements. In the second case study, after extracting the molecular structure information through IR, the crystal structure was determined by XRPD analysis. Additionally, pair distribution function (PDF) analysis was used to confirm the molecular conformation and the crystal structure.

The fourth chapter is focused on the anisotropic thermal expansion analysis of two different organometallic systems: three isotypical copper complexes showing photosalient behaviour and two isotypical interpenetrated MOFs. The anisotropic thermal expansion was measured and visualized helping to explain the phenomenon through the development of structural motifs in the compounds. These studies showed the variation in the anisotropic thermal expansion as a function of the different positions of fluorine atoms on the benzene ring in the three isotypical photosalient crystals. In addition, temperature-dependent *in situ* measurements in vacuum on one of the two MOFs revealed a phase transition, which influences the optical properties.

The fifth chapter presents the investigation of the synthetic process of Chabazite zeolite with two different approaches (solvent-free and solvent-based), monitored through *in situ* XRPD and PDF measurements. In the first approach, trends on reactants and products were followed, and the concurrent formation of sodium sulfate was identified. In the second approach, the co-existence of the precursor and product was observed for a long period of time before the reaction completed at 190 °C. Additionally, the kinetic study revealed the possible presence of two reaction mechanisms.

The sixth chapter presents the crystal structure of a polymer, poly(*p*-dinitrosobenzene). Although structure solution of polymers from XRPD can be complicated, in this case, the comparatively high crystallinity of the studied compound allowed for structure solution through XRPD. In addition, TGA/DTA/DSC analysis and temperature-dependent *in situ* XRPD measurements showed thermal stability until circa 150 °C .

The last chapter details an extensive structural study of different forms of metal thiocyanate coordination compounds and their thermal behaviour by temperature-dependent *in situ* XRPD. The crystal structures and thermal behaviour were determined for coordination compounds of cadmium, iron, nickel, and manganese with 4-methoxypyridine, 4-picoline, 4-cyanopyridine,

and 3- ethylpyridine as co-ligands.

Overall, various XRPD methods were applied to extract structural information and enhance the understanding of the thermal behaviour and the formation processes of compounds without any limitation on the class of materials and the aggregation state.

1 Introduction

Due to the continued development and the increasing need for new, high performance materials, the characterization at the atomic scale of new and already existing compounds and their synthetic methods is ever critical. A detailed insight into atomic-level structure of a material is absolutely crucial for understanding its properties and then optimizing its performance or designing a new, improved version.

Single-crystal X-ray diffraction (SC-XRD) is generally used to determine the crystal structure of a compound. The modern methods and software made this technique quite fast and straightforward to use, enabling relatively fast access to reliable structure models also in cases where samples are smaller than 3 μm in size [1]. However, single crystals with shape and size suitable for SC-XRD analysis are not always easy to produce, since in certain cases (*e.g.*, polymeric structures [2] or proteins [3]), the crystallization process requires days or even months and many trials before the right crystallization conditions can be found and optimized. Sometimes, these efforts are still inconclusive, and other techniques must be used, such as X-ray powder diffraction [4–6] and electron diffraction [7, 8].

X-ray powder diffraction (XRPD) can help scientists extract structural details in those cases where SC-XRD fails or an accurate model cannot be obtained. Additionally, contrary to SC-XRD, where only a single crystal from a synthesis batch is analysed, XRPD retrieves information about a large population of crystals. Despite the long story of powder diffraction (the first

powder diffraction experiments were performed by Friedrich in 1912 and 1913 [9, 10]), in the beginning the technique was not as frequently used as today. The main reason is related to the intrinsic problem of the accidental and systematic peak overlap caused by the projection of the three-dimensional reciprocal space on to the one-dimensional 2θ space of a powder pattern. After this problem was partly solved by the Rietveld method [11, 12] and new fast computers were developed, XRPD became a prominent tool in materials characterization. This technique is nowadays commonly used for qualitative and quantitative phase analysis, however, structure determination [13] and characterization of microstructural defects (*e.g.* stacking faults [14]) by XRPD can still be challenging.

Structure determination by SC-XRD and XRPD gives a crystallographic model where the coordinates of the atoms are averaged over all diffracting unit cells of the crystal (*average structure*). Small fluctuations around the equilibrium positions are described using atomic displacement parameters, but in certain crystalline materials (*e.g.* perovskites [15, 16]), the deviation from the average structure is so strong that the symmetry can locally break. Since this phenomenon can have a big impact on the properties, a careful characterization of the *local structure* is crucial. With the term "local structure" is meant the structure of the nearest neighbours around an atom in crystals and molecules. This is usually probed with spectroscopic techniques such as NMR [17], infrared [18] and X-ray absorption [19]. Another method used to study the local structure is pair distribution function (PDF) analysis. This technique uses the "total scattering" approach, which treats both the Bragg and diffuse scattering on an equal basis. As for XRPD, PDF is a technique developed long time ago (beginning of the 20th century) [20, 21] and has become popular in the last few decades thanks to technological advancements. The function gives a measure of the probability of finding a pair of atoms in the material separated by a distance **r**. PDF studies are particularly useful for amorphous [22] and nanocrystalline [23] species, and mixtures of different phases such as crystalline and amorphous phases or liquid suspensions [24].

Since XRPD and PDF analysis are versatile and powerful tools in de-

tecting and extracting structural information, they can be used for studying synthetic processes and behaviour of compounds when they are exposed to external *stimuli* (*e.g.* temperature, UV light, pressure, or mechanical stress). One of the common ways to perform these studies is to do *ex situ* analysis where a number of experiments are performed at different conditions or at the same condition but stopped at different reaction times, and subsequently measured. However, this procedure works only when reaction kinetics are slow and there are no metastable intermediates and reversible phase transitions. In addition, the production of chemical waste is substantial with this approach. To circumvent these disadvantages and obtain time-resolved information, XRPD and PDF analysis have been combined with devices, such as furnaces, UV lamps, pressure pumps, and mills [25]. The first application dates back to 1921 with a diffraction study on iron and steel at high temperatures [26], but it is with the advance in instrumentations, such as new detectors, and the access to high flux beam (synchrotron) that this tool became popular in the last few decades. By performing *in situ* XRPD and PDF experiments, information such as structural changes, phase quantities, and kinetics are extracted from a sample at a specific condition and as a function of the time of stimulus, regardless of the degree of the structural order (crystalline/amorphous) and the state of matter (solid/liquid). Therefore, this tool enables scientists to answer many problems related to the chemistry and physics of materials in non ambient conditions. Investigation of solid state reactions, polymorphic analysis, and gas absorption experiments are only some of the possible applications.

The thermal expansion of a material can also be monitored by *in situ* XRPD. With powder diffraction, the position of each reflection is tracked as function of the temperature and then related to the lattice parameters. By using this information, the expansion can be quantified along the crystallographic axes of the unit cell (*coefficient of thermal expansion*, α) and compared with the behaviour of similar compounds. The investigation of this behaviour may reveal anomalies, such as huge *anisotropic thermal expansion*, where the expansion is remarkable in one direction ($\alpha > 100 \times 10^{-6} K^{-1}$) and

ordinary or negative in another direction ($\alpha < 0 \times 10^{-6}K^{-1}$) [27–29]. This phenomenon may be due to structural peculiarities and molecular mechanisms that make these materials promising candidates for applications as microscale actuators or thermal expansion compensators. Therefore, understanding the structure-property relationship is crucial to properly manipulate molecular motion and design sensitive thermomechanical devices [30].

In the process of investigating the formation mechanism and the crystallization of certain materials, such as zeolites, which are produced by hydrothermal synthesis and investigated in this thesis, *in situ* experiments may be challenging to perform owing to extreme conditions, such as high pressures, high temperatures, and the need for sealed reaction chambers. In these cases, the development of new strategies or devices is the first requirement to satisfy for successful *in situ* experiments [31]. Most of these devices are small (*micro-reactors*) in order to improve the heat transfer efficiency and have high pressure tolerance. To facilitate the penetration of the X-ray beam, the wall thickness of these devices is kept as small as possible, and these devices are mostly used at high energy synchrotron light sources. However, since the access to synchrotron facilities is possible only after the approval of a proposal, is limited to a small period of time, and requires travelling to other places, the need for micro-reactors suitable for laboratory diffractometers is growing.

In this thesis, I will present my research work with a focus on the atomistic details of different compounds at ambient condition or while the samples are subjected to external *stimuli*, such as pressure and temperature. The thesis includes the analysis of many compounds without any limitation on the classes of materials. The targeted samples can be divided in organic molecules, metal coordination compounds, inorganic materials, and polymers. The results are distributed in different sections depending on the properties of the investigated compounds and the type of analysis. For each class of material, I will discuss in detail the open problems presented in this section, and consistently report the results, the instrumentation and the methods used for each sample. XRPD was the main tool for conducting the research. *Ab initio* structure solution methods and Rietveld refinement were extensively employed

for determining the crystal structures, whereas PDF analysis was used as a complementary technique to confirm the structural models for the short-range order and to monitor the presence of amorphous or weakly crystalline compounds in the analysed samples. The investigation of the compounds in this thesis is supported by supplementary techniques including vibrational spectroscopy (IR and Raman), elemental analysis, scanning electron microscopy (SEM) coupled with EDX, and thermal analysis, such as thermogravimetric analysis (TGA), differential thermal analysis (DTA) and differential scanning calorimetry (DSC). In the next section, the diffraction techniques and the related methods will be briefly introduced.

2 Powder diffraction analysis and instrumentation

In this chapter, a brief introduction to the techniques, methods, and instrumentations that were used to investigate the different materials and solid state reactions present in this thesis is given. In particular, XRPD and PDF analysis, two techniques extensively employed in this research, the methods for structure characterization, and laboratory and synchrotron light sources will be briefly discussed. Additionally, the devices for *in situ* and *operando* studies, used, designed, and built during this PhD, will be illustrated.

2.1 Basics of X-ray powder diffraction (XRPD) and Pair distribution function (PDF)

The term "powder diffraction" describes a technique where radiation with a wavelength comparable to interatomic distances is incident on a powder, made of a high number of randomly oriented crystallites, generating the phenomenon of diffraction. Different types of radiation can be used, such as X-rays, neutrons, and electrons but herein I will exclusively focus on the X-ray diffraction.

The principle of diffraction from a crystal was described by William Lawrence Bragg, via the Bragg equation $2dsin\theta=\lambda$, as a reflection of the beam

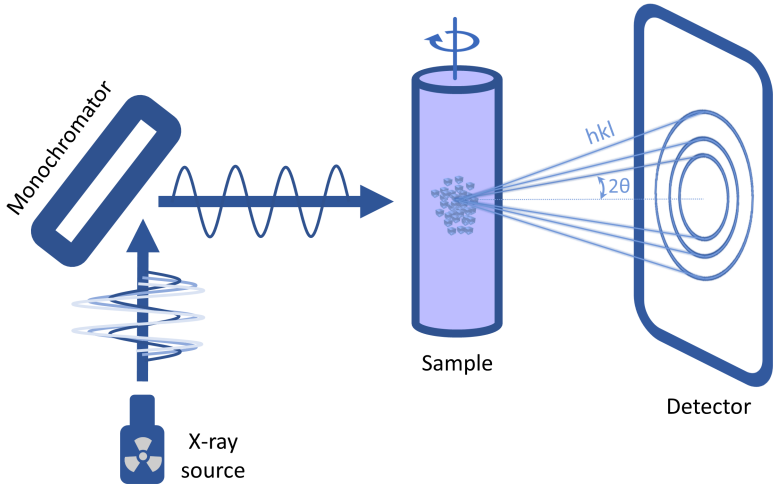

Figure 2.1. Schematic representation of a typical setup for XRPD measurements in transmission (Debye-Scherrer) geometry.

with wavelength λ by sets of parallel lattice planes, each of them separated by a distance *d* and characterized by the Miller indices *hkl*. This results in a

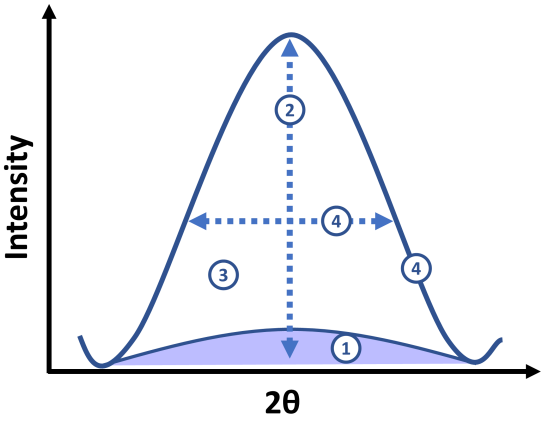

Figure 2.2. Schematic representation of the different parts of a XRPD pattern: background/diffuse scattering (1), peak position (2), integrated peak intensity (3), and peak profile (4).

sharp spot of high intensity related to a specific angle of reflection 2θ. However, in the presence of a crystalline powder, constituted by a high number of randomly oriented crystallites, Debye-Scherrer cones are formed (Figure 2.1). The cones on a screen perpendicular to the primary beam (*e.g.* 2D detector) appear as rings, which become sharp peaks (*Bragg peaks*) in a one-dimensional powder pattern (diffractogram or XRPD pattern) after orizontal or vertical (depending on the diffractometer geometry) one-dimensional cut through the rings [4]. Therefore, Bragg peaks (Figure 2.2) are related to specific lattice planes of a crystal structure and as a consequence, from the analysis of their positions, lattice types, lattice parameters, space group[1] (or at least a subset of the possible ones), and macrostrain (*i.e.* uniform variation of the *d*-spacing) can be revealed. In addition, since each substance produces a characteristic diffraction pattern, the peak positions can be considered as a sort of "fingerprint", which can be used to identify a compound (*qualitative phase analysis*).

The dimension of the finite crystallite domains is one of the primary sources of the peak broadening. This is usually measured from the full width at half maximum (FWHM) by using the Scherrer equation [32,33]. The presence of disorder, such as a non uniform distortion of the inter-layer distance *d* (*microstrain*) or stacking faults, has also an impact on the peak asymmetry and broadening (*peak profile*). In addition, there are also instrumental contributions affecting peak broadening that must be deconvoluted when accurate sample-related information has to be extracted.

From the radiation-sample interaction, inelastic scattering (*Compton effect*) and coherent elastic scattering are generated. The latter has both Bragg and diffuse components. The Bragg scattering originates from the presence of a periodic arrangement of atoms in the sample and gives Bragg peaks, as already discussed. From the area below the peak (*intensity*), the crystal structure of a compound can be determined. In addition, details about

[1] In this case, peak intensity is also fundamental, since the absence of classes of reflections means the presence of one (or more than one) symmetry operator that enables to identify the possible extinction symbols and the related possible space group(s).

the site occupancy factor (SOF), temperature factors, and texture can also be revealed and quantitative phase analysis carried out. The diffuse scattering arises from the lack of long-range order and is visible as broad bumps in the XRPD pattern. Standard XRPD analysis focuses on the information that can be extracted from the Bragg peaks of crystalline materials and excludes the diffuse scattering from the data analysis (unless a quantification of the amorphous phase is required) by treating it as a background signal. However, the information coming from this portion of the diffractogram is substantial since details about the local structure can be extracted. One of the techniques to extract this information is the "total-scattering" or PDF analysis. The PDF is a scaled histogram of all the atom–atom distances in the material [34]. It is averaged over all atoms in the scattering volume and the total time of the experiment, giving a measure of the average radial structural environment of all the atoms (Figure 2.3). This is nowadays considered as a cutting-edge analysis for investigating solutions, amorphous compounds, disordered structures, and nanostructured materials, however the first applications go back to the first half of the twentieth century with the experiments performed on carbon by Warren [35] and Franklin [36]. Collecting data for generating PDF plots means performing XRPD experiments. The difference is in the good statistics and a high measured value of Q ($\mathbf{Q_{max}}$, with $Q=4\pi\sin(\theta)\lambda^{-1}$), which require the use of diffractometer with molybdenum or silver radiation (at the expense of a long exposition time) or synchrotron light sources. The collected reciprocal space data are then corrected for the inelastic and self scattering to give the reduced total-scattering structure factor, **F(Q)**, which is then sine-Fourier transformed to obtain the experimental PDF, **G(r)**:

$$G(r) = \frac{2}{\pi}\int_{Q_{min}}^{Q_{max}} F(Q)\sin(Qr)dQ \tag{2.1}$$

This technique is both straightforward and intuitively easy to comprehend. In a PDF plot, which shows the **G(r)** as function of the interatomic distance, **r**, a positive peak at a given **r** corresponds to high correlation between two atoms at distance **r** whereas G(r)=0 represents the average atomic den-

sity of the irradiated sample (Figure 2.3). With PDF analysis, it is possible to

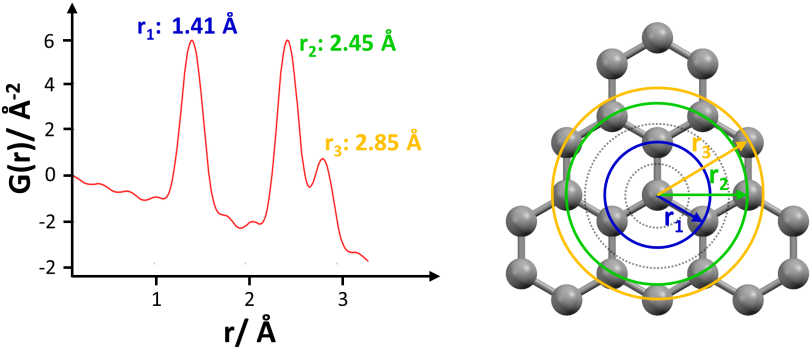

Figure 2.3. Relationship between peaks in the PDF plot (left) and the actual atom pair distances in the sample structure (right).

look at the structure with respect to the short-range order (SRO), the medium-range order (MRO) and the long-range order (LRO) [37,38]. This means that the function is sensitive to intramolecular correlations, such as atomic coordination, bond lengths, torsions, as well as molecular conformation (SRO), and to intermolecular interactions, orientations, and packing (MRO).

In an ideal, perfect crystal, the relationships between atoms separated by large distances are visible as distinct peaks. However, due to the presence of crystalline domains, the inter-atomic relationships are lost and the PDF signals damps out. This feature allows for the identification of the largest distance within a coherently scattering domain (*domain size*). The signal-attenuating effect, which is also related to the shape of the coherent domains, can often be accounted for by modifying the ideal PDF signal for an infinitely periodic crystalline system, $\mathbf{G_\infty(r)}$, with a characteristic function, $\boldsymbol{\gamma}\mathbf{(r)}$ [39]:

$$G(r) = \gamma(r)G_\infty(r) \tag{2.2}$$

With this analytical expression, PDF of disordered samples can be described by modulating the PDF of the same sample in a non-disordered state with the proper function.

2.2 Methods for structure determination and refinement from XRPD

The process for obtaining the crystal structure from XRPD can be broken into six steps: i) data acquisition, ii) determination of the unit cell (*indexing*), iii) determination of the space group from the systematic absences, iv) extraction of the integrated peak intensities and the refined lattice parameters (*whole powder pattern decomposition methods*), v) determination of the crystal structure (*reciprocal space methods and global optimization methods*[2]), vi) refinement of the crystallographic model structure (*local optimization methods*), and visual inspection for checking plausibility of the crystal structure (*e.g.*, chemical bonds and molecular geometry). This section shortly deals with the last three steps with a focus on the methods that were used during this thesis.

2.2.1 Whole powder pattern decomposition methods

Whole powder pattern decomposition methods differ from the single Bragg peak fitting since they fit the whole XRPD pattern using instrumental (*e.g.*, wavelength and axial divergence) and sample information (*e.g.*, peak shape, space group, and lattice parameters). From these methods, peak intensities of all reflections can be extracted to be used as input in the structure determination process. The great advantage is that it is possible to obtain refined parameters, such as lattice parameters or crystallite size, without any structural model. Two routines for the decomposition process, commonly used nowadays, were developed in the 1980s by Pawley [40] and Le Bail [41]. The Pawley routine is based on least squares analysis of the XRPD pattern where background parameters, instrumental zero error, unit cell parameters, peak shape parameters and integrated intensities are refined during the fitting process. Since the method assumes all *hkl* reflections as independent parameters, the least squares fitting can give any values. Therefore, although the

[2] In this thesis, I will focus on the last ones

total area of a group of largely overlapping peaks are well determined, the intensity of the single peaks may also assume negative values. To limit this problem, constraints and restraints (slack constraints) were included in the routine. The Le Bail method was developed to speed the fitting process and avoid the intensity-related problem of the Pawley routine. In this method, based upon Rietveld's original method, the major difference is that the intensities of the individual peaks are no longer treated as least squares parameters and are never refined but adjusted in an iterative procedure. At the beginning, the intensity are set to an arbitrary value, and they are treated as "calculated" values as if they had been derived from a structural model. Then, by using the refined parameters from the least-squares fitting, new intensity values can be calculated, which are used in the subsequent cycles until convergence is reached. However, it must be noted that in case of strong overlapping, both methods tend to give erroneous values and care must be taken in using those data.

2.2.2 Global optimization methods

Global optimization methods are used for structure determination. The advantage of these methods is in the algorithm, which is able to locate the global minimum from any random starting point without being trapped in a local minimum (corresponding to an incorrect determined structure, Figure 2.4). Global optimization methods involve moving atoms around a known unit cell until the best agreement with the observed diffraction data is obtained. In order to understand if the best minimum has been reached, it is possible to compare the obtained agreement factor value with that obtained from a Pawley or Le Bail refinement [13]. To increase the chance of success, different strategies were developed during these years. The main idea is to use any chemical information as constraints or restraints (*e.g.* torsion angles, and bond lengths and angles) to compensate for the reduced information content of the XRPD pattern. In case molecules are present in the crystal structure, a rigid body can be built and used, leaving only the position and the orientation

of the molecule within the unit cell to be determined. Many methods have been developed during these years such as the Grid Search method, Monte Carlo method and the Simulated Annealing technique [4, 42]. Since the last technique was mostly used throughout this thesis, a brief description is now given.

The simulated annealing algorithm belongs to the so-called *direct space methods* and it is the most used and effective of the algorithms for structure determination from XRPD data. The name refers to the annealing process where a crystalline compound is obtained by slowly cooling from a melt. In powder diffraction, a trial crystal structure is provided to the algorithm (the atom coordinates are usually set to arbitrary numbers), which probes the whole parameters space by generating a huge number of different crystal structures. For each crystal structure, a XRPD pattern is calculated and compared to the observed one by means of an agreement factor (usually R_{wp}, see section 2.2.3.). After each cycle, the difference between the new agreement factor and the old one is monitored. If this difference is negative, the variation led to an improvement of the fit and the new structure model is accepted. If the difference is positive, the fit is worse but the structural model can be

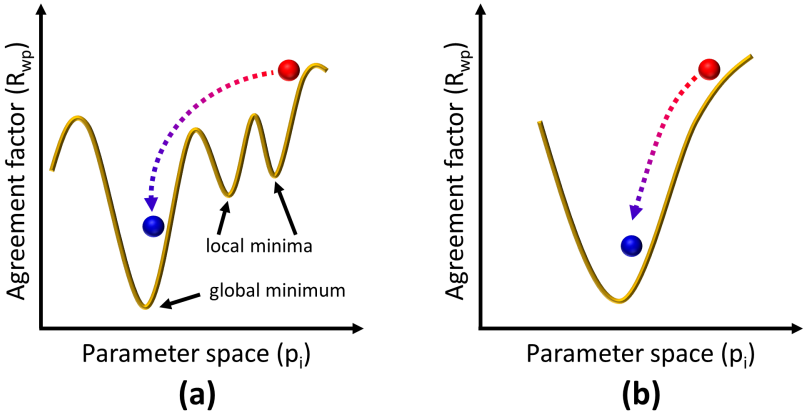

Figure 2.4. Schematic representation of the difference between global (a) and local (b) optimization methods.

accepted with a probability according to an acceptance criterion, which decreases with decreasing the temperature. This is the key feature that allows the 'uphill moves' in the global minimisation process and avoids the algorithm to be trapped in a local minimum.

2.2.3 Local optimization methods

When a crystal structure is determined through global optimization methods or an isomorphic structure is used as starting model, the structural model must be optimized with a local optimization method in order to find the global minimum. The most used and common local optimization method is the Rietveld refinement and it is based on least squares refinement [4]. The method was introduced by Hugo Rietveld in 1969 as a profile refinement method for nuclear and magnetic structures [11]. Nowadays it is mostly used for refining crystal structures to XRPD patterns. The Rietveld refinement marked a turning point in powder diffraction since it does not use the integrated intensities, which can be affected by errors due to accidental and/or systematic overlap of some Bragg reflections, but employs directly the profile intensities (*step-scanned intensities*) obtained from the XRPD pattern. This feature gave an important contribution to the development of powder diffraction method by enabling scientists using powder diffraction to be no longer limited to data analysis by methods expressly developed for single crystal investigation.

The core of the algorithm of the Rietveld method is to use the least squares procedure to refine the parameters related to the structure, specimen and instrument effects, and optimize the fit to the whole powder pattern available in step-scanned intensity data. This procedure intrinsically accounts for peak overlap. The function M to be minimized is the following:

$$\mathrm{M} = \sum_{\mathrm{i}} \mathrm{w_i}\{\mathrm{y_{obs,i}} - \frac{1}{\mathrm{c}}\mathrm{y_{calc,i}}\}^2 \tag{2.3}$$

where the sum is over the N observed data points in the chosen 2θ range, $y_{obs,i}$ and $y_{calc,i}$ are the observed and calculated step-scanned intensities, c is

the scale factor, and w_i is the weighting factor derived, *e.g.*, from the variance of $y_{obs,i}$ as $1/\sigma(y_{obs,i})$.

The calculated intensity $y_{calc,i}$ can be expressed as the sum of the contribution from the background ($y_{bkg,i}$) and the Bragg reflections **s**=(*hkl*) ($y_{s,i}$):

$$y_{calc,i} = y_{s,i} + y_{bkg,i} \tag{2.4}$$

with:

$$y_{s,i} = S\sum_{s}(|F_{calc,s}|^2 \Phi_{s,i} Corr_{s,i}) \tag{2.5}$$

where the sum runs over all Bragg reflections **s** of a phase that contribute to the position *i* in the powder pattern, S is the scaling factor applied to the reflection intensities, $Corr_{s,i}$ is the product of various correction factors (*e.g.* multiplicity, absorption correction, Lorentz-polarization factor, and preferred orientation correction) applied to the reflection intensities $|F_{calc,s}|^2$ that depends on the diffraction geometry and individual reflection indices, and $\Phi_{s,i}$ is the profile function, which is determined by the instrumental profile and microstructural parameters of the sample.

To assess the quality of the refinement of a structural model in powder diffraction, different agreement factor (*R-factor*) have been introduced. Those factors, as in SC-XRD, are based on the difference between the observed and the calculated data.

The powder pattern *R*-factor R_p:

$$R_p = \frac{\sum_i |y_{obs,i} - y_{calc,i}|}{\sum_i y_{obs,i}} \tag{2.6}$$

The weighted powder pattern *R*-factor R_{wp}:

$$R_{wp} = \sqrt{\frac{\sum_i w_i [y_{obs,i} - y_{calc,i}]^2}{\sum_i w_i y_{obs,i}^2}} \tag{2.7}$$

where the weight w_i is, *e.g.*, derived from the variance of $y_{obs,i}$ as $1/\sigma^2(y_{obs,i})$

The expected *R*-factor R_{exp}, which gives the value of the best possible fit

based on counting statistics:

$$R_{exp} = \sqrt{\frac{N-P}{\sum_i w_i y_{obs,i}^2}} \tag{2.8}$$

with *N* the number of data points and *P* the number of parameters.
By using R_{exp} and R_{wp}, it is possible to calculate the GOF (or χ), which is a good measure of the quality of the Rietveld refinement:

$$GOF = \frac{R_{wp}}{R_{exp}} = \sqrt{\frac{\sum_i w_i [y_{obs,i} - y_{cal,i}]^2}{N-P}} \tag{2.9}$$

For comparison with single crystal data, the Bragg *R*-factor for each crystalline phase is introduced:

$$R_{Bragg} = \frac{\sum_k |I_{obs,k} - I_{calc,k}|}{\sum_k I_{obs,k}} \tag{2.10}$$

where $I_{obs,k}$ and $I_{calc,k}$ are the 'observed' and calculated intensities for each reflection *k*.

Of course, it should be noted that a careful visual inspection of the fit and the crystal structure must always be performed in order to properly direct the refinement process and discard wrong models with good *R*-factor but no chemical sense.

2.3 Instrumentations

2.3.1 Laboratory source

The experimental setup of a laboratory diffractometer for XRPD measurements consists of an X-ray source, optics, slits, a goniometric head, a beam stop and a detector (Figure 2.5). Each of these elements is important in obtaining high quality XRPD data. Assembling and choosing the right setup

may avoid the collection of low quality diffractograms that can lead to misleading results or prevent the data analysis from being performed.

Before an experiment, the X-ray source must be carefully chosen to prevent sample-related issues such as absorption and fluorescence. When one of these problems occurs, a different X-ray source (*i.e.* wavelength) must be chosen. Usually the most common ones are those with silver (0.559 Å), molybdenum (0.709 Å), copper (1.54 Å) and cobalt (1.79 Å) anodes. Silver and molybdenum anodes can be used for laboratory PDF analysis. The use of optics, such as filters and monochromators, helps to prevent background noise and the formation of Bragg peak doublets in the final XRPD pattern by removing unwanted radiations (*e.g.* K_β in copper anodes), focusing the beam and selecting one characteristic wavelength (*e.g.* $K_{\alpha 1}$ in copper anodes). Slits tune the shape, the intensity and the resolution of the Bragg peaks, whereas new detectors, such as the Mythen 1K (Dectris) used during the course of this PhD, reduce the data collection time and the background noise.

Laboratory XRPD diffractometers can mainly be found in two different geometries: reflection (Bragg-Brentano) and transmission (Debye-Scherrer). The first geometry is suitable for strongly X-ray absorbing samples whereas the second one is suitable for less absorbing X-ray samples. In this thesis, Bruker D8-Advance and STOE Stadi-P diffractometers with transmission geometry were the most used ones.

2.3.2 Synchrotron light source

A synchrotron light source is a source of electromagnetic radiation produced in a storage ring where charged particles (electrons) travel at relativistic speeds. When their trajectory is forced to curve by a magnetic field, synchrotron radiation (photons) is emitted.

During this PhD, the synchrotron light sources at ESRF (beamline ID15A, France) and DESY (PETRA III, beamline P02.1, Germany) were used for performing PDF experiments and testing the *in situ* XRPD devices. The reasons behind this decision are mainly two: high flux beam and short radiation

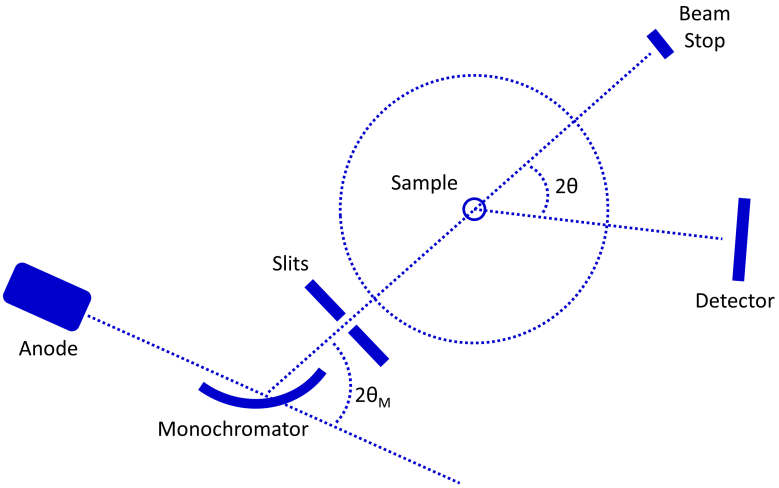

Figure 2.5. Schematic view of an experimental setup of a laboratory diffractometer in transmission geometry showing the different elements such as X-ray source (anode), optics (monochromator), slits, beam stop and detector.

wavelength. The combination of these factors allows for high signal-to-noise ratio and short measurement time, suitable for *in situ* experiments. In addition, XRPD patterns can be collected to a high Q maximum (Q_{max}), very important for PDF analysis, and high X-ray absorbing samples can be penetrated and measured in transmission mode.

2.3.3 Devices for *in situ* and *operando* studies

In situ measurements allow scientists to investigate their material in 'real time', while it is subjected to external *stimuli* such as temperature, pressure, mechanical stress or UV radiation. When the structure and the activity of a material, *e.g.* during a catalytic or a synthetic process, are measured while the same parameters as in the actual *working* conditions are applied, the term '*operando*' can be used [43, 44]. Both experiments reveal important changes in crystal structure, microstructure, and phase composition of a material that can be related to its properties and used for improving its performance. In

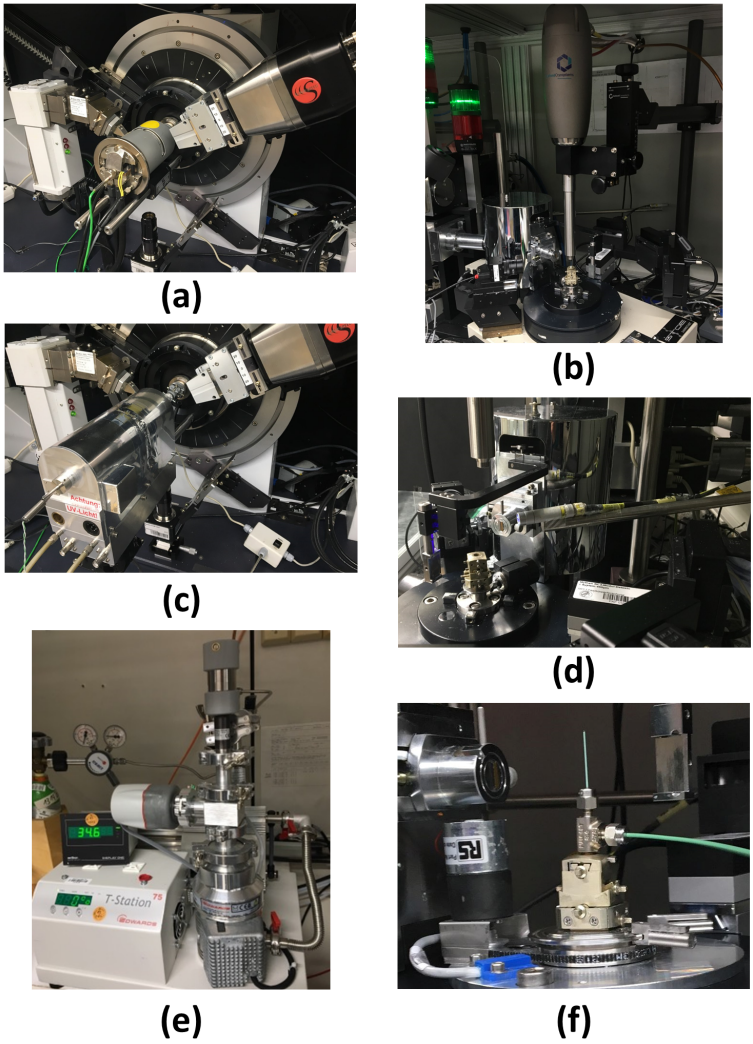

Figure 2.6. Instrumental setups used in this thesis to perform temperature-dependent (a,b), UV (c,d) and pressure (e,f) *in situ* XRPD experiments.

the course of this thesis, several *in situ* experiments were performed using different reactors, which will now be briefly introduced.

Temperature-dependent *in situ* measurements were performed using two

different devices to access different temperature ranges. Temperatures in the range of 25 °C-900 °C were reached with the mri reaction chamber (Figure 2.6,a) whereas temperatures in the range of -193 °C-227 °C were accessed with the Oxford cryostream 800 PLUS, a cryogenic gas cooler (Figure 2.6,b).

In situ pressure measurements were performed with an in-house built capillary microreactor and a T-Station 75 Turbomolecular pumping system (Figure 2.6,e-f). This system achieves low (*vacuum* conditions) and high pressures, and allows for gas loading or solid-gas reaction experiments. In addition, temperature devices can also be added to this setup.

For *in situ* UV experiments, two devices were employed. When experiments were performed on the STOE diffractometer, a UV lamp with a radiation of 365 nm was used whereas for the Bruker D8, an in-house built UV chamber was used (Figure 2.6,c-d).

Three reactors were designed and built in this research period in order

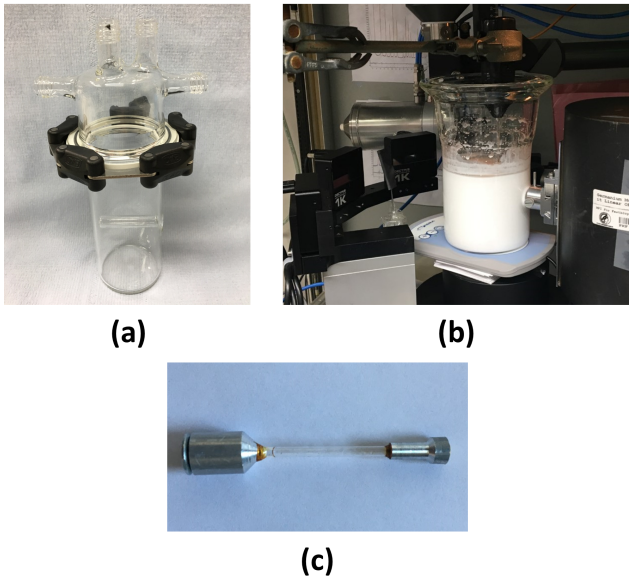

Figure 2.7. View of the reactors designed and built during this thesis. Reactors for investigating suspensions (a-b) and autoclave-like microreactor (c).

to investigate the synthesis and the crystallization process of different compounds (Figure 2.7). The reactors are different with respect to purpose, use, characteristics and size. The common idea was to design and build the devices for using them with laboratory diffractometers. The first two devices, made of glass, are very similar and they differ only in the capacity. They have been designed for *in situ* and *operando* investigations of suspensions. These glass devices have several inlets in the top part for connecting several components (*e.g.* pH and temperature sensors, and mechanical stirrers), for inserting liquids/gas in the reaction mixture or for venting any excess of gas out. The last device is a mini autoclave reactor (with length of circa 30 mm), which was designed to investigate the synthesis of certain materials, such as zeolites, who required a closed and sealed system. The microreactor is made of an open quartz capillary sealed on both sizes by two elements in aluminium. The size of the aluminium element at the bottom allows this system to perfectly fit in a standard goniometric head of a STOE Stadi-P diffractometer whereas the upper part is smaller so that the flow coming from the Oxford cryosystem device can reach the capillary and heat (or cool) the sample.

3 Characterization and thermal behaviour studies

In this chapter, a detailed study of two compounds, ferrous glycine sulphate pentahydrate, $Fe(C_2H_5NO_2)SO_4 \cdot 5(H_2O)$, and glycolaldehyde ammonia, $C_6H_{15}O_3N_3$, will be presented. This includes the complete characterization of the substances and the elucidation of their crystal structures.

3.1 Ferrous glycine sulfate pentahydrate

Ferrous glycine sulfate pentahydrate, contained in the iron supplement for anaemia commercially known as ferro sanol duodenal®, was characterized by laboratory XRPD, scanning electron microscopy (SEM) and infrared spectroscopy (IR). The thermal behaviour was elucidated by thermal analysis (TGA and DTA) and *in situ* XRPD measurements. This work was published in the journal *Zeitschrift für anorganische und allgemeine Chemie* and in 2019/12 was chosen as the front cover [45].

3.1.1 Introduction

Metal coordination compounds of glycine ($C_2H_5NO_2$ = gly) with general formula $M^{2+}\ (gly)_a A^{b-}_{2/b} \cdot xH_2O$ (M = Mg, Mn, Fe, Co, Ni, Cu, Zn) are relevant for nutrition. Since they can act as a source of trace elements and

amino acids in human and animal diets [46,47], most of these compounds are commonly used in dietary supplements.

These compounds exhibit a huge variety of properties. Glycine based salts of cobalt, zinc and manganese show positive effects in correcting mineral deficiency in animals [48]. The iron based salt is used as therapeutic agent to prevent or treat iron deficiency anaemia in infants [49], or lactating and pregnant women as well as to fortify food [50].

Furthermore, it was demonstrated that some of these compounds have physical properties like ferro-electricity [51], pyro-electricity [51], magnetism [52] and non-linear optical properties [53,54].

Concerning the Gly-M-SO_4 system, several crystal structures are reported in literature, such as magnesium, cobalt, nickel and zinc glycine sulfate pentahydrate [55–57]. However, in regard to the iron-based system, only few compounds were studied. In particular, the crystal structure of the anhydrous form was determined by XRPD [58], the pentahydrate form, included in the PDF database®as an indexed compound only, was insufficiently described in 1960 and not completely characterized due to the low quality of the data [59]. The trihydrate was submitted to the CSD database only as private communication [60].

In this work, Fe(gly)SO_4·5(H_2O) (**1**), contained in capsules of the dietary supplement ferro sanol duodenal®, was characterized by using different techniques (XRPD, IR, SEM). The thermal behaviour was investigated by thermal analysis (TGA and DTA) and *in situ* XRPD measurements. Thermal analyses revealed phase transitions from **1** to the anhydrous form through the trihydrate compound, Fe(gly)SO_4·3H_2O (**2**). Description of the crystal structures, herein confirmed by independent *ab initio* structure solution and subsequent Rietveld refinement, and an interpretation of the phase transition mechanism was also included.

The aim of this work is to gain knowledge about the crystal structure and the thermal behaviour of the dietary supplement. This information is important in the process of finding new pharmaceutical drugs, and detecting drug fraud and abuse, such as product counterfeiting where the type or the amount

of the ingredients is incorrect. Additionally, information about storage and drying conditions can also be extracted.

3.1.2 Results and discussion

Crystallites of **1** were initially inspected by SEM. Figure 3.1 (top) shows aggregated crystallites with a broad distribution of dimensions ranging from 5 to 20 μm. Inspection of the SEM image coupled with BSE detector revealed traces of heavily scattering particles, probably elemental iron or an iron oxide phase, which could be a side product of the synthesis (Red circle in Figure 3.1, bottom). To obtain information about the stoichiometry of the compound, SEM-EDX analysis was performed revealing a Fe:S:N ratio of 1:1:1, as expected (Table 3.1).

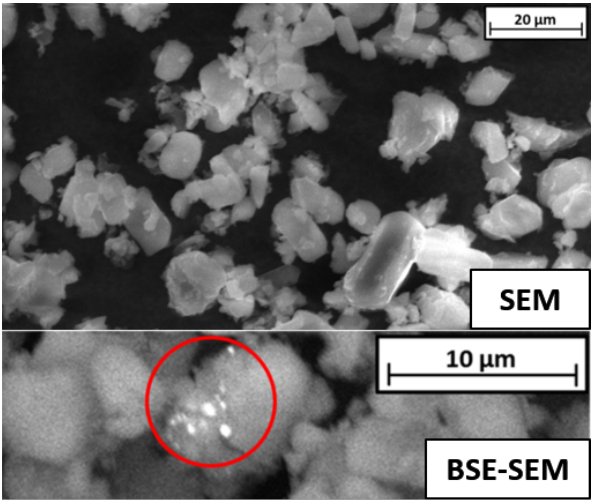

Figure 3.1. SEM image of crystallites of compound **1** with dimensions between 1-10 μm in width and 2-20 μm in length (top); BSE-SEM image of **1** showing the presence of traces of heavily scattering particles, probably elemental iron or iron oxide(white small particles), highlighted by the red circle.

The IR spectrum of **1** at room temperature was collected with the aim of confirming the presence of all expected co-ligands in the complex and gaining information of their binding to the metallic centre. Selected excerpts of the IR spectrum are enlarged for clarity in Figure 3.2. A tentative bands assignment was made, based on the reported vibrational spectra of related compounds like iron based glycine [61], glycine sulfates [62], and metal(II) based glycine sulfate compounds [55]. Table 3.2 shows all the bands with the corresponding assignments. It was possible to confirm the presence of water, glycine and sulfate ions in the compound and to extract several features of the crystal structure. Indeed, the bands in the (1600-1300) cm^{-1} range related to antisymmetric and symmetric stretching modes of C-O and deformational NH_3^+-related N-H vibrations confirmed the presence of glycine molecules in zwitterionic form and as monodentate ligands. Additionally, the presence of a network of possible hydrogen bonds is supported by bands associated with stretching and out-of-plane O-H(···O) and N-H(···O) vibration at 3222 cm^{-1} and 785 cm^{-1}, respectively.

Compound **1** crystallizes in the triclinic space group $P\bar{1}$ with lattice parameters a = 5.9951(1) Å, b = 6.8013(1) Å, c = 13.4021(3) Å, α = 85.414(1) Å, β = 82.893(1)°, γ = 83.072(1)° and V = 537.12(2) $Å^3$. This structure, determined by Simulated Annealing, is isostructural with the Mg-, Mn-, Co- and Zn-based pentahydrate compounds reported in literature. In the asymmetric unit, two distinct octahedrally coordinated iron sites can be observed, which are located on symmetry centres. One iron atom is exclusively coordinated by six water molecules ($[Fe(H_2O)_6]^{2+}$ complex ion) whereas the other one is coordinated by four water molecules and two glycine molecules ($[Fe(gly)_2(H_2O)_4]^{2+}$ complex ion, Figure 3.3). A close inspection of the

Table 3.1. Composition of **1** detected by SEM-EDX. The values are given in atomic percentage.

Element	N	S	Fe
Average	10.1	11.7	10.8
S.D.	0.8	0.6	0.6

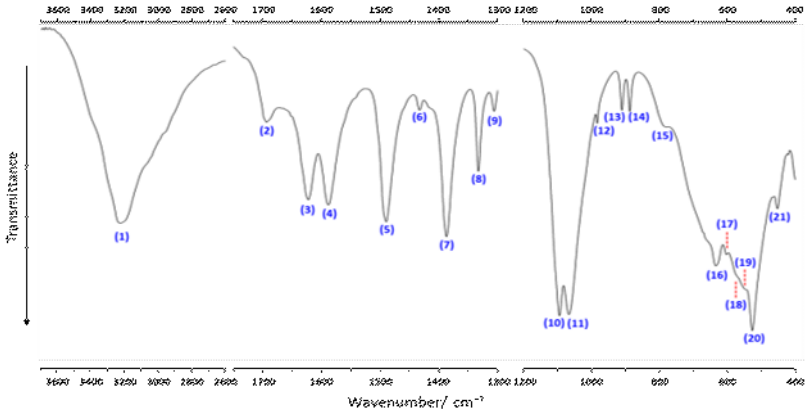

Figure 3.2. Excerpts of the IR spectrum of **1** crystals measured at room temperature. Adapted from [45].

Table 3.2. Bands assignment in the IR spectrum of **1**.

Band no.	IR wavelength[a)]	Assignment
1	3222,mb	ν O-H(···O), ν N-H(···O)
2	1692,w	$\delta_{as}NH_3^+$
3	1623,m	ν_3 COO^-
4	1589,m	δ_{as} NH_3^+
5	1491,m	δ_s NH_3^+
6	1433,w	δ CH_2
7	1387,m	ν_{as} COO^-
8	1333,m	τ CH_2
9	1306,w	ω CH_2
10	1095,vs	ν_3 SO_4
11	1067,vs	ν_3 SO_4
12	983,sh	ν_1 SO_4
13	911,m	δ CH_2
14	888,m	ν_s CCN
15	785,sh	γ O-H(···O), γ N-H(···O)
16	635,s	ν_4 SO_4
17	604,sh	ω COO^-
18	570,vb	ν_s Fe-O, ω COO^-
19	550,vb	ν_s Fe-O, ω COO^-
20	527,vs	δ COO^-
21	452,m	ν_2 SO_4

[a)]List of abbreviations: weak(w), medium(m), strong(s), very strong (vs), shoulder (sh), broad (b), very broad (vb).

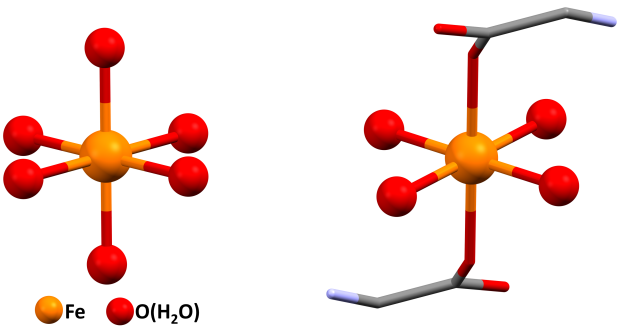

Figure 3.3. Coordination of the two iron sites in **1**: $[Fe(H_2O)_6]^{2+}$ complex ion (left) and $[Fe(gly)_2(H_2O)_4]^{2+}$ complex ion (right). Hydrogen atoms are omitted for clarity.

complex ions shows that glycine molecules coordinate the iron site as monodentate ligands, as expected from IR analysis, and in *trans* configuration.

The distinct complex ions arrange in the crystal by forming two different layers parallel to the *ab*-plane, which are slip-stacked along the *c*-axis with $(SO_4)^{2-}$ ions in between (Figure 3.4). In the $[Fe(gly)_2(H_2O)_4]^{2+}$ layer, the complex ions are connected by hydrogen bonds between water molecules and the glycine-related oxygen atoms [$O(H_2O) \cdots O(gly)$ distance: 2.58 Å] and

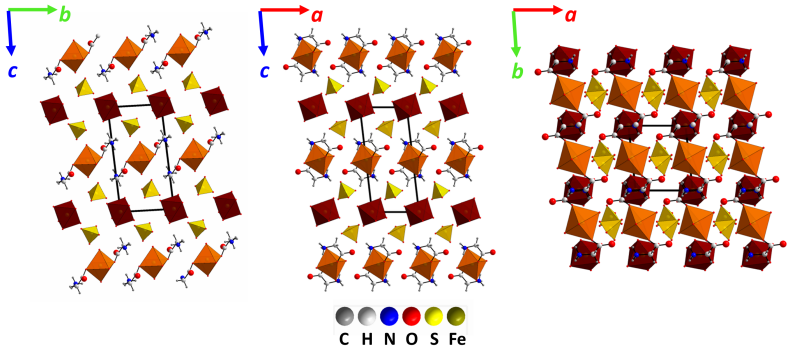

Figure 3.4. Projections of the crystal structure of **1** along *a*- (left), *b*- (middle) and *c*- (right) crystallographic axes. The 1D polymeric chains are highlighted in different colors. Adapted from [45].

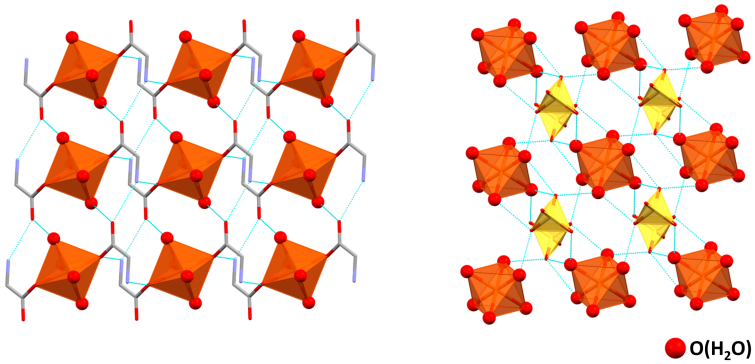

Figure 3.5. Intra-layer interactions in $[Fe(gly)_2(H_2O)_4]^{2+}$ (left) and $Fe(H_2O)_6]^{2+}$ layers (right) in **1**. Adapted from [45].

between glycine ligands (H $\cdots$ O distance: 2.58 Å, Figure 3.5, left). The $[Fe(H_2O)_6]^{2+}$ layer is built up by interactions that the complex ions form with the sulfate ions ($O(SO_4^{2-}) \cdots O(H_2O)$ distance: (2.64-2.84) Å, Figure 3.5, right). Additionally, the layers are kept together by a potential hydrogen bond network with sulfate ions as acceptors.

The thermal behaviour of compound **1** was investigated by coupled TGA/DTA and *in situ* XRPD measurements. The thermal analysis was performed in a dynamic oxygen atmosphere and the sample was heated from 30 °C to 800 °C (Figure 3.6). The TGA-curve (Figure 3.6, black line) shows two weight losses of 9.6 and 13.7 wt-% in the temperature range 74 °C - 119 °C associated with two endothermic peaks ((1-2) in Figure 3.6, blue line). The first step corresponds to the release of two water molecules (Δm_{calc}=11.7 wt-%) and the second one to the release of three water molecules (Δm_{calc}=17.6 wt-%, Table 3.3). The small discrepancy between experimental and calculated weight losses is likely due to the presence of amorphous or nanocrystalline by-products (probably iron or iron oxide), as observed in SEM image and suggested by the hump in the background of the XRPD pattern (Figure 3.7). Further heating of the sample leads to poorly resolved and overlapped weight losses associated with two broad exothermic peaks in the DTA curve

Table 3.3. List of the results obtained from the TGA/DTA measurement of **1**.

Step No.	T/ °C	Reaction assigned	Δm_{tot}(calc)/ wt-%	Δm_{tot}(exp)/ wt-%
(1)	74-100	Release of 2 H_2O	11.7	9.6
(2)	119-185	+ Complete release of H_2O	29.3	24.8
(3+4)	185-440	+ Decomposition of gly and oxidation of Fe(II)	47.9	54.9
(5)	588-683	+ Decomposition of Fe_2SO_4 into Fe_2O_3	74.0	76.8

((3+4) in Figure 3.6). These steps can be attributed to the decomposition of the glycine and oxidation from iron(II) to iron(III), leading to formation of a mixture of iron(II) sulfate (mikasaite form) and iron(III) oxide. By heating above circa 588 °C, the last weight loss step, corresponding to the complete decomposition to iron(III) oxide, is observed ((5) in Figure 3.6). The presence of these two crystalline forms was confirmed by *ex situ* analysis of the residues obtained after further TGA measurement.

To further investigate the thermal behaviour of **1** and correlate the thermal measurements to changes in the crystal structures, temperature dependent *in*

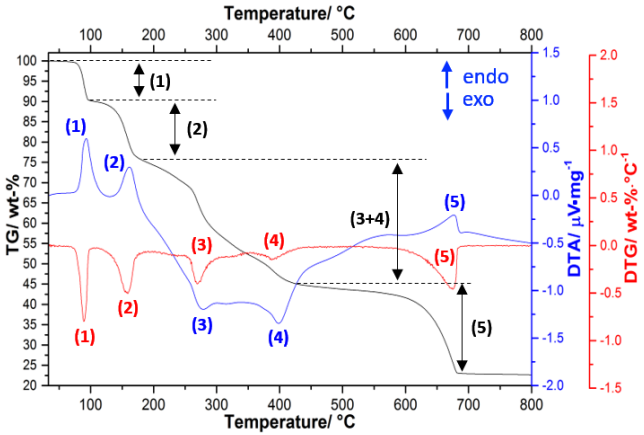

Figure 3.6. TG (black), DTG (red) and DTA (blue) curves for **1** measured in dynamic oxygen atmosphere. Adapted from [45].

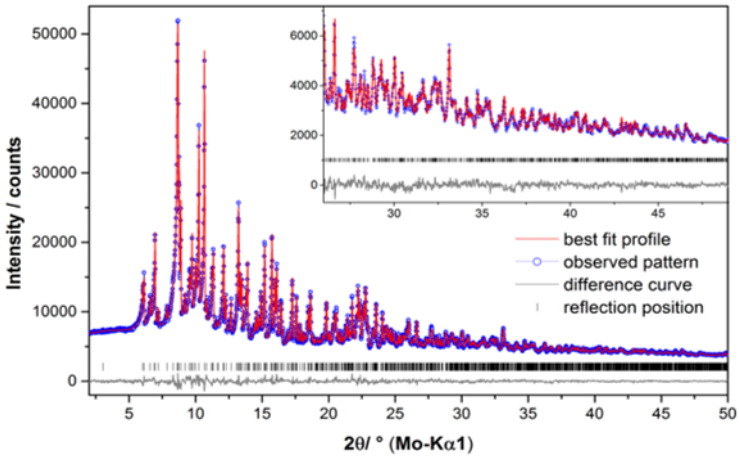

Figure 3.7. Rietveld plot of **1** at 30 °C. The observed pattern (blue circles, the best Rietveld fit profiles (red line) and the difference curve between the observed and calculated profile (grey line) are shown. Excerpt of the plot starting at 26° in 2θ is reported for clarity. Adapted from [45].

situ XRPD measurements were performed (Figure 3.8). Compound **1** was first heated in static air atmosphere from 30 °C to 200 °C to prove the formation of a less hydrated crystalline form (Figure 3.8, top) and then from 30 °C to 800 °C to compare it with the thermal analysis (Figure 3.8, bottom). It should be noted that temperatures deviate from those in TGA/DTA experiments due to the different atmospheres and sample environment(static and open capillary for the XRPD measurements, and dynamic and Al_2O_3 crucible for TGA/DTA). The first experiment shows the presence of **1**, stable up to 50 °C, transforming into a new phase, $Fe(gly)SO_4 \cdot 3H_2O$ (**2**), whose peaks gradually disappear at circa 150 °C. In the second experiment, performed using a different heating device, it was possible to observe the transition of compound **2** to the anhydrous form at 130 °C, which completely decomposes above 250 °C. After the decomposition, it was possible to observe the formation of $Fe_2(SO_4)_3$ (mikasaite) at 370 °C and Fe_2O_3 (hematite) at 510 °C.

By comparing the results from thermal analysis and *in situ* XRPD measurements, it was possible to observe and confirm many features like the for-

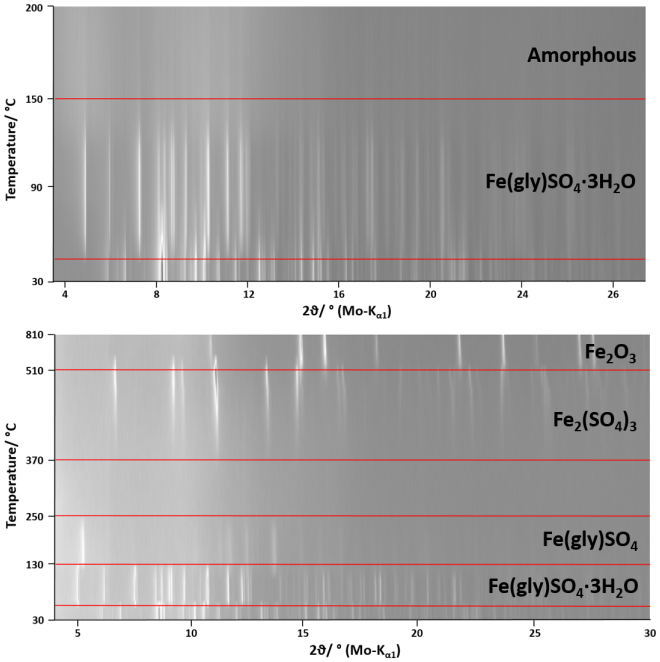

Figure 3.8. Temperature dependent *in situ* XRPD measurements of **1** performed in air atmosphere from 30 °C to 200 °C (top) and from 30 °C to 800 °C (bottom). Adapted from [45].

mation of a less hydrated structure (**2**) and the related anhydrous form. In the temperature range 180 °C - 450 °C, where the TG curve showed two poorly resolved weight losses, XRPD measurement did not show the presence of crystalline compounds meaning that the complex thermal process occurs in the amorphous state. Interestingly, in the first *in situ* XRPD experiment, it was observed the disappearance of crystalline peaks of **2** instead of the formation of the anhydrous form. This could be attributed to the formation of the anhydrous form in amorphous state, whose bio-availability could be higher than in the crystalline one.

Crystal structure determination of **2** was carried out by Simulated Annealing using the high resolution XRPD pattern at 100 °C collected from the

first *in situ* experiment. Compound **2** crystallizes in the monoclinic space group $P2_1/n$ with a = 9.0475(6) Å, b = 10.5825(6) Å, c = 10.4127(5) Å, β = 112.68(10) Å and V = 918.68(10) Å^3. The crystal structure is found to be isostructural with the Zn [63] and Co trihydrate compounds. As in compound **1**, two distinct octahedrally coordinated iron sites, located on centres of symmetry, can be observed: one iron site is coordinated by four water molecules and 2 glycine-related oxygen atoms ($[Fe(gly)_2(H_2O)_4]^{2+}$ complex ion) whereas the other one by two water molecules, two sulfate ions and two glycine ligands ($[Fe(gly)_2(SO_4)_2(H_2O)_2]^{2-}$ complex ion). All ligands coordinate to the iron in *trans* configuration with the glycine acting as a μ_2 bridging ligand between the two distinct iron sites. This coordination type allows the formation of 1D polymeric chains of different alternating complex ions running along the *b*-axis (Figures 3.9 - 3.10). Additional interactions support the chain motif, most likely hydrogen bonds, between sulfate ions and water molecules [$O(SO_4^{2-})\cdots O(H_2O)$ distance: 2.77 Å], and between water and glycine related oxygen atoms [$O(H_2O)\cdots O(gly)$ distance: 2.84 Å]. Inter-chain interactions are also observed: sulfate ions form potential hydrogen bonds with water molecules [$O(SO_4^{2-})\cdots O(H_2O)$ distances: 2.72, 2.92 and 2.98 Å] and glycines [$O(SO_4^{2-})\cdots H(gly)$ distances: 1.88 and 2.06 Å]. Hydrogen bonds involving exclusively water molecules are most likely present in the crystal structure as indicated by the $O\cdots O$ distance of 2.94 Å.

The study of the thermal behaviour of **1** showed the formation in the crystalline solid state of a less hydrated structure (**2**) and the related anhydrous form. However no information about how these processes occur at molecular level was extracted so far. Therefore, in order to understand the dynamics behind these phase transitions, an interpretation of the mechanism has been given herein. The analysis of the crystal structures of **1** and **2** shows that the transition between the two forms also involves a change in the coordination spheres of the iron sites. To better understand this transformation, we should consider the chain motif running along the crystallographic $[21\bar{1}]$ direction, which consists of alternating different complex ions with a distance between iron atoms of 9.15 Å (Figure 3.11, left). Upon heating, the sulfate

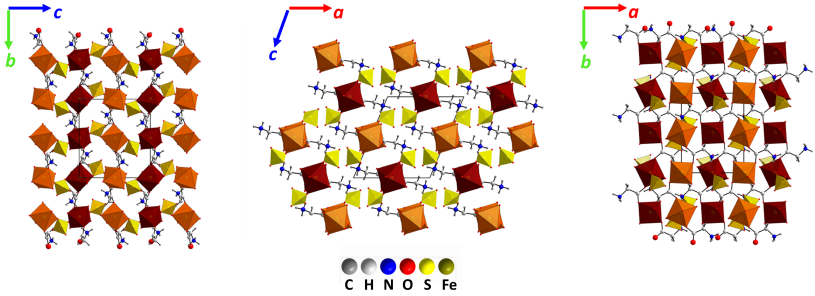

Figure 3.9. Projections of the crystal structure of **2** along *a*- (left), *b*- (middle) and *c*- (right) crystallographic axes. The two complex ions are depicted in different color. Adapted from [45].

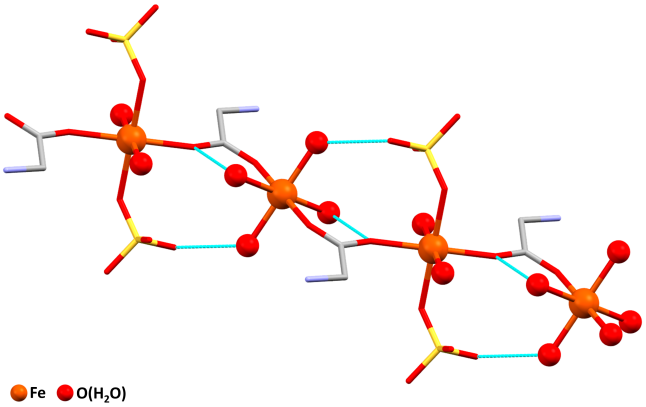

Figure 3.10. View of the 1D polymeric chain in **2**. Intra-chain interactions are depicted in light blue. Adapted from [45].

ions, close to the iron site, replace the two water molecules in equatorial position whereas the two water molecules in axial position are removed and the glycine ligands can bridge the two iron sites (light blue color in Figure 3.11). As a consequence, the iron sites move closer (Fe···Fe distance: 5.29 Å) and the characteristic chain motif in **2** is formed. Additionally, the glycine ligand acts as a spacer increasing the distance between the chains. During the transition to the anhydrous form, water molecules are completely removed from the coordination sphere of iron and replaced by sulfate-related oxygen atoms

leading to the condensation of FeO_6 octahedra. Consequently, the distance between iron sites is reduced (Fe···Fe distance: 3.82 Å) and the anhydrous compound is formed.

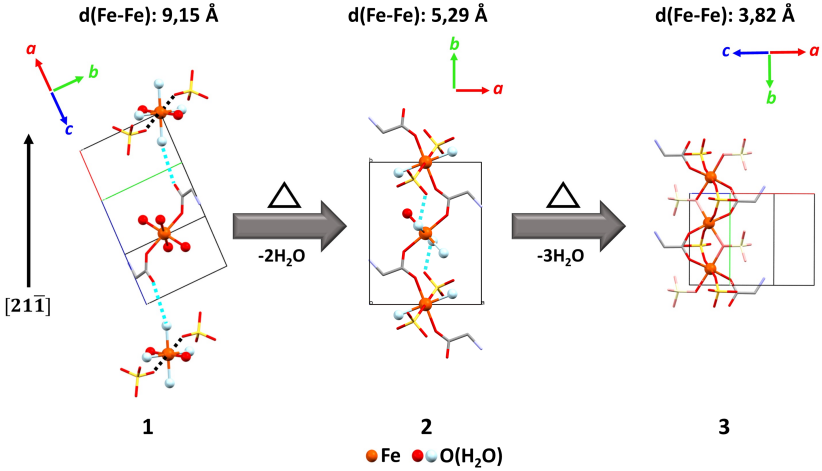

Figure 3.11. Representation of the transition from compound **1** (left) to the anhydrous (right) form through compound **2** (middle). The crystallographic [21$\bar{1}$] direction for **1** is also given. Released water molecules are depicted in light blue. Directions of the movements of the atom are highlighted in black for the sulfate ions and in light blue for glycines. Distances between iron atoms are reported as well. Adapted from [45].

3.1.3 Conclusions

Ferrous glycine sulfate pentahydrate, used in iron supplements, was characterized using several techniques and its thermal behaviour investigated. A large distribution of the particle sizes and the presence of traces of heavily scattering particles, by-products of the synthesis, were revealed by SEM coupled with BSE detector whereas the stoichiometry (Fe:S:N ratio) of the sample was confirmed by EDX. The use of IR spectroscopy with the attenuated total reflection (ATR) technique allowed to confirm the presence of the expected ligands, and indicates possible OH···O/NH···O hydrogen bonds

as well as the denticity of the glycine and its presence in zwitterionic form. The crystal structure of compound **1** was determined by Simulated Annealing from laboratory XRPD data and refined by Rietveld method. Its thermal behaviour was investigated by thermal analysis (TGA/DTA) and temperature dependent *in situ* XRPD measurements. This investigation revealed that the dehydration of **1** is a two-step process where **2**, whose crystal structure was determined by XRPD, is formed as intermediate. On further heating, it was observed that the decomposition of glycine and the oxidation of iron leads to $Fe_2(SO_4)_3$ (mikasaite) and then to Fe_2O_3 (hematite).

3.1.4 Experimental section

Sample

Capsules containing the industrially produced sample **1** were purchased from UCB Pharma GmbH, Germany (batch number 9868801).

Thermal Analysis

Coupled TGA/DTA measurements were carried out on a STA 449 F5-Jupiter (Netzsch) device. 35.7 mg of **1** was placed in an Al_2O_3 crucible and heated from 30 °C to 600 °C with a heating rate of 2 K/min whereas 31.8 mg of **1** was heated from 3 °C to 800 °C with a heating rate of 5 K/min. In both cases, measurements were carried out in a 20 mL/min oxygen stream. The TG curve of the second experiment was corrected measuring a standard (Al_2O_3).

Scanning electron microscopy (SEM/BSE/EDX)

SEM/BSE images and EDX analysis of **1** were obtained with TESCAN Vega TS 5130 MM equipped with x-Max^N 20 SDD (Oxford instruments).

IR spectroscopy

IR spectrum of **1** was recorded in ATR geometry on PerkinElmer Spectrum Two equipped with a diamond crystal. The background spectrum was measured separately and subtracted.

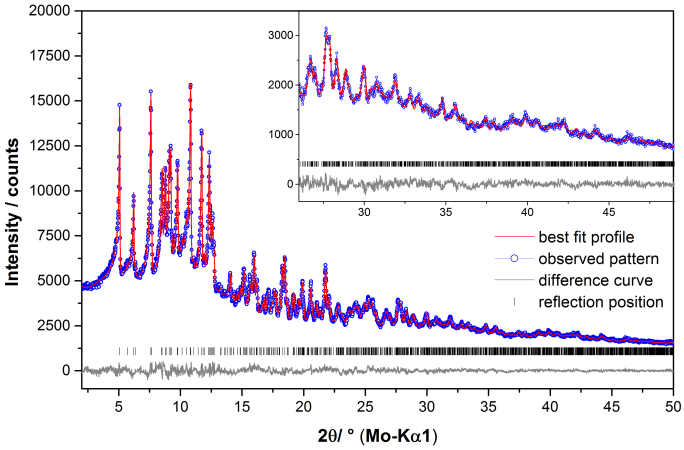

Figure 3.12. Rietveld plot of **2** at 100 °C. The observed pattern (blue circles, the best Rietveld fit profile (red line) and the difference curve between the observed and calculated profile (grey line) are shown. Excerpt of the plot starting at 26° in 2θ is reported for clarity.

Laboratory X-ray powder diffraction

All *ex situ* XRPD patterns were collected at room temperature on a laboratory powder diffraction diffractometer in Debye-Scherrer geometry (Stadi P Diffractometer, STOE) using Mo-$K_{\alpha 1}$ radiation from primary Ge(111)-Johann-type monochromator with 3 Mythen 1 K detectors (Dectris). All patterns were measured within the 2θ range from 0° to 110°.

Indexing, space group determination, Pawley refinement, crystal structure solution through Simulated Annealing and Rietveld refinement were performed with the program TOPAS 6.0 [64].

In situ X-ray powder diffraction measurements

Temperature dependent *in situ* XRPD measurements were carried out on two laboratory powder diffractometers in Debye-Scherrer geometry: Stadi P-Diffractometer (STOE), Mo-$K_{\alpha 1}$ radiation from primary Ge(111)-Johann-type monochromator, array of 3 Mythen 1 K detectors (Dectris) and Bruker D8-Advance, Mo-$K_{\alpha 1}$ radiation from primary Ge(220)-Johannson-type monochro-

Table 3.4. Crystallographic and Rietveld refinement data for compounds **1** and **2**.

Compound	**1**	**2**
Molecular Formula	$[Fe(H_2O)_6]\cdot[Fe(gly)_2(H_2O)_4]\cdot 2(SO_4)$	$Fe_2(gly)_2(SO_4)_2(H_2O)_6$
Sum formula	$C_4H_{30}N_2S_2O_{22}Fe_2$	$C_4H_{30}N_2S_2O_{22}Fe_2$
Molecular weight/g·mol^{-1}	634.10	549.84
Crystal system	triclinic	monoclinic
Space group (No.)	$P\bar{1}$ (2)	$P2_1/n$ (14)
Wavelength/ Å	0.7093	0.7093
a/ Å	5.9952(1)	9.0462(6)
b/ Å	6.8014(1)	10.5824(6)
c/ Å	13.4023(3)	10.4122(5)
α/ °	85.415(1)	90
β/ °	82.894(1)	112.849(4)
γ/ °	83.073(1)	90
V/ Å^3	537.16(2)	918.6(1)
T/K	298	373
Z	1	2
refined parameters	69	60
D_{calc}/g·cm^{-3}	1.96	2.03
R_{wp}/ % [a]	3.48	2.94
R_p/ % [a]	2.74	2.33
R_{Bragg}/ % [a]	1.65	1.08
Starting angle measured/ ° 2 θ	0	0
Final angle measured/ ° 2 θ	110	110
Starting angle used/ ° 2 θ	2	2
Final angle used/ ° 2 θ	50	50
Step width (° 2 θ)	0.01	0.01
Time (hrs)	3	3

[a] As defined in section 2.2.3.

mator, LYNXEYE detector (Bruker). For the experiment on the first device, the XRPD patterns were measured in a 2θ range from 2.0° to 110.0° applying a total scan time of 3h per measurement. The sample was heated, using an Oxford Cryosystem 500 device (Oxford Cryosystem), from 30 °C to 200 °C in 10 °C steps with a heating rate of 2 K/min and applying 30 min delay to ensure thermal equilibration of the sample. For the experiment on the second

device, the XRPD patterns were measured in a 2θ range from 2.0° to 41.0° applying a total scan of 2h per measurement. The sample was heated, using a TC-transmission furnace (MRI capillary heater), from 30 °C to 510 °C in 20 °C steps and from 510 °C to 810 °C in 50 °C steps with a heating rate of 5K/min and 10 min delay before each measurements.

Structural characterization

Ab initio structure solutions and Rietveld refinements of **1** and **2** were performed with the software TOPAS 6.0. The crystal structure were determined by the global optimization method of simulated annealing (SA) in real space. The profile function was described with the fundamental parameter approach implemented in TOPAS and the background was modelled using Chebyshev polynomials. The hump in the background caused by the capillary and small amounts of amorphous phase was described with a very broad Lorentzian type peak. Glycine and sulfate molecules were described using rigid bodies in *z*-matrix notation and their rotation and translation modes were let to refine. Distinct isotropic displacement parameters were applied for iron, glycine, sulfate and water (oxygen atoms) molecules. Hydrogen sites of water and glycine related nitrogen atoms were omitted due to the limits of the powder diffraction method. The final agreement factors are listed in table 3.4 and the fits of the XRPD patterns are shown in Figures 3.7 and 3.12.

3.2 Glycolaldehyde ammonia

Glycolaldehyde ammonia, a six-membered cyclic alkanolamine, was synthesized by BASF SE through the combination of glycolaldehyde with gaseous ammonia. The product was characterized by elemental analysis, SEM, vibrational spectroscopy (IR and Raman), and laboratory XRPD. A systematic analysis of the compound using PDF was carried out to confirm the results of the molecular and crystal structure identification and further investigate the short-range order. PDF and Rietveld co-refinement was performed to determine a robust model for the compound. Additionally, thermal behaviour was investigated with thermal analysis (TGA/DTA) and temperature dependent *in situ* XRPD. This work is in preparation for publication.

3.2.1 Introduction

Amines are an industrially important class of organic compounds [65]. They are formally derivatives of ammonia since they can be obtained by replacing one or more hydrogen atoms with different organic substituents [66]. Due to their chemical properties, amines are versatile compounds that can be used as building blocks for amino acids, pharmaceutical drugs, herbicides, agrochemicals, polymer additives, and surfactants.

Starting over more than a century ago, synthetic routes for the production of new amino compounds were designed using small precursors like ammonia and aldehydes. As an example, the combination of ammonia and formaldehyde [67, 68], the smallest aldehyde, results in the formation of hexamine, which is used in the production of resins, fuel tablets, explosives, vulcanization accelerators, anticorrosion agents, antibacterial agents, and preservatives [65]. When aliphatic aldehydes are used in the presence of ammonia, linear or cyclic amino compounds, such as alkanolamine or hexahydrotriazine, can be formed [65]. An example of formation of cyclic amines is the reaction of acetaldehyde with ammonia yielding crystalline triethylhexahydrotriazine trihydrate [69, 70].

In this work, a previously unknown cyclic amino alcohol compound, glycolaldehyde ammonia (2,4,6-Trihydroxymetil-1,3,5-triazinane, **1**), recently synthesized at BASF SE from the combination of glycoaldehyde and ammonia, is presented. The aim of this project was to consistently investigate a relatively small organic molecule using, besides techniques like IR and Raman spectroscopy, electron microscopy (SEM), and thermal analysis (TGA/DTA), XRPD and PDF. The potential of XRPD and PDF analyses, individually and combined, was exploited to extract information about the short, medium and long-range order of the target organic molecule.

3.2.2 Results and discussion

The molecular structure of compound **1** was initially investigated by elemental analysis and solid state NMR by BASF SE. The first analysis showed a chemical composition of $C_6H_{15}N_3O_3 \cdot H_2O$ indicating the presence of water. NMR identified two possible molecular models (Figure 3.13). The first model

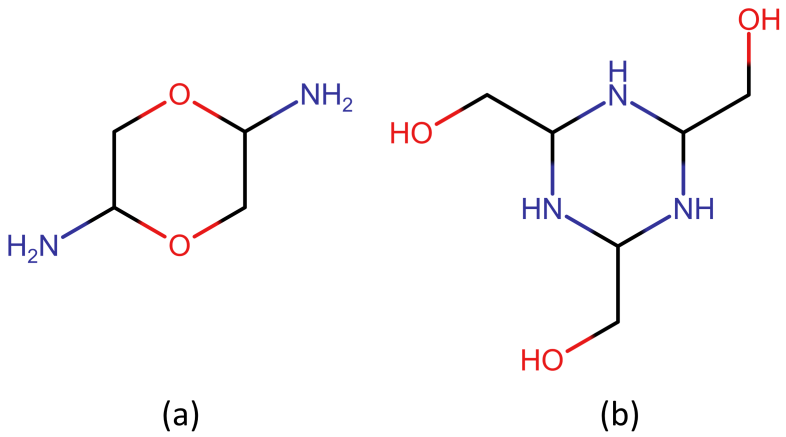

Figure 3.13. Representation of the two proposed molecular models: model 1 (a) and model 2 (b).

(model 1) consists of a six-membered ring with two condensed oxygen atoms, and two amine groups linked to the carbon atoms (Figure 3.13,a). The second

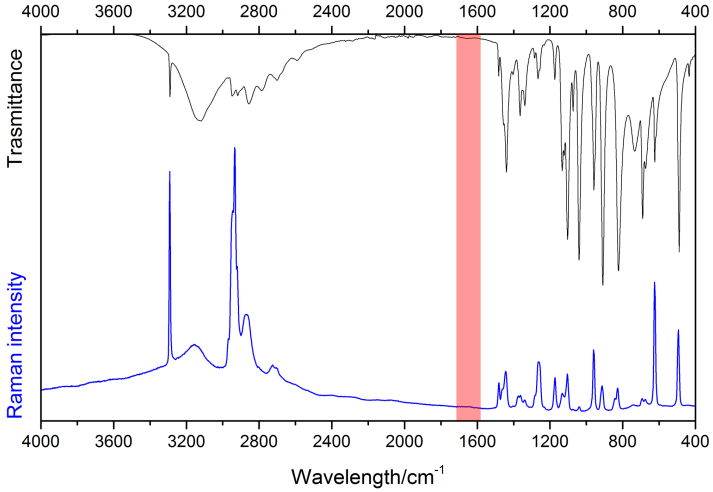

Figure 3.14. IR (black) and Raman (blue) spectra of **1**. The area of the spectra where no visible band related to the presence of secondary ammines is highlighted in red.

model (model 2) consists of a six-membered ring with three condensed nitrogen atoms, and three hydroxymethyl groups connected to the carbon atoms (Figure 3.13,b). Since one of the differences in the two models is the presence of primary (model 1) and secondary amines (model 2), IR and Raman spectra were collected (Figure 3.14). After a tentative band assignment (Table 3.5) using spectroscopic results of related structures [71–78], the spectra showed stretching bands above 3000 cm^{-1} corresponding to O-H/N-H groups and excluded the presence of possible structural water, as it is observed by thermal analysis (Figure 3.24). More importantly, the vibrational spectra do not show any band in the region around 1600 cm^{-1} (Figure 3.14) excluding the presence of secondary amine groups and, consequently, the proposed molecular model 1.

The angular shaped crystalline particles with dimensions ranging from 5 to 60 µm, as observed through SEM (Figure 3.15), were analysed by XRPD in order to determine the crystal structure and unambiguously confirm the presence of one of the two proposed molecular models. Structure solution through

Table 3.5. Band assignment for IR and Raman spectra for **1**.

Position, cm^{-1}, shape		
IR	**Raman**	**Assignment**
3290, s	3292, vs	OH/NH stretching, NH stretching
-	3153, vbr	OH stretching/water NH stretching
3129, vbr	-	OH stretching, NH stretching
-	2969, sh	CH stretching
2949, w	2945, sh	CH/CH_2 stretching
-	2934, vs	CH stretching
2918,w	2920 sh	$CH_{2\ sym}$, $CH_{2\ asym}$, CH stretching
-	2871, m	CH/CH_2 stretching
2857, br	-	CH stretching
2784, br	-	
-	2727, br	
2703, br	2705, sh	CH_2 bending
2590, br		
1482, w	1480, m	CH_2bending
1456, sh	1462, sh	
1440, s	1445, m	CH_2 bending
1403, w	-	
-	1375, m	NH/CH_2 bending, CN stretching
1365, m	1362, m	
1338, m	1339, m	HCCN/ R_{sym}/ CCH bending
1285, w	-	
1266, m	1262, s	COH/CH_2 bending
1258, sh	-	
1174, m	1172, sh	
1133, s	1132, sh	CC/CN stretching, CH bending
1122, s	-	
1103, vs	1105, s	CC/CN/CO stretching, CH_2/ HCCN/ R bending
1073, m	-	R/CO stretching, R deformation
1040, vs	1040, w	CN stretching, CH bending, R deformation
959, s	960, s	C-OH stretching
910, vs	913, m	CC stretching, CH_2/R_{sym} bending
-	843, sh	CNCC/R_{sym}/CH_2 bending
823, vs	829, m	CH/CNCC/R_{asym}/CH_2/NH bending
734, br	-	N-H bending
690, s	693, w	
674, sh	673, w	
624, s	624, vs	
617, sh	-	
490, vs	493, s	Lattice modes
435, w	-	
-	354, m	
-	327, w	
-	281, w	
-	221, w	

vs: very strong, s: strong, m: medium, br: broad, vbr: very broad, sh: shoulder, w: weak.

ab initio simulated annealing against laboratory XRPD data revealed that the compound crystallizes in the orthorhombic space group *Ama*2 with lattice parameters *a*= 12.1054(2) Å, *b*= 13.5537(2) Å, *c*= 5.20741(8) Å, *V*= 854.40(2) Å^3. All crystallographic and Rietveld refinement data are listed in Table 3.8 while the Rietveld fit is depicted in Figure 3.25. The projections of the crystal packing along the three crystallographic axes are depicted in Figure 3.16. The inspection of the crystal structure confirmed the second proposed molecular model and revealed the unit cell containing four molecules with the backbone ring parallel to the *ab* plane and the hydroxymethylgroup almost parallel to the *c*-axis. The asymmetric unit consists of half molecule that is completed by the mirror plane perpendicular to the *b*-axis. In the crystal, the molecules are stacked in columns along the *c*-axis with an intermolecular distance of 5.21 Å, which corresponds to the *c*-axis. The molecules interact via inter- and intra-columnar hydrogen bonding networks. The intracolumnar interactions consists of CH$\cdots$O hydrogen bonds (C-O distance: 3.51 Å, CHO angles: 152.8°-152.6°) involving the hydrogen attached to the carbon atom in the backbone ring and the hydroxyl oxygen atom (Figure 3.17, a). The inter-

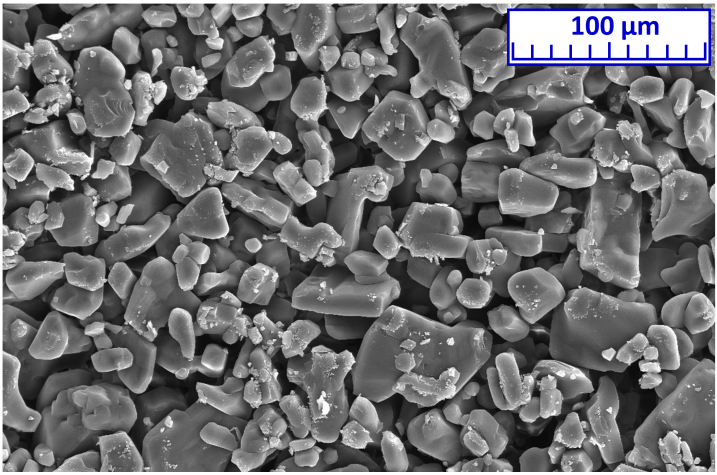

Figure 3.15. SEM image of **1** showing angular shaped crystalline particles with dimensions in the range of 5-60 µm.

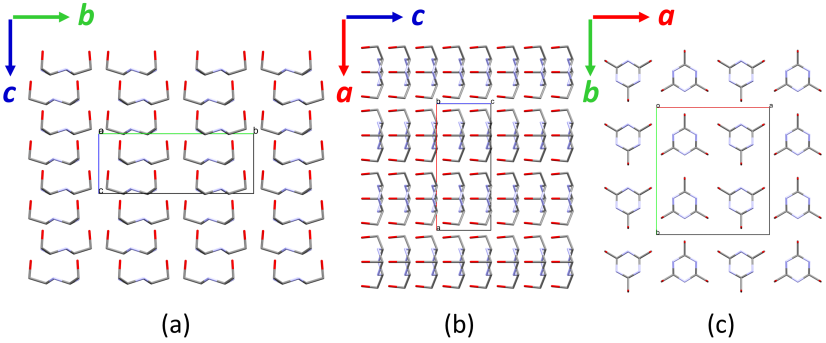

Figure 3.16. Projections of the crystal structure of **1** along the crystallographic *a*- (a), *b*- (b) and *c* (c)-axes.

columnar interactions are made up of N-O hydrogen bonds (distance: 2.8-2.9 Å) involving the nitrogen atom of the backbone ring and the hydroxyl oxygen atom (Figure 3.17, b). In addition, contrary to the results from the elemental analysis, the absence of voids (probe radius: 1 Å) further excludes the presence of structural water.

Since structure solution from XRPD gives only an average structural

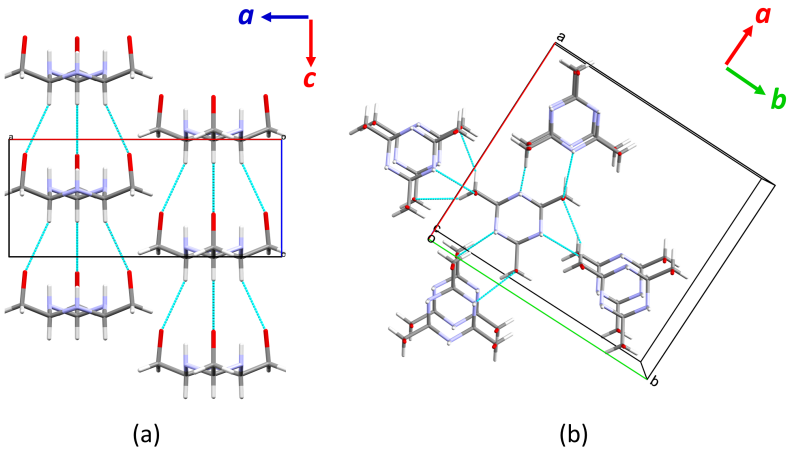

Figure 3.17. Representation of the intracolumnar (a) and intercolumnar (b) interactions in **1**. The interactions are depicted in blue.

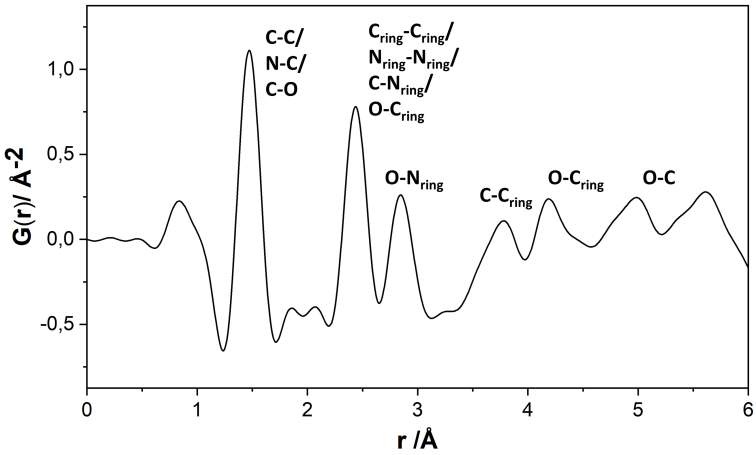

Figure 3.18. Experimental PDF of **1**. The atomic pairs for each signals are also assigned.

model of the molecule in the crystal and deviations from the model at low concentration level are difficult to observe, a detailed study of the molecular conformation was performed by PDF analysis. In addition, PDF analysis was used to extract more accurate molecular conformation since, due to the high symmetry of the crystal and the use of a rigid body as scaffold for the molecule, values of the bond lengths, angles and torsions were constrained during the refinement.

PDF plot of **1** was obtained from synchrotron total scattering XRD data (Figure 3.18). Excluding the peak at 0.83 Å, which is a termination effect due to the truncated Fourier transform of the measured data, the first peak can be observed at circa 1.46 Å, which corresponds to C-C/C-N/C-O bonds. The peaks at around 2.43 Å and 2.85 Å correspond to atomic pairs C_{ring}-C_{ring}, N_{ring}-N_{ring}, C-N_{ring}/O-C_{ring}, and O-N_{ring}, respectively while peaks at 3.78 Å, 4.19 Å, and 4.99 Å are assigned to C-C_{ring}, O-C_{ring}, and O-C pairs, respectively. Contribution from pairs containing hydrogen were not clearly visible due to the low scattering power of the hydrogen atom for X-rays. The feature around 1.05 Å may contain information from C/N/O-H bond pairs but is

highly correlated to errors at low-*r* due to the data reduction procedure, which can create artefacts close to this distance range (such as a variation of Q_{max}). However, this peak position agrees with the expected average of the C/N/O-H distances (C-H ∼1.09 Å, N-H ∼1.0 Å and O-H ∼0.9 Å) [79].

The rigidity of the molecular conformation of **1** and the presence of possible conformation errors were investigated by probing the short-range order using PDF analysis. Different conformers were generated using the software Mercury from the Cambridge Crystallographic Data Center (CCDC) [80]. The possibility of a boat conformation for the ring, less stable than the chair one [81] and usually observed when hindered substituents are present [82,83], was excluded from the investigation. Three conformers were obtained (Figure 3.19) and their PDFs were obtained from simulated scattering intensities using the Debye equation [84, 85]. The simulated PDF plots were compared to the observed PDF, and to the simulated PDFs of the isolated single molecule from the XRPD refinement and of the intermolecular pairs (Figure 3.20). The analysis excludes the presence of alternative conformations since their PDFs

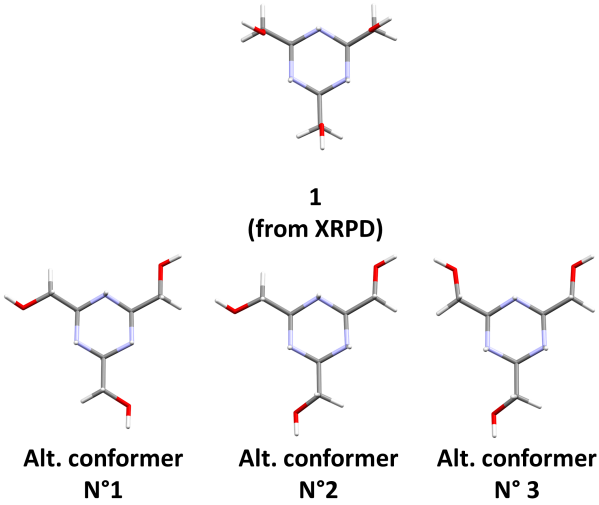

Figure 3.19. Representation of the molecular structure of **1** and of the alternative conformations simulated with the software Mercury.

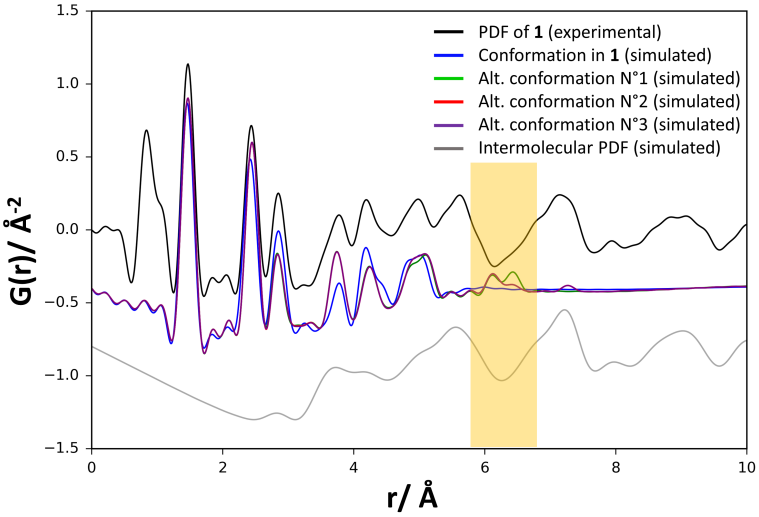

Figure 3.20. Comparison of the experimental PDF of **1** (black) with the simulated PDFs of the isolated molecules obtained from the XRPD model (blue) and from the alternative conformers (green, red, purple). The simulated PDF accounting for the intermolecular correlations in **1** (grey) is also reported. The difference in the PDFs between 6-7 Å is highlighted in yellow.

show features between 6-7 Å that are not evident in the measured data. Therefore, it is unlikely that conformational errors exist at any significant concentration, and the fidelity of the primary conformation can be confirmed.

To obtain a good model of the molecule and to observe any deviation from the structural model obtained from XRPD analysis, several refinements against the PDF curve were carried out. Three slightly different models with different crystal systems and space groups were sequentially investigated with the aim of monitoring the change of the local structure and the quality of the fit as function of the symmetry in the model. In all three cases, when not constrained by symmetry, bond lengths, and torsion and bond angles were allowed to refine. To describe the *r*-dependent peak width in the PDF, affected by thermal vibration and disorder, different strategies are described in literature [86–88]. Due to the rigidity of the molecular conformation, and

the use of restraints for bond lengths and torsions to address the remaining flexibility, it was decided to not over-parametrize the refinements. Therefore, two different isotropic thermal displacement factors for non-hydrogen (B_{eq_1}) and hydrogen atoms (B_{eq_2}) as well as one additional parameter for all non-H atoms and for the X-H covalent bonds in the same molecule (B_{intra_1}) were used. Crystallographic and fit data determined by PDF analysis are listed in Table 3.6.

The first model, similar to the one used for structure solution and Rietveld refinement, was built in the space group *Ama*2. It consists of a half molecule, treated as rigid body, located on special position (mirror plane). The refinement of the model to the PDF curve is consistent with the result from Rietveld refinement and it gives a good agreement (R_{wp}= 17.3%) with the experimental data in the long-range order but a only decent agreement in the short-range order (Figure 3.21, a). This can be attributed to the actual local structure of the compound, which is different from the averaged one obtained from Rietveld refinement.

To increase the degree of freedom of the molecules in the unit cell, which are constrained by symmetry, a second model was built. This model is com-

Table 3.6. Parameter values determined by PDF refinement of the three models in the range 1.2-15 Å and 1.2-70 Å for **1**.

Model No.	**#1**		**#2**		**#3**	
Crystal system	Orthorhombic		Monoclinic		Triclinic	
Space group	*Ama*2		*C*2		*P*1	
a/ Å	12.114(2)	12.114(5)	13.5570(8)	13.567(6)	13.5578(9)	13.565(8)
b/ Å	13.550(2)	13.637(3)	5.2103(3)	5.201(2)	5.2077(3)	5.207(3)
c/ Å	5.2087(7)	5.197(3)	12.1112(7)	12.140(4)	12.1125(7)	12.120(6)
α/ °	90	90	90	90	89.96(3)	90.1(3)
β/ °	90	90	90.05(2)	90.3(2)	90.03(3)	90.0(2)
γ/ °	90	90	90	90	90.09(3)	90.2(3)
V/ Å^3	854.9(2)	858.6(7)	855.49(9)	856.7(6)	855.2(1)	856.0(8)
T/ *K*	298		298		298	
Refined parameters	16		24		47	
R_{wp} % [a]	17.3	14.6	13.3	10.3	13.0	9.8
Starting '*r*'-range used/ Å	1.2	1.2	1.2	1.2	1.2	1.2
Final '*r*'-range used/ Å	70	15	70	15	70	15

[a] As defined in section 2.2.3.

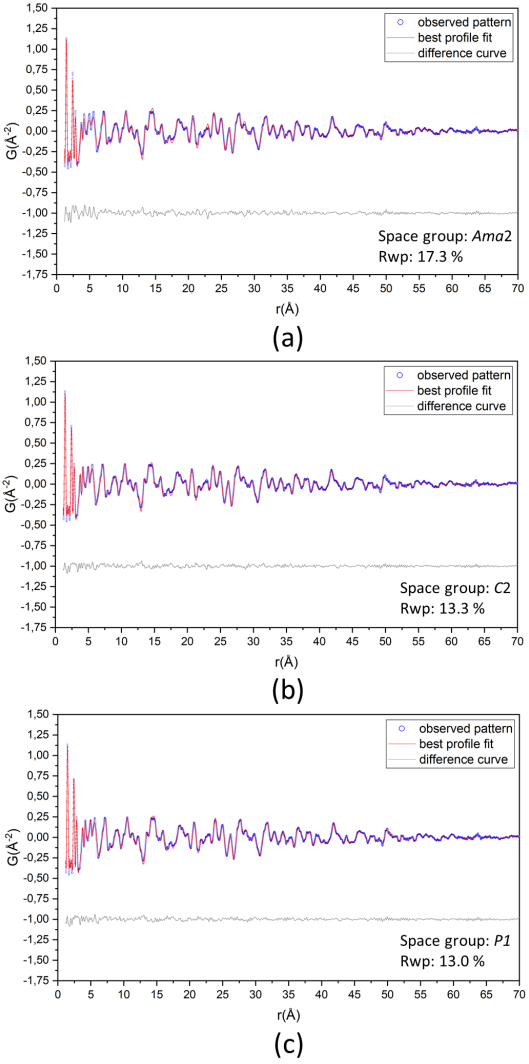

Figure 3.21. PDF fits of the models with *Ama*2 (a), *C2* (b) and *P*1 (c) space groups for **1** in a 'r'-range from 1.2 to 70 Å. The blue circles and red solid line correspond to measured and simulated PDFs, respectively. The grey solid line offset below denotes the difference curve.

posed of one molecule, treated as rigid body, with the space group *C*2. Contrary to the previous model, the molecule can rotate and translate in the unit cell without breaking the crystallographic symmetry. The refinement of the model to the PDF curve gives a very good agreement with the experimental data in the long-range order and this time, the quality of the fit in the short-range order shows a substantial improvement with an R_{wp} of 13.3% (Figure 3.21, b).

The last model is composed by four crystallographically independent molecules with the space group *P*1. In this model, the four molecules can independently rotate and translate without obeying any symmetry constraints. As a result, the refinement of this model to the experimental PDF curve slightly improved giving the best fit among the three models (Rw=13.0%, Figure 3.21, c).

In addition, PDF refinements in the range 1.2-15 Å were also carried out in the same way as a further attempt to exclusively focus on the local struc-

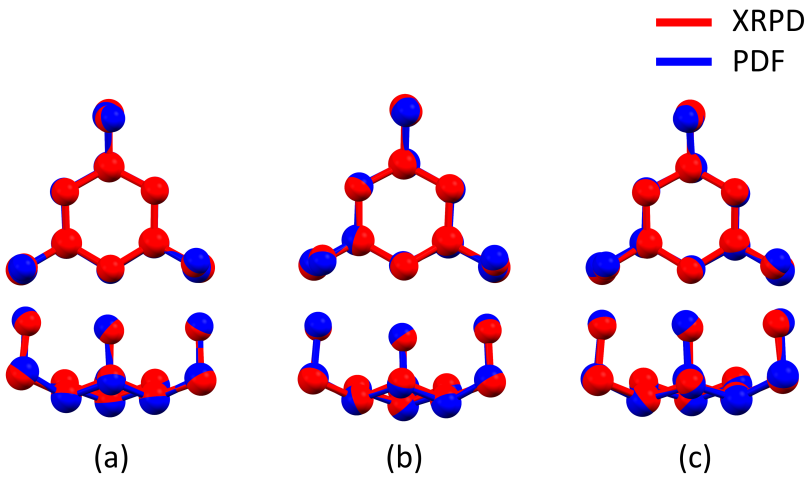

Figure 3.22. Superimposition of the molecular structure from XRPD (red) with those obtained from PDF fitting in the range 1.2-15 Å (blue) using the space groups *Ama*2 (a), *C*2 (b) and *P*1 (c). The RMSDs are 0.0805, 0.087 and 0.0912, respectively.

ture.

However, although the structural model in $P1$ space group shows a very good agreement with the observed data, the molecular conformation in all three investigated models does not remarkably deviate from the model obtained from XRPD (Figure 3.22).

A XRPD/PDF co-refinement was performed with the aim of obtaining one single model containing precise lattice parameters and arrangement of the molecules extracted from the Rietveld refinement, and accurate molecular conformation and bond lengths extracted from PDF analysis. The crystallographic and refinement parameters are listed in Table 3.7. Before carrying this co-refinement out, a weighting factor was chosen so that both real and reciprocal space datasets could equally contribute to the refinement and give the optimal result. Several refinements were carried out using different weighting factors for the PDF fitting and the agreement factor, R_{wp}, for both refinements was checked. The results obtained from the test are depicted in Figure 3.23, which reveals the suitable weighting factor for the best agreement between the two techniques with these datasets. The obtained value (10^5) almost ap-

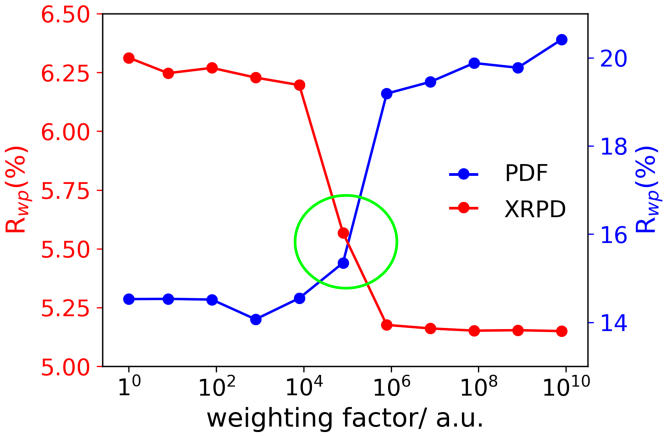

Figure 3.23. Agreement factors (R_{wp}) obtained from the co-refinement as function of the used weighting factor. The best value is highlighted by a green circle.

Table 3.7. Crystallographic and refinement parameters of **1** for the XRPD/PDF co-refinement.

Crystal system	Triclinic
Space group	*P*1
a/ Å	13.5545(1)
b/ Å	5.20787(5)
c/ Å	12.1060(1)
α/ °	90.027(3)
β/ °	90.022(4)
γ/ °	89.970(4)
V/ Å^3	854.58(1)
R_{wp} % for XRPD [a]	5.28
R_{wp} % for PDF [a]	15.8

[a] As defined in section 2.2.3.

proaches to the difference between the integrated intensity of the XRPD pattern (I_{XRPD}) and the PDF (I_{PDF}) multiplied by 10 ($I_{XRPD}/(I_{PDF}\cdot 10)$). This strategy was performed by refining the model in *C*2 space group and the weighting factor was applied for the co-refinement with the model in *P*1 space group.

Thermal behaviour was investigated by performing coupled TGA/DTA and temperature-dependent *in situ* XRPD measurements. The thermal analysis (TGA/DTA) (Figure 3.24,a) shows thermal stability up to 100 °C followed by several mass loss steps, which are overlapped and difficult to separate. The TGA-curve does not show any weight loss step related to water molecules and confirms the anhydrous model obtained from XRPD. At 100 °C, overlapped weight losses, associated with endothermic peaks, are observed. This likely corresponds to the decomposition of the sample, which is also unstable for a certain period of time (around 1-2 weeks) at room temperature. At 650 °C, the sample is completely decomposed and due to the oxygen atmosphere, no residue is observed at the end of the measurement. Temperature-dependent *in situ* XRPD measurements (Figure 3.24,b) confirmed the thermal stability up to circa 100 °C, where the sample decomposed and Bragg peaks disappeared. Since no crystalline phases are observed, it can be concluded that the decomposition event only occurs in the amorphous state.

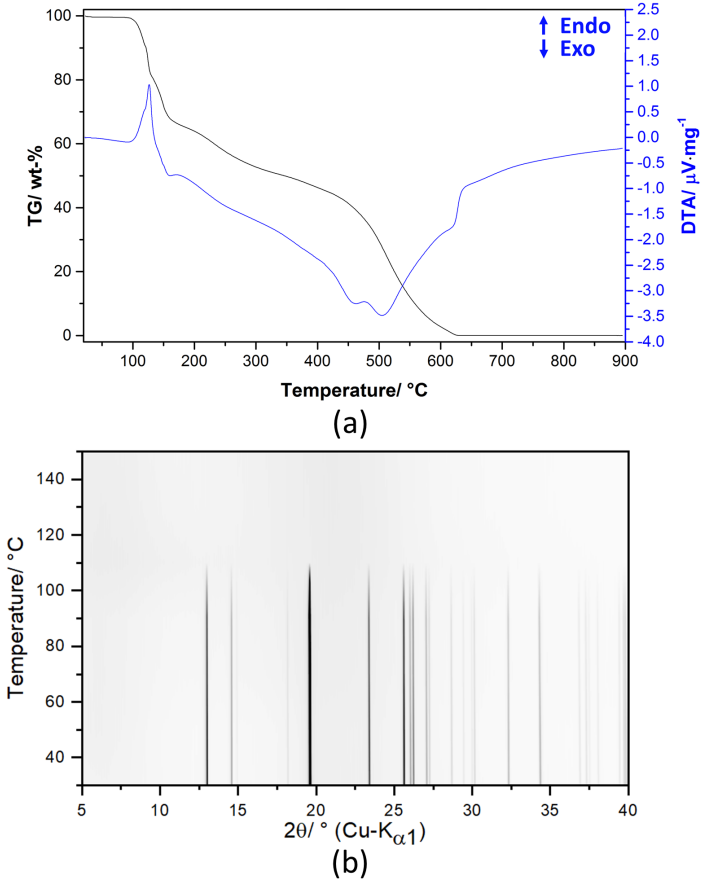

Figure 3.24. TG (black) and DTA (blue) curves for **1** measured in dynamic oxygen atmosphere (a) and temperature-dependent *in situ* XRPD measurements of **1** performed in air atmosphere (b).

3.2.3 Conclusions

Compound **1**, which could be used in the future as a build block for pharmaceuticals or as an additive, was synthesized at BASF SE from the combination of glycoaldehyde and ammonia. After an initial characterization by elemental analysis, NMR, and IR performed at BASF SE, the molecular

structure was confirmed by crystal structure determination using laboratory XRPD data and synchrotron X-ray PDF analysis. The crystal structure shows a columnar arrangement of the molecules along the *c*-axis. Thermal analysis (TGA/DTA) and temperature-dependent *in situ* XRPD measurements tracked the thermal profile of **1** showing the loss of crystallinity and decomposition above 100 °C. This work offered a route that can also be used for the investigation of cyclic and macrocyclic compounds in cases where the molecular conformation cannot accurately be determined. The use of PDF analysis allows in particular to study low crystalline or amorphous compounds.

3.2.4 Experimental section

Synthesis process

The synthesis of **1** was performed by BASF SE Company. Gaseous glycolaldehyde was provided by evaporation of an aqueous solution of the glycolaldehyde dimer in THF (7.5 wt.-% glycolaldehyde dimer, 11.5 wt.-% THF, 80 wt.-% water and 1 wt.-% tetraglyme) by heating the solution to 160 °C in a tube evaporator comprising Raschig-rings. The gaseous feed was fed into an unheated reaction chamber operated at ambient pressure. Gaseous ammonia at room temperature was also fed to the reaction chamber through a separate inlet. It was observed that colorless crystals formed at the cooler parts of the reaction chamber. At the cooler, bottom of the reaction chamber, a yellow-brownish clear solution condensed from the gas phase. The product solution was drawn-off from the bottom of the reaction chamber through a valve. The product solution was analyzed through gas chromatography (GC) and yielded a distinct product peak, which was identical to the peak obtained by performing a GC on the crystals. The other substances in the product solutions were identified to be the solvents (THF, water, tetraglyme) from which the glycolaldehyde was evaporated from excess ammonia. The total yield of conversion products of glycolaldehyde and ammonia, including the triazinane, was about 73%.

Infrared spectroscopy (IR)

Infrared spectrum of 1 was recorded in attenuated total reflection (ATR) geometry on a PerkinElmer Spectrum Two equipped with a diamond crystal. The background spectrum was measured separately and subtracted.

Raman spectroscopy

Raman spectrum of 1 was recorded in transmission geometry using a Horiba iHR320 Imaging Spectrometer with a laser (λ=633 nm) as excitation source.

Scanning electron microscope (SEM)

SEM images of 1 were obtained with a TESCAN Vega TS 5130 MM equipped with X-MaxN 20 SDD (Oxford instruments). The sample was spattered with gold nanoparticles before the analysis.

Thermal analysis

Thermal analyses were carried out using a STA 449 F5-Jupiter (Netzsch) device for TGA- and DTA-measurements. The sample were placed in an Al_2O_3 crucible and heated up from 30 °C to 800 °C with a heating rate of 5 °C/min in in a 20 mL/min O_2-stream. An empty crucible was used as reference material. After cooling down to room temperature, the residue of the thermal decomposition was transferred into a 0.5 mm diameter borosilicate glass capillary (WJM-Glas/Mueller GmbH), which was sealed and analysed by X-ray powder diffraction (see below). The TGA-curve was corrected using the data of a standard (Al_2O_3), which was measured with the same temperature program.

Laboratory X-ray powder diffraction

The X-ray powder diffraction pattern of **1** used for crystal structure solution and Rietveld refinement was collected at room temperature on a laboratory powder diffractometer in Debye-Scherrer geometry (Stadi-P Diffractometer (Stoe), Cu-$K_{\alpha 1}$ radiation from primary Ge(111)-Johann-type monochromator, 3 Mythen 1K detectors (Dectris)). The sample was gently ground and filled in a 0.5 mm diameter borosilicate glass capillary (WJM-Glas/Mueller GmbH), which was spun during the measurements. A total scan time of 12

Table 3.8. Crystallographic and Rietveld refinement data for compound **1**.

Compound	**1**
Sum formula	$C_6H_{15}O_3N_3$
Molecular weight/ g·mol^{-1}	117.19
Crystal system	Orthorhombic
Space group (No.)	*Ama*2 (40)
Wavelength/ Å	1.5406
a/ Å	12.1054(2)
b/ Å	13.5537(2)
c/ Å	5.20741(8)
V/ Å^3	854.40(2)
Z	4
T/K	298
Refined parameters	34
D_{calc}/ g·cm^{-3}	1.35
R_{wp}/ % [a]	6.51
R_p/ % [a]	4.27
R_{Bragg}/ % [a]	5.30
Starting angle measured/° 2θ	0
Final angle measured/° 2θ	110
Starting angle used/° 2θ	5
Final angle used/° 2θ	100
Step width/° 2θ	0.01
Time/ h	12

[a] As defined in section 2.2.3.

hours was applied and the pattern was measured over a 2θ range from 0° to 110°. Temperature dependent *in situ* XRPD measurements were carried out on a Bruker D8-Advance powder diffractometer in Debye-Scherrer geometry with Cu-$K_{\alpha 1}$ radiation from primary Ge(111)-Johannson-type monochromator and Våntec detector. The sample was loaded into a 0.7 mm diameter glass capillary, which was spun during the measurements. The patterns were measured in a 2θ range from 2.0° to 60.0°. A total scan time of 3 hours was applied per each measurement. The temperature was adjusted using a TC-transmission furnace (mri). The sample was heated from 30 °C to 150 °C in 20 °C steps with a heating rate of 5 °C/min. During each step, a diffraction

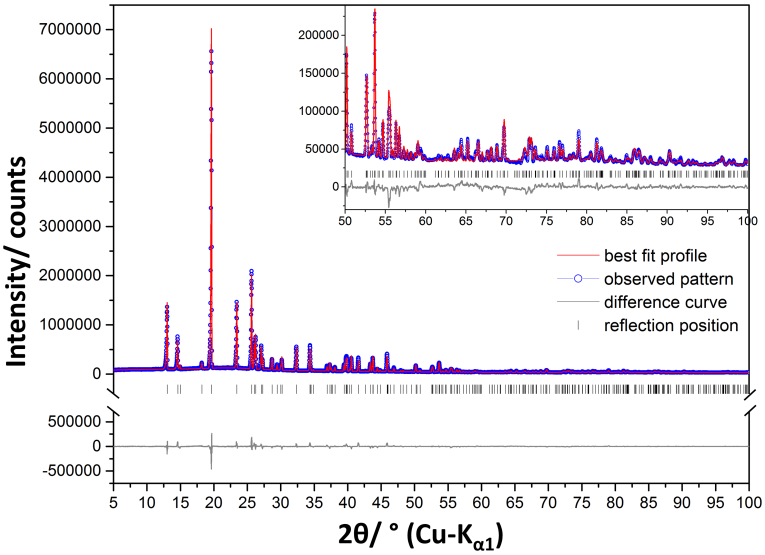

Figure 3.25. Rietveld plot of **1** at ambient condition. The observed pattern (blue circles, the best Rietveld fit profile (red line) and the difference curve between the observed and calculated profile (grey line) are shown. Excerpt of the plot starting at 50° in 2θ is reported for clarity.

pattern was collected, after a delay time of 5 minutes to ensure thermal equilibration of the sample.

Indexing, space group determination, Pawley refinement, crystal structure solution through Simulated Annealing and Rietveld refinement were performed with the program TOPAS 6.0 [64].

Pair distribution function

Experiments were carried out using beamline P02.1 at the Petra III synchrotron (DESY). The diffraction dataset was collected at room temperature using a 2D Perkin Elmer XRD1621 (2048 x 2048 pixels and 200 x 200 μm pixel size) with sample-to-detector distance of 303.66 mm. The incident wavelength of the X-rays was λ = 0.207 Å (60 keV). Calibration of the experimental setup was performed using a silicon standard sample. The in-

vestigated powder was loaded into a 1 mm Kapton capillary and an empty Kapton capillary was used as background. Raw 2D data were corrected for geometrical effects and polarization, then azimuthally integrated to produce 1D scattering intensities versus the magnitude of the momentum transfer Q (where $Q = 4\pi \sin\theta/\lambda$ for elastic scattering) using the program Fit2D [89]. The program xPDFsuite [90] was used to perform the background subtraction, further corrections, and normalization to obtain the reduced total scattering structure function F(Q), and Fourier transformation to obtain the pair distribution function (PDF), G(r).
PDF refinements were performed with the program TOPAS 6.0 [64].

4 Giant anisotropic thermal expansion

This chapter is dedicated to the thermal expansion analysis of five compounds belonging to two classes of compounds: photosalient crystals and metal organic frameworks (MOFs). The first part gives a brief introduction of the anisotropic thermal expansion phenomenon of materials, whereas the second part deals with three isotypical copper complexes showing photosalient behaviour. The last part focuses on two isotypical interpenetrated MOFs where one compound undergoes structural transformation.

4.1 General aspects

Materials change their shape, area, and volume in response to external stimuli, such as temperature. In general, they expand along all three directions upon heating (positive thermal expansion, **PTE**). A typical example of a well-known material showing this property is mercury, which has been widely used in thermometers.

However, certain compounds deviate from this tendency. Negative thermal expansion (**NTE**) occurs when a materials exhibits compression upon heating [91]. This phenomenon can be observed in ice in the range 0-4 °C, where the density is smaller than liquid water, and in the range 10-75 K [92]. Interestingly, it has also been demonstrated that a small number of solids

does not expand at all along one of the axes, *i.e.* zero thermal expansion (**ZTE**) [93]. When the expansion does not occur equally along all three directions, anisotropic thermal expansion can be observed. In these cases, the analysis of the deviations of the axes allows to reveal this effect and few combinations can be possible: PTE along all directions but with difference magnitude, combined PTE/NTE or ZTE along one direction compensated by PTE and NTE.

The study of thermal expansion is very important. Prominent examples are railway tracks or bridges, where expansion during summer and contraction during winter occur. A careful analysis of the expansion helps to prevent undesired effects, which can lead to serious consequences. Furthermore, many applications in different fields like sensors, artificial muscles [94], and temperature-sensitive drug delivery systems [95] can be found.

However, in order to design new materials with improved properties, the knowledge of the underlying mechanism is fundamental. Possible mechanisms behind this phenomenon can be *e.g.* conformational changes [93, 96], packing rearrangement [97], host-guest interactions [98, 99], and geometric flexibility [100] (Figure 4.1).

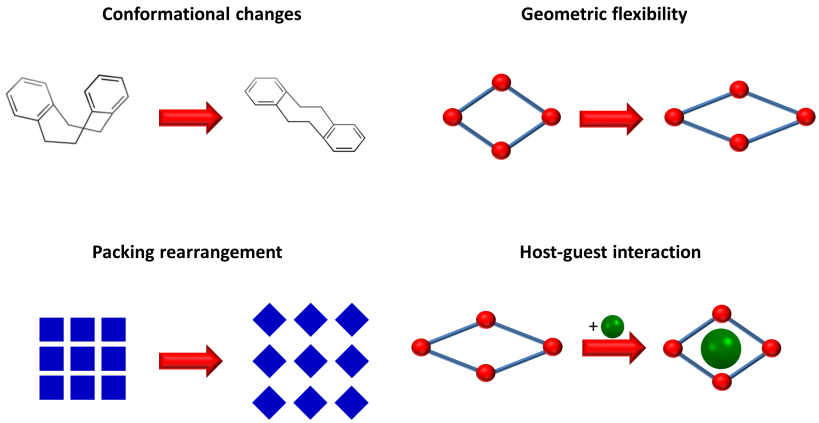

Figure 4.1. Schematic plot showing certain mechanisms involved in anisotropic thermal expansion.

To estimate the thermal expansion, the coefficient of thermal expansion (CTE) of the volume and along the axes must be calculated. This coefficient (α) is calculated by dividing the variation of the volume or the axes (x) by the change in temperature (T) at constant pressure (4.1).

$$\alpha_x = \frac{1}{x}\left(\frac{\partial x}{\partial T}\right)_p \tag{4.1}$$

In crystalline compounds, calculating CTE along the crystallographic axes can be misleading. Considering only the variation of the crystallographic axes in non-orthogonal crystal systems (*i.e.* trigonal, hexagonal, monoclinic, and triclinic) may not provide an accurate picture of the actual expansion behaviour, since the expansion or compression involves also changes in the crystallographic angles. Since the unit cell is not unique but a conventional construct, it is possible to have different unit cells for the same crystal structure. For example, if we consider a simplified system, such as a two-dimensional molecular framework, where a 'wine-rack'-like expansion [101] is involved, two unit cells can be chosen: a rectangular unit cell and a rhombic unit cell (Figure 4.2). It is obvious that in this mechanism of expansion along one side involving a contraction in the perpendicular direction will not particularly affect the axes (a_1 and b_1) in the rhombic cell (Figure 4.2, green); instead, a great variation will be recorded on the γ angle, which is not easy to interpret and also it will be less evident when only the crystallographic axes are considered. Therefore, the choice of a rectangular cell (Figure 4.2, purple) with all angles equal to 90° permits to easily observe the expansion along the axes (a_2 and b_2), enabling a better visualization and interpretation of thermal expansion mechanism.

It is clear that the choice of a new unit cell, different from the standard crystallographic one, can help to analyse the thermal phenomenon in many cases. The determination of a new unit cell can be performed by orthogonalizing the crystallographic axes in order to obtain new axes which are perpendicular to each other. This can be simple for some crystal systems but it becomes difficult for low symmetry systems like monoclinic and triclinic

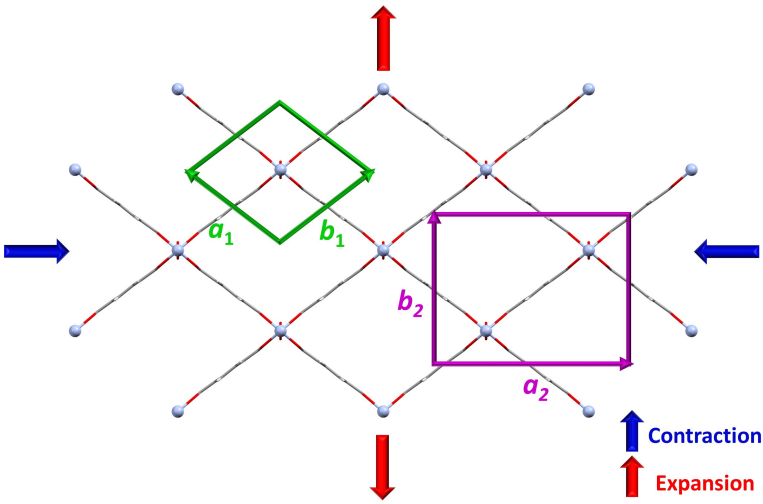

Figure 4.2. Schematic plot showing the effect of two different unit cells on the determination of the lattice expansion. The structural model was taken from literature [102]. Directions of contraction (blue) and expansion (red) are also given.

systems. In the projects that will be shown in this thesis, CTEs along the axes of the transformed unit cells were determined with PASCal, a program that is readily available online [103].

The program PASCal requires temperatures and lattice parameters for each temperature step as input and it gives as output the coordinates of the new axes, so-called principal axes ($\mathbf{X}_n$), the CTEs along the volume and the principal axes, and the expansivity indicatrix, which is a three-dimensional surface plot centred at the unit cell origin showing the variation of the magnitude of α along the direction (Figure 4.3). The expansivity indicatrix allows to visualizing the direction of the change in the unit cell as well as using color codes for highlight an expansion (red) or a contraction (blue).

The use of the free online program PASCal and the careful analysis of the crystal structure allowed to study and reveal the mechanism of the thermal expansion in the compounds that will be discussed in this chapter.

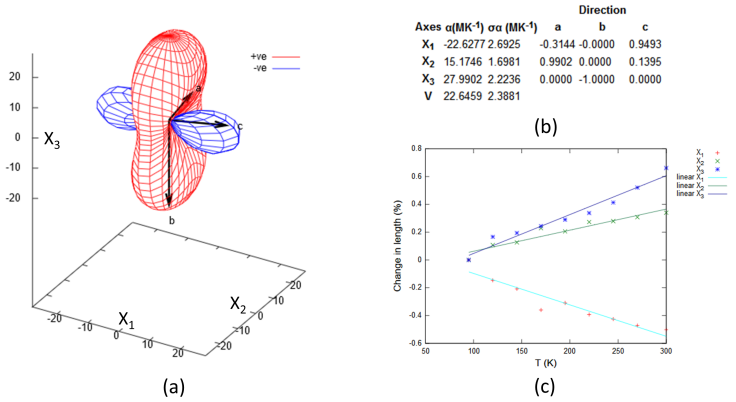

Figure 4.3. Outputs of the PASCal program: a) expansivity indicatrix, b) CTFs (σ) related to the principal axes (X_n) and volume, and c) plot of the change in lengths as function of the temperature.

4.2 Photosalient crystals

Three isotypical complexes, Cu(benzoate)L_2, (**1**) with L=4-stryryrilpyridine (4spy), (**2**) with 2'-fluoro-4-styrylpyridine (2F-4spy), and (**3**) with 3'-fluoro-4-styrylpyridine (3F-4spy), were investigated by temperature dependent *in situ* XRPD measurements. Sequential Pawley refinements revealed anisotropic thermal expansion with large volumetric expansion coefficients. A possible explanation for this peculiar thermal property was also given.

This study was done in collaboration with the research group of Prof. Jagadese J. Vittal from the National University of Singapore who provided the sample, characterized the crystal structures, and investigated the photosalient behaviour. The results were published in the journal *IUCrJ* (2020) [104].

4.2.1 Introduction

Photosalient crystals belong to the class of materials known as "dynamic molecular crystals". The peculiar property of these materials is to transform the strain energy accumulated by external *stimuli*, like heat, light, or pressure into mechanical work [105]. Indeed, when exposed to light (photosalient

effect, **PE**) or heat (thermosalient effect, **TE**), single crystals exhibit mechanical effects involving either change of shape (curling, bending, and twisting) [106, 107] or movements (jumping, flipping, and rotation) [108, 109]. As regards the photosalient behaviour, the mechanical motions are observed in single crystals where solid-state [2+2] cycloaddition reactions, [4 + 4] dimerization, isomerization, ring opening and closing reaction, polymorphic phase transition, and dynamic changes in the pseudorotaxane molecule can occur.

These compounds can also show anisotropic changes in lattice parameters, which accompany many of the salient effects [105, 107]. Indeed, after performing *in situ* measurements, the analysis of the lattice parameters variation revealed an anisotropic expansion and, in some compounds, very large coefficients of thermal expansion were recorded [30, 110].

In this work, the thermal behaviour of the three isotypical copper complexes **1**), **2**, and **3** was investigated (Figure 4.4). The crystal structures (mon-

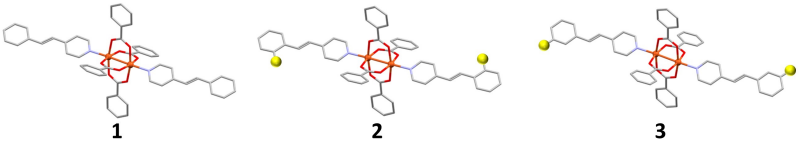

Figure 4.4. View of the three investigated isotypical compounds **1-3**. The figure highlights the peculiar paddlewheel-like structure of the complexes. Hydrogen atoms are omitted for clarity.

oclinic space group *C2/c* with *Z*=4) reveal distinct complexes, involving four benzoate ions and two 4-spy ligands, with a paddlewheel-like structure. The main difference in the three crystal structures is the presence and the position of the fluorine atom on the spy-related aryl group. Each pyridyl ligand interacts in a head-to-tail manner with one pyridyl from the neighbouring complex via $\pi \cdots \pi$ interactions forming a one dimensional chain-like motif (Figure 4.5). The distances between the centres of the C=C bonds are 3.787 Å in **1**, 3.765 Å in **2** and 3.810 Å in **3**, which make these compounds, according to Schmidt's rule, suitable for [2+2] cycloaddition reaction [111]. As a consequence, when exposed to UV light, these compounds show photosalient

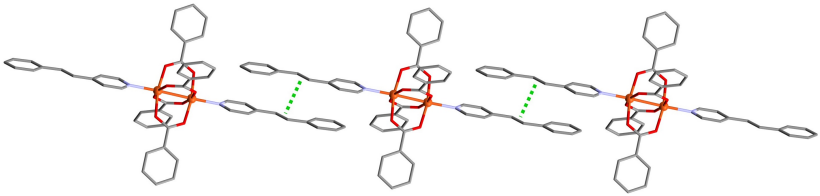

Figure 4.5. View of the one dimensional chain-like motif built up by $\pi\cdots\pi$ interactions. Hydrogen atoms are omitted for clarity.

behaviour. Furthermore, since these single crystals also move by rolling upon heating, temperature dependent *in situ* XRPD measurements were performed in order to study this phenomenon. The analysis of the lattice parameters as function of the temperature reveals very large anisotropic thermal expansion upon heating to about 200 °C.

4.2.2 Results and discussion

The thermal behaviour of compounds **1-3** was investigated by temperature dependent *in situ* XRPD measurements in the temperature range 30-200 °C. The inspection of the XRPD patterns revealed a large peak shifting, which is indicative of a remarkable thermal expansion (Figure 4.6). To study the

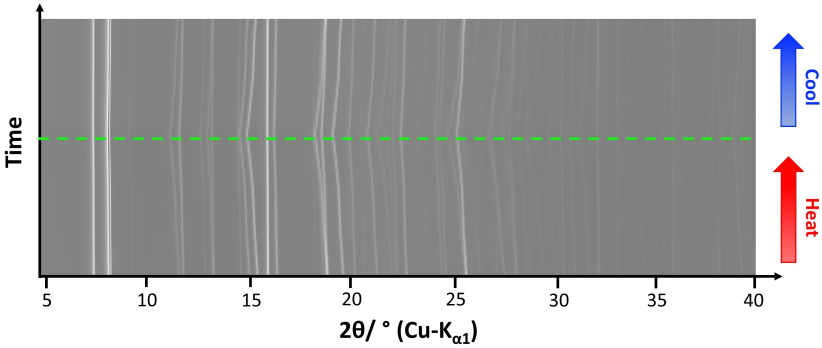

Figure 4.6. Two dimensional plot of the temperature dependent *in situ* XRPD measurement of compound **3**.

thermal expansion, sequential Pawley refinements were performed and the

lattice parameters were extracted. Since these compounds crystallize in the monoclinic space group $C2/c$, the program PASCal was used to calculate the thermal expansion coefficients along the three principal axes (Table 4.1). The principal X_1 axis is almost parallel to the directions [102] for **1** and **2**, and [101] for **3**. The principal X_2 axis is parallel to the *b*-axis in all three compounds and the principal X_3 axis is almost parallel to the directions $[\bar{1}02]$ for **1** and **3**, and $[10\bar{1}]$ for **2**. Table 4.1 shows that all compounds exhibit anisotropic thermal expansion with the biggest variation along the principal X_3 axis. Additionally, all solids exhibit relative small PTE except compound **3** that possesses a negative thermal expansion coefficient along the principal X_1 axis. The expansivity indicatrix for the three compounds also confirms the

Table 4.1. Thermal expansion coefficients of the volume and along the principal axes for compounds **1-3** extracted from PASCal.

1			Direction		
Axes	α, $10^{-6}K^{-1}$	σ_α, $10^{-6}K^{-1}$	*a*	*b*	*c*
X_1	13.9159	0.8233	0.5338	0.0000	0.8456
X_2	5.0233	1.0415	0.0000	1.0000	0.0000
X_3	166.3843	5.5537	0.5291	0.0000	0.8486
V	241.8234	6.4930			
2			Direction		
Axes	α, $10^{-6}K^{-1}$	σ_α, $10^{-6}K^{-1}$	*a*	*b*	*c*
X_1	21.8943	0.4764	-0.3870	0.0000	-0.9221
X_2	38.3804	0.5909	0.0000	-1.0000	0.0000
X_3	167.7776	5.2979	0.8072	-0.0000	-0.5902
V	233.1210	6.2627			
3			Direction		
Axes	α, $10^{-6}K^{-1}$	σ_α, $10^{-6}K^{-1}$	*a*	*b*	*c*
X_1	-13.8283	3.7014	0.6377	-0.0000	0.7703
X_2	64.5518	1.3444	0.0000	-1.0000	0.0000
X_3	228.3639	9.0008	-0.3302	0.0000	0.9439
V	285.6904	7.1723			

α is the CTE, σ_α is the error in the CTE, *a*, *b* and *c* are the projections of X_n on the unit cell axes.

anisotropic behaviour just as the plots of the volume and the variation of the axes as function of the temperature, which, in addition, show no hysteresis on cooling and the linearity of the expansion in the studied range (Figures 4.7,A.1,A.2).

The explanation of the mechanism behind the anisotropic thermal expan-

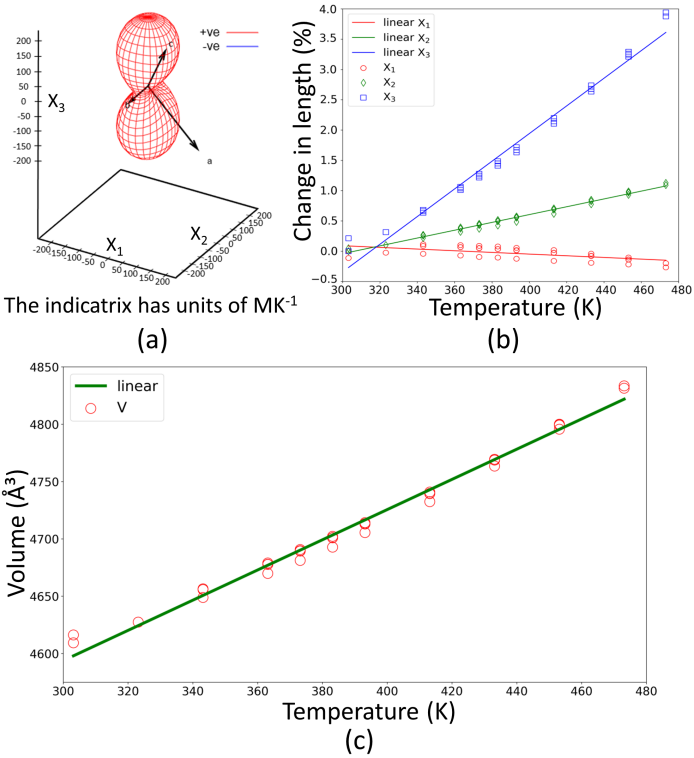

Figure 4.7. Results from analysing the thermal behaviour of **3** using PASCal : a) expansivity indicatrix (units: MK^{-1}), b) plot of the axes variations as function of temperature and c) plot of the volume expansion as function of temperature. Adapted from [104].

sion behaviour is revealed by investigating the structural motifs in compounds **1-3**. As stated before, the main structural motif is the one dimensional chain-like structure formed by the paddlewheel complexes connected by $\pi \cdots \pi$

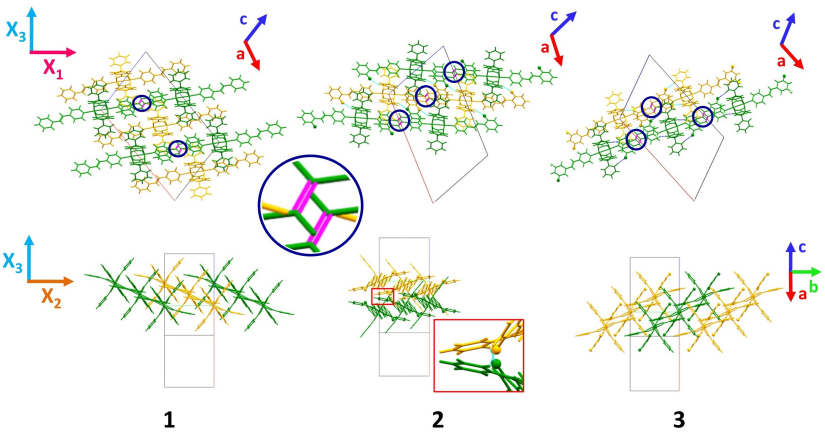

Figure 4.8. Representation of the projections of the crystal structures for compounds **1**-**3** along the crystallographic *b*-axis (above) and along the principal X_1 axis (below). Crystallographic (*a*, *b* and *c*) and principal (X_1, X_2 and X_3) axes are also given. The 1D chain-line structure motif formed by $\pi\cdots\pi$ interactions (blue circle) are depicted in green and yellow. F$\cdots$H-C interactions in compound **2** are highlighted in the red rectangle. Adapted from [104].

interactions between the C=C bonds of the styrylpyridine ligands and by the strong coordination bonds in the complex itself (Figure 4.8). This chain-like motif runs in the $[2\bar{2}1]$ direction, which is a combination of the principal X_1 and X_2 axes. Therefore, an expansion along these axes is inhibited by the rigidity of the chain. Although the $\pi\cdots\pi$ interactions are considered to be weak, their determinant role was confirmed by the observation of the photoreactivity of these compounds in the temperature range 120-200 °C. This result indicates that the Schmidt's criteria for a [2+2] cycloaddition reaction in these crystals is satisfied, which means that at high temperatures, the alignment of the styrylpyridine ligands is retained.

The inspection of table 4.1 for the three compounds reveals differences in magnitude and sign of the CTEs. Although the three compounds are isotypical, the differences such as the presence and the position of the fluorine atom on the styrylpyridine-related phenyl group, affect the expansion behaviour.

In compound **2**, the fluorine atoms are involved in intermolecular F···H-C interactions that connect neighbouring chains. These interactions inhibit the expansion along the principal X_2 axis and, as a result, the α_2 coefficient in **2** is the smallest of the three compounds. Compound **3** shows intramolecular F···H-C interactions between the styrylpyridine and the benzoate ligands that further strengthen the chain. This could explain the small contraction along the principal X_1 axis, which is associated with a negative value of α_1. The expansion along the principal X_3 axis is promoted by mechanics and the α_3 value along the principal X_3 axis is the largest one. Concerning **1**, this compound doesn't have any fluorine atom that can give rise to F···H-C interactions. Therefore, since the only effective interactions on the thermal expansion are the $\pi\cdots\pi$ interactions, the values of α_1, α_2, and α_3 are in the intermediate range of the investigated compounds.

The values of the thermal expansion coefficients were compared with those of organo-metallic complexes found in literature revealing a very high expansion (Tables 4.2, A.2). However, it should be highlighted that, when comparing values from literature, many factors should be considered like different expressions used for calculating thermal expansion and the non-linearity of the expansion.

Table 4.2. Comparison of thermal expansion coefficients of the volume and along the principal axes from this work with those in literature.

Metal complexes	**T range/ K**	**Axial TE, α_x/ $10^{-1}\cdot K^{-1}$**	**VTE, α_V/ $10^{-1}\cdot K^{-1}$**	**Ref.**
1	300-480	13.9, 56.0, 166.4	241.8	This work
2		21.9, 38.3, 167,8	233.1	
3		-13.8, 64.5, 228.4	285.7	
PHA	220-350	260.4, 39.4, -79.9	247.8 (α form)	[110]
	100-270	124.0, 105.4, 114.9	255.5 (β form)	
$Cu(acac)_2$	100-300	42, 44, 70	213.15	[112]
$(Himd)_2[CuCl_4]$	273-353	-38, 568, -184	346	[28]

All compounds in this table show linear expansion during heating.

4.2.3 Conclusions

The thermal behaviour of three isotypic copper complexes with formula Cu(benzoate)L_2 (with L=4spy, 2F-4spy, and 3F-4spy) was studied by temperature dependent *in situ* XRPD measurements. The inspection of the XRPD patterns showed big shifts in peak position, which are related to a large thermal expansion. Lattice parameters were extracted by sequential Pawley refinement, and subsequently used as input values for the program PASCal. The use of the program allowed to reveal the anisotropic thermal expansion with the biggest variation along the principal X_3 axis. The analysis of the structural motifs allowed to disclose the mechanism behind the anisotropic expansion where interactions like $\pi\cdots\pi$ and weak hydrogen bonds F$\cdots$H-C play an important role. In the end, the comparison of the values of the CTEs with those of the literature confirmed the giant anisotropic thermal expansion of the three studied compounds.

4.2.4 Experimental section

Samples

Synthesis and characterization of compounds **1**, **2**, and **3** were done by Dr. Khushboo Yadava (National University of Singapore) according to the publication [104].

Temperature dependent *in situ* X-ray powder diffraction

Temperature dependent *in situ* XRPD measurements were carried out on a Bruker D8-Advance diffractometer in Debye-Scherrer geometry with Cu-$K_{\alpha 1}$ radiation from a primary Ge(111)-Johansson-type monochromator and Våntec detector. The patterns for the thermal expansion analysis were collected in a 2θ range from 3° to 40° applying a total scan time of 2 hours per measurement. The temperature was adjusted using a water-cooled capillary heater (MRI) and the samples were heated following the thermal cycling program (30-200-70-200-30) °C in 20 °C steps (in ranges 30-90 °C and 120-200 °C) and in 10 °C steps (in the range 90-120 °C) with a heating ramp of 2

$K \cdot min^{-1}$. Before each measurement, a delay time of 10 minutes was applied to ensure thermal equilibration of the sample.
Pawley refinement was performed with the program TOPAS 6.0 [64].

4.3 Interpenetrated Metal-Organic Framework

The thermal behaviour of two isostructural interpenetrated MOFs, $M(pvb)_2 \cdot DMF$ (with M= Zn^{II}/Cu^{II} and pvb= *trans*-2-(4-pyridyl)-4-vinylbenzoate) was investigated by temperature dependent *in situ* XRPD measurements under *vacuum* condition. Sequential Rietveld refinements allowed to observe the phase transition from the Zn-bearing MOF (**1**) to the anhydrous form (**2**) and to reveal a very large positive and negative thermal expansion in the temperature range 30-150 °C.

This study was done in collaboration with the research group of Prof. Jagadese J. Vittal from the National University of Singapore who provided the samples, characterized the crystal structures and investigated the optical properties. The results were published in the journal *Angewandte Chemie* (2019) [113].

4.3.1 Introduction

MOFs are a class of porous polymeric materials formed by the coordination of organic bridging ligands (linkers) to metal ions (nodes) [114, 115]. These compounds show many applications in catalysis, separation, gas storage, and molecular recognition [116–119]. Contrary to porous inorganic materials such as zeolites, the possibility to use different organic linkers allows to potentially control the architecture and the functionalization of the pores and, as consequence, to have flexibility in designing new structures [120].

Interpenetration is one of the peculiar phenomena that can also be found in MOFs. It is observed in entangled structures where two or more independent infinite networks interpenetrate each other. This phenomenon takes inspiration from structures of compounds that the nature offers, such as the

entangled strands in the DNA double helix. However, contrary to the DNA, where the strands are held together by non-covalent bonds and no disruption is needed to disentangle them, in the interpenetrated MOFs, disentanglement is only possible when covalent bonds are broken [121, 122]. The degree of interpenetration, defined by the term '*n*-fold' (where *n* is the number of independent nets), can vary from two to twelve but exceptions are also possible [123]. Although MOFs are known to be very robust upon removal of the guest molecules, it was observed that the degree of interpenetration can be manipulated not only during the synthesis process [124, 125] but, surprisingly, in the solid state as well. A few examples related to the change of interpenetration in solid state can be found [126] and only some of them show this phenomenon occurring in a single-crystal-to-single-crystal manner (SCSC) [127, 128].

Non-centrosymmetric crystal structures can exhibit second-order nonlinear optical (NLO) properties, which make these materials eligible for applications in photonics, for example for optical signal transimission and processing [129]. Additionally, the use of chiral ligands may allow MOFs to be NLO active even though they do not ensure strong second harmonic generation (SHG) responses of the material. A strategy to obtain compounds with these properties is to design and synthesize structures with diamondoid network (**dia** net), which can be obtained by choosing metal atoms suitable for tetrahedrally coordinating specific rigid bridging ligands. This network is the most suitable geometry for obtaining these compounds as the lack of inversion centres promote the formation of non-centrosymmetric solids [130].

During the study of Zn^{II} and Cu^{II} MOFs, the research group of Prof. Vittal was able to successfully synthesize and characterize two zinc MOF, $Zn(pvb)_2 \cdot DMF$ (**1**) and its anhydrous form (**2**), and one copper MOF with formula $Cu(pvb)_2 \cdot DMF$ (**3**). Compound **1**, isomorphous to compound **3**, crystallizes in the non-centrosymmetric space group *Cc*. The zinc atoms have a five-coordinate geometry and they are bonded to two pyridyl-related N atoms and three carboxylate-related oxygen atoms. The structures reveals a diamandoid framework, which is 7-fold interpenetrated (**dia**) (Figure 4.9). Despite this

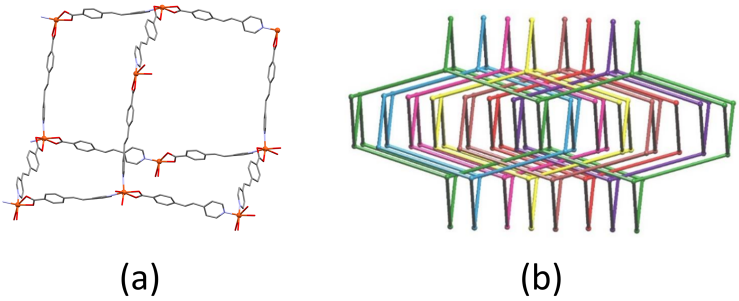

Figure 4.9. View of the **dia** net (a) and the 7-fold interpenetration (b) in compound **1**. Adapted from [113].

peculiarity, the compound exhibits voids filled with DMF molecules. Compound **2** crystallizes in the non-centrosymmetric space group *C2*. In this case, two distinct zinc atoms, one four-coordinated and the other six-coordinated, are bonded to four ligands giving rise to a diamandoid cage. This framework is 8-fold interpenetrated and, due to the dense packing, no voids are present (Figure 4.10).

Crystals of **1** and **2** were tested for possible interesting optical properties. Non-linear optical responses of **1** and **2** were analysed by mapping SHG and 2PPL responses of the single crystals. The results display that at the optimum excitation wavelength of 950 nm, the SHG response at 475 nm from the

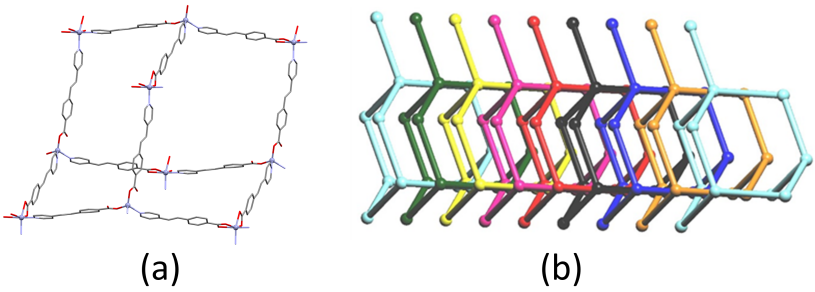

Figure 4.10. View of the **dia** net (a) and the 8-fold interpenetration (b) in compound **2**. Adapted from [113].

crystal **2** is circa 125 times larger that that of **1** whereas the 2PPL intensity of sample **2**, at the optimum excitation wavelength of 680 nm, is circa 14 times stronger than that of sample **1**.

In this project, the two interpenetrated MOFs, compounds **1** and **3**, were investigated by temperature dependent *in situ* XRPD measurements and their interesting thermal behaviour as well as the relationship between the solvated (**1**) and the anhydrous (**2**) form were revealed.

4.3.2 Results and discussion

The thermal behaviour of compound **1** was initially investigated by thermogravimetric analysis in the temperature range 30-650 °C. The TG curve reveals at around 120 °C a weight loss of 12.7 wt-% corresponding to the loss of one molecule of DMF (Δm_{calc}= 12.5 wt-%, Figure 4.11). This feature is attributed to the removal of the DMF with possible transition to the anhydrous phase, which involves a switch of the degree of interpenetration, rarely

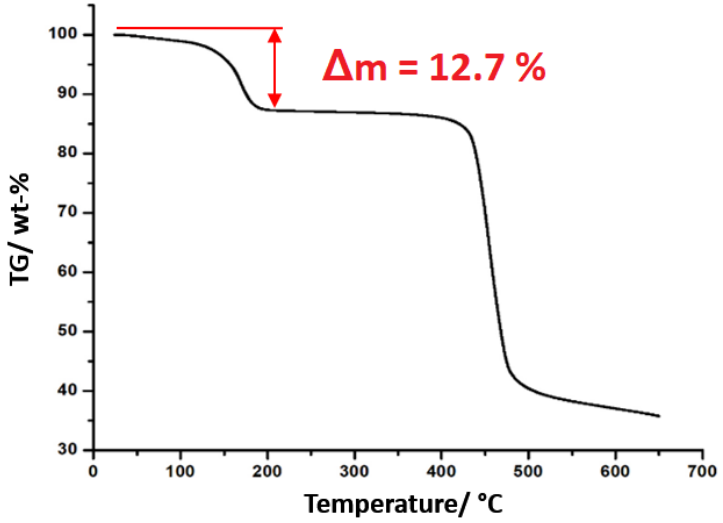

Figure 4.11. TG curve of compound **1** measured in dynamic nitrogen atmosphere.

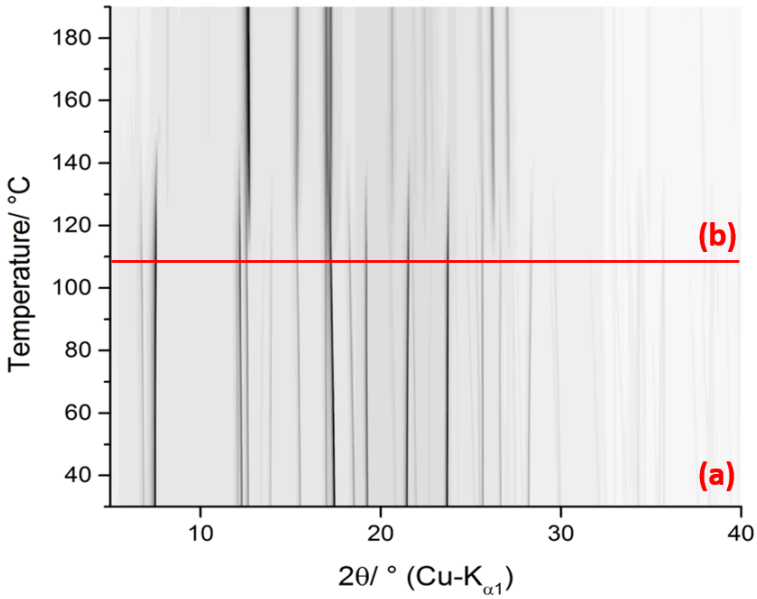

Figure 4.12. Temperature dependent *in situ* XRPD measurement showing the transition from compound **1** (a) to compound **2** starting at circa 110 °C (b). Adapted from [113].

observed in literature.

Temperature dependent *in situ* XRPD measurements were performed in order to elucidate the thermal behaviour of compound **1** observed in the TG-curve. The compound was investigated in the temperature range 30 °C-190 °C under *vacuum* condition to easily remove the guest DMF molecules from the framework. The experiment confirmed the transition to the anhydrous compound **2** starting at circa 110 °C and ending at 160 °C with no other intermediate forms (Figure 4.12). In contrast to the structure obtained from SC-XRD at -100 °C [113], Rietveld refinement of the high temperature structure of compound **2** shows the β angle close to 90° (β= 94.2° at -100 °C), which is retained at 30 °C (Figure 4.20, Table 4.4). This peculiarity of compound **2** was further observed by performing an additional temperature dependent *in situ* XRPD measurement of a mixture of compounds **1** and **2** in the tempera-

ture range 30-430 °C (Figures 4.13).

A possible mechanism of the transition from the solvated to the anhydrous form can be derived from the analysis of the structural motifs. Upon heating, the DMF molecules are removed from the 1D channels parallel to the *c*-axis. In order to fill the voids, alternating **dia** components from adjacent structures move towards each other by shrinking the whole crystal structure, which explains the decrease in the cell volume by 312.4 $Å^3$. The proxim-

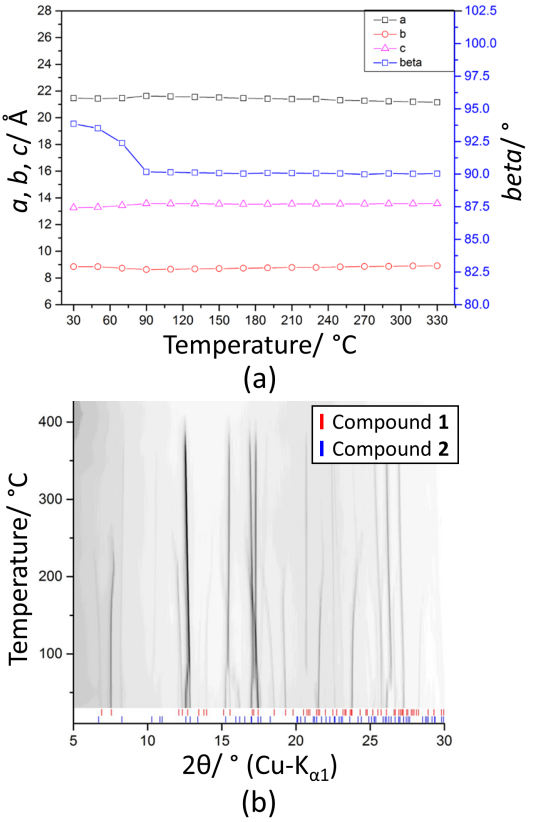

Figure 4.13. Lattice parameters trend as function of the temperature derived from sequential Pawley refinement (a) and temperature dependent *in situ* XRPD measurements of a mixture of compounds **1** and **2** (b). Adapted from [113].

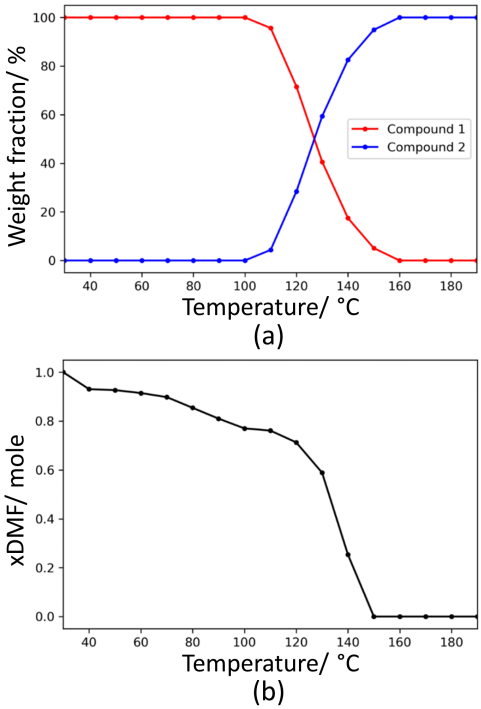

Figure 4.14. Plots of weight fractions of compounds **1** and **2** (a) and DMF content (b) as function of the temperature derived from sequential Rietveld refinements. Adapted from [113].

ity of different frameworks promotes the breakage and subsequent formation of the Zn-ligand bonds, which is accompanied by a change in the coordination sphere of the zinc atoms (distorted trigonal bipyramidal to mixture of octahedral and tetrahedral geometries). As a consequence, the degree of interpenetration is increased from 7-fold to 8-fold.

The phase transition and the release of DMF as function of the temperature was monitored through sequential Rietveld refinements of both structures via the XRPD patterns of the *in situ* experiment under *vacuum* condition (Figure 4.14). In addition, lattice parameters of the solvated form were extracted in order to monitor the thermal expansion. Since compound **1** crystallizes in

Table 4.3. Thermal expansion coefficients of the volume and along the principal axes for compounds **1** extracted from the analysis using PASCal.

1			Direction		
Axes	α, $10^{-6}K^{-1}$	σ_α, $10^{-6}K^{-1}$	*a*	*b*	*c*
X_1	-199.5967	24.5302	-0.8393	0.0000	-0.5436
X_2	88.8589	16.7810	-0.1614	-0.0000	0.9869
X_3	225.0249	4.4317	0.0000	-1.0000	0.0000
V	111.9961	4.8511			

α is the CTE, σ_α is the error in the CTE, *a*, *b* and *c* are the projections of X_n on the unit cell axes.

a monoclinic space group, PASCal software was used to calculated the thermal expansion coefficients along the three orthogonal principal axes. The inspection of the CTEs (Table 4.3) reveals large anisotropic thermal expansion with PTE along the principal X_3 axis (α_3=225.0249 x $10^{-6}K^{-1}$, parallel to the crystallographic *b*-axis), relatively small PTE along the principal X_2 axis (α_2=88.8589 x $10^{-6}K^{-1}$, almost parallel to the *c*-axis) and high NTE along the principal X_1 axis (α_1=-199.5967 x $10^{-6}K^{-1}$, nearly parallel to the crystallographic [201] direction with the *a*-axis as the most influential component axis). All expansions are rather linear in the measured temperature range (Figures 4.15).

The understanding of the mechanism behind the anisotropic thermal expansion of compound **1** is quite important in the process of finding a possible application as well as for the rational design of new compounds. For this reason, the crystal structure of compound **1**, obtained by Rietveld refinement (Figure 4.19) was carefully analysed and structural motifs identified. The key to understand the mechanism is to focus on the base of the **dia** net, which can be approximated to a rectangle containing six zinc atoms (Figures 4.16 and A.3). The long side includes two ligands bridging three zinc atoms and it runs along the $[20\bar{1}]$ direction. The short side includes one ligand, bridging two zinc atoms and it runs along the $[11\bar{2}]$ direction. An expansion along both directions is inhibited since it requires the stretching of the ligands. However, the long side does not form a rigid unit but it may bend due to the possibility

of a change in angle between the two ligands (black double arrows in Figure 4.16). The variation of the angle leads to a distortion of the rectangular motif along *b*- and *c*-axes (principal X_3- and X_2- axes, respectively). In addition, since the framework is packed along the *c*-axis, parallel to the direction of the channels filled with DMF molecules, a possible movement of the **dia** fragments along the direction of the channels is hindered whereas it is promoted towards the channels (*ab* plane). Therefore, the preferred direction of the expansion is along the *b*-axis. As a consequence, just like in Nuremberg scissors, a compression along the principal X_1-axis is promoted by mechanics.

From a comparison of the reported thermal expansion coefficients in literature and the herein discussed study (Table A.2), it is apparent that **1** exhibits

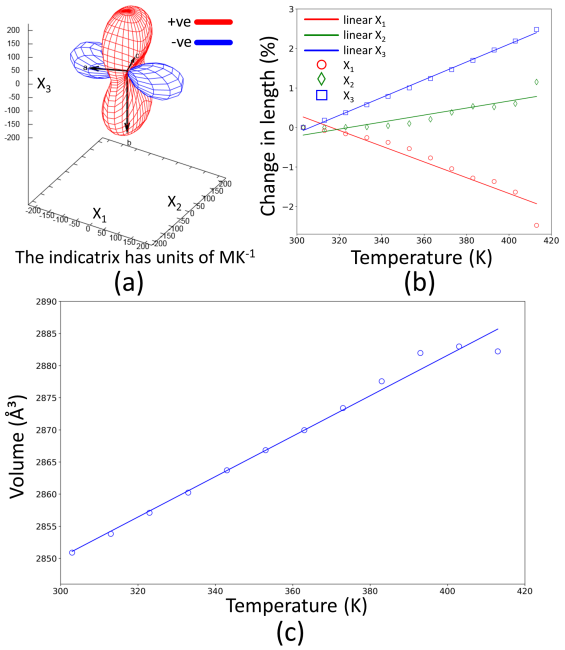

Figure 4.15. Results from PASCal program for compound **1**: a) expansivity indicatrix (units: MK^{-1}), b) plot of the axes variations as function of the temperature and c) plot of the volume expansion as function of the temperature. Adapted from [113].

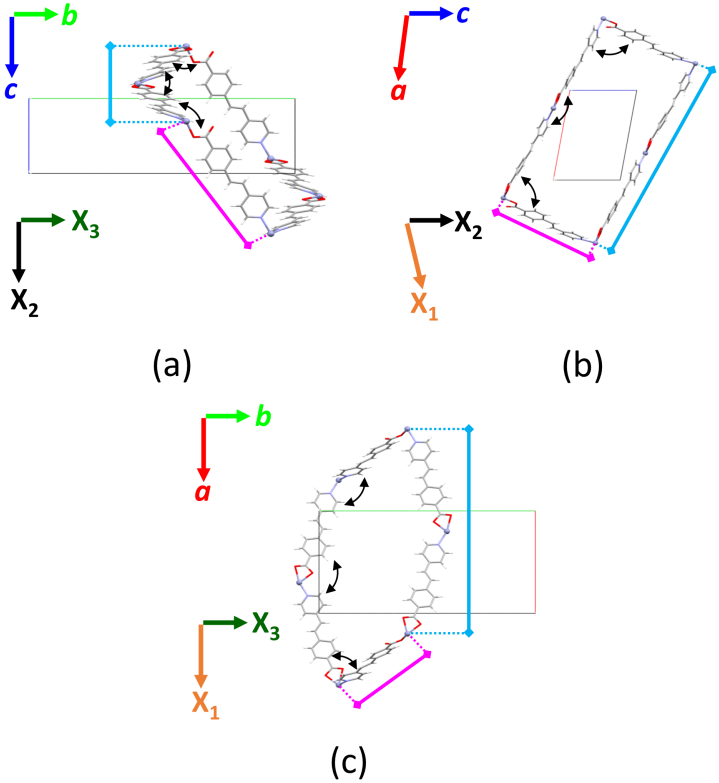

Figure 4.16. Representation of the rectangular motif of **dia** net in **1** along (a) *a*-axis, (b) *b*-axis and (c) *c*-axis. The long side is indicated by the light blue line, the short side by purple and the angle formed by zinc nodes by black double arrows. The principal and crystallographic axes are also given. Adapted from [113].

a large and significant anisotropic thermal expansion.

The thermal behaviour of compound **3**, isomorphous to compound **1**, was investigated by temperature dependent *in situ* XRPD measurements (Figure 4.17). Contrary to the zinc-based MOF, this compound did not show any phase transition upon heating. However, through sequential Rietveld refinements, it was possible to monitor the content of DMF as function of the tem-

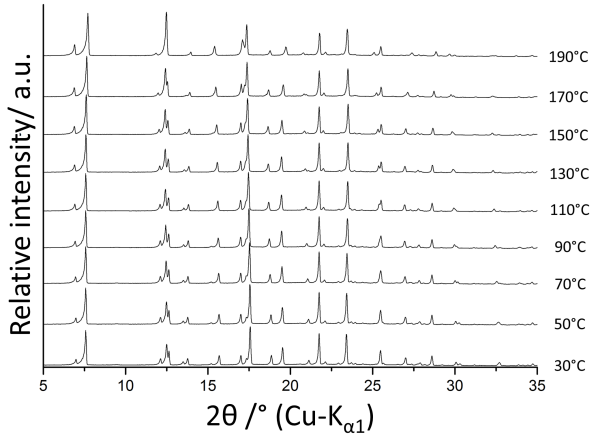

Figure 4.17. Selected XRPD patterns of **3** at different temperatures showing that there is no drastic structural change visible upon DMF removal by heating. Adapted from [113].

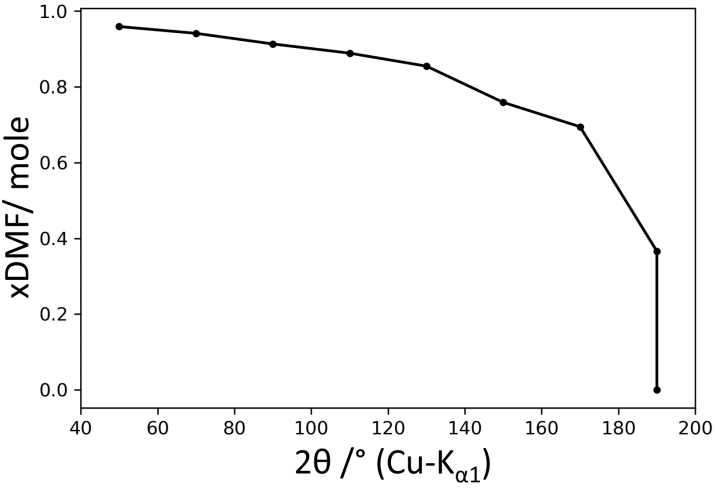

Figure 4.18. Evolution of the content of DMF molecules in compound **3** during temperature dependent *in situ* XRPD measurements as a function of temperature. Adapted from [113].

perature and to observe the complete release of the guest molecules at 190 °C (Figures 4.18).

4.3.3 Conclusions

The thermal behaviour of two interpenetrated MOFs, ZnMOF·DMF (**1**) and CuMOF· DMF (**3**), was investigated by temperature dependent *in situ* XRPD measurements.

Contrary to compound **3**, where no transition was observed, compound **1** exhibits in *vacuum* a phase transition to the anhydrous form **2** associated with a change in the degree of interpenetration. This interesting phenomenon is rare in the solid state and only a few examples have been reported in literature so far. Interestingly, this transition is accompanied by a giant enhancement of the SHG (circa 125 times) and 2PPL (circa 14 times), which makes this compound eligible for a possible application as NLO devices. In addition, a remarkable anisotropic thermal expansion was observed in **1** through sequential Rietveld refinement, for which a possible mechanism was proposed.

4.3.4 Experimental section

Samples

Synthesis and samples characterization of compounds **1**, **2**, and **3** were mainly done by Dr. Zhihui Chen (National University of Singapore) according to the publication [113].

Temperature dependent *in situ* X-ray powder diffraction

XRPD and variable temperature *in situ* XRPD measurements of **1** were carried out on two laboratory powder diffractometers in Debye-Scherrer geometry: Stadi P-Diffractometer (Stoe), Cu-$K_{\alpha 1}$ radiation from primary Ge(111)-Johann-type monochromator, array of 3 Mythen 1 K detectors (Dectris) and Bruker D8-Advance, Cu-$K_{\alpha 1}$ radiation from primary Ge(111)-Johannson-type monochromator, Våntec detector. For measurements on both diffractometers, the samples were loaded into 0.5 mm diameter quartz capillaries

Table 4.4. Crystallographic and Rietveld refinement of compounds **1**, **2** and **3**.

Compound	**1**	**2**	**3**
Crystal system	Monoclinic	Monoclinic	Monoclinic
Space group (No.)	*Cc* (9)	*C*2 (5)	*Cc* (9)
Wavelength/ Å	1.5406	1.5406	1.5406
a/ Å	13.3862(2)	21.777(2)	13.2309(3)
b/ Å	25.6147(6)	8.5362(6)	25.1532(6)
c/ Å	8.4313(3)	3.620(2)	8.4936(2)
β/ °	99.550(2)	90.34(1)	98.603(3)
V/ Å^3	2850.9(1)	2532.2(3)	2794.9(1)
Z	4	4	4
T/ K	303	303	303
Refined parameters	54	46	58
D_{calc}/ g·cm^{-3}	1.35	1.35	1.39
R_{wp}/ % [a]	3.82	4.18	5.46
R_p/ % [a]	3.16	3.40	4.17
R_{Bragg}/ % [a]	1.12	0.91	1.86
Starting angle measured/° 2θ	0	0	0
Final angle measured/° 2θ	110	110	110
Starting angle used/° 2θ	5	5	5
Final angle used/° 2θ	60	60	60
Step width/° 2θ	0.01	0.01	0.01
Time/ h	2	2	2

[a] As defined in section 2.2.3.

(WJM-Glas/Mueller GmbH), which were spun during the measurements. For the measurements on the Stoe diffractometers, powder patterns were measured in a 2θ range from 2.0° to 110.0° applying a total scan time of 2 hours per measurement. The temperature was adjusted using an Oxford Cryostream 500 device (Oxford Cryosystems). The sample was heated from 30 °C to 190 °C and back to 30 °C in steps of 10 °C. During each step a diffraction pattern

was collected after a delay time of 30 minutes to ensure thermal equilibration of the sample. The experiment was carried out with a capillary microreactor (designed in-house), connected to a pumping station (T-Station 75 Turbo-molecular), which allowed the sample to be heated under *vacuum* condition (Figure 2.6, e-f). For the measurements on the Bruker diffractometer, the powder patterns were measured in a 2θ range from 2.0° to 40.0° applying a total scan time of 2 hours per measurement and the temperature was adjusted using the TC-transmission furnace (MRI capillary heater). The sample was heated from 30 °C to 430 °C in steps of 20 K. During each step a diffraction pattern was collected after a delay time of 5 minutes to ensure thermal equilibration of the sample. XRPD patterns and variable temperature *in situ* XRPD measurements of **3** were recorded on the laboratory powder diffractometer in Debye-Scherrer geometry: Stadi P-Diffractometer (Stoe), Cu-$K_{\alpha 1}$ radiation from primary Ge(111)-Johann-type monochromator, array of 3 Mythen 1 K detectors (Dectris). The sample was loaded into a 0.5 mm diameter borosilicate capillary (WJM-Glas/Mueller GmbH), which was spun during the measurements. The patterns were measured in a 2θ range from 2.0° to 110.0° applying a total scan time of 2 hours per measurement and the temperature was adjusted using an Oxford Cryostream 500 device (Oxford Cryosystems). Pawley and Rietveld refinements were performed with the program TOPAS 6.0 [64].

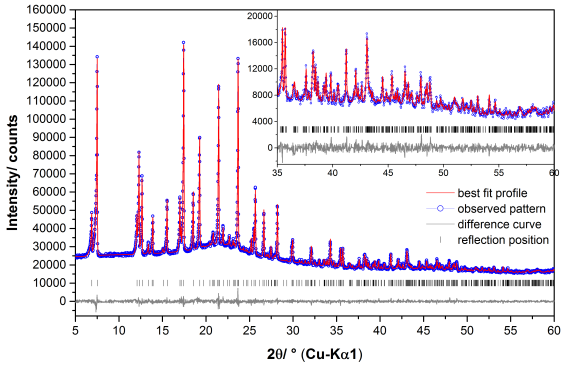

Figure 4.19. Scattered X-ray intensities of compound **1** during *in situ* experiment at 30 °C under vacuum conditions as a function of diffraction angle 2θ. The observed pattern (circles) measured in Debye-Scherrer geometry, the best Rietveld fit profiles (line) and the difference curve between the observed and the calculated profiles (below) are shown. The high angle part starting at 35° in 2θ is enlarged for clarity.

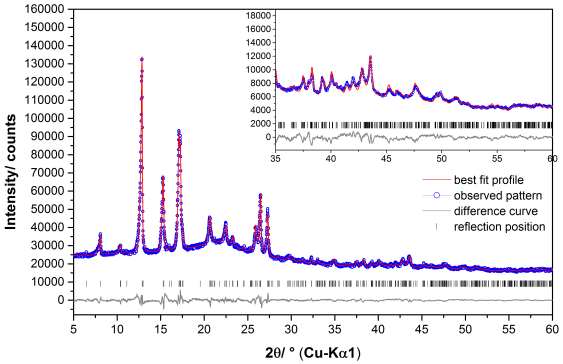

Figure 4.20. Scattered X-ray intensities of compound **2** after *in situ* experiment at 30 °C under vacuum conditions as a function of diffraction angle 2θ. The observed pattern (circles) measured in Debye-Scherrer geometry, the best Rietveld fit profiles (line) and the difference curve between the observed and the calculated profiles (below) are shown. The high angle part starting at 35° in 2θ is enlarged for clarity.

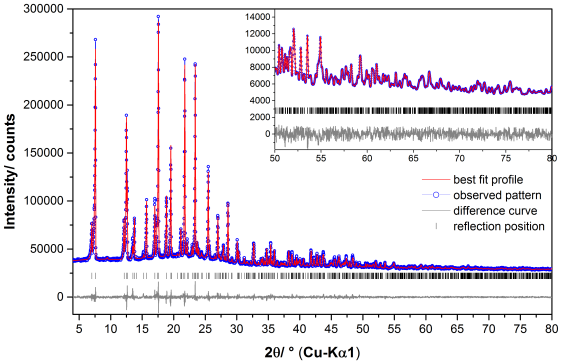

Figure 4.21. Scattered X-ray intensities of compound **3** during *in situ* experiment at 30 °C as a function of diffraction angle 2θ. The observed pattern (circles) measured in Debye-Scherrer geometry, the best Rietveld fit profiles (line) and the difference curve between the observed and the calculated profiles (below) are shown. The high angle part starting at 50° in 2θ is enlarged for clarity.

5 Investigation of ultrafast synthesis of zeolites

This chapter is dedicated to the study of two ultrafast synthetic processes of Chabazite zeolite designed at BASF SE in Ludwigshafen am Rhein (Germany). In particular, the first process, which is based on a solvent-free approach, was investigated through SEM (coupled with BSE and EDX) and XRPD measurements using both laboratory and synchrotron light sources. By using the synchrotron data collected at the beamline P02.1 in PETRA III (DESY, Hamburg, Germany), the same process was analysed with two different approaches: the reciprocal space approach, using the "standard" XRPD analysis and the real space approach, using PDF analysis. The second process is a solvent-based approach and it was studied by SEM and laboratory *in situ* XRPD measurements. Isothermal solid state kinetic studies for both processes are herein proposed as well.

5.1 Introduction

Zeolites are crystalline, microporous aluminosilicates. The term *zeolite* derives from the Greek *zéō* and *líthos* (boiling stone) and it was coined in 1756 by the swedish mineralogist Alex Friedrik Cronstedt, who observed a large amount of steam coming from this material during heating [131].

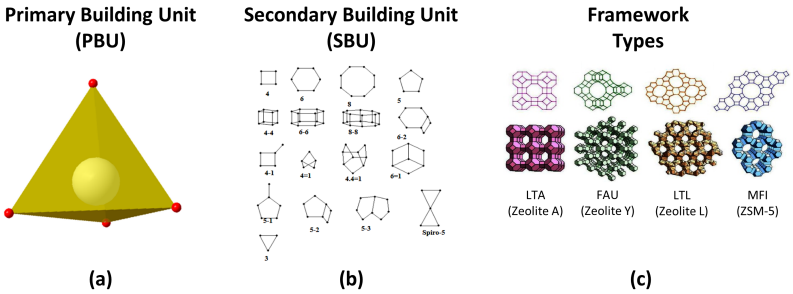

Figure 5.1. Representation of the primary building unit (a), the secondary building unit (b) and the framework types (c) in zeolites. Adapted from [132].

The crystal structure of a zeolite is composed by a three-dimensional network of $[AlO_4]^{5-}$ and $[SiO_4]^{4-}$ tetrahedra (the primary building unit, PBU) linked to each other by sharing all the oxygen atoms (Figure 5.1, a). Several tetrahedra arrange to form characteristic geometries (the secondary building unit, SBU), which in turn assemble to form a three-dimentional framework, denoted by three letters (Figure 5.1, b-c). The substitution of silicon with aluminium atoms creates a charge imbalance, which requires metal ions, such as those from the first or second main group, to be present in the cavities together with water molecules.

The presence of pores and channels in the crystal structure, as well as their dimensions and geometries, have a large impact on the properties and applications of these solids. Indeed, zeolites are used as molecular sieves [133], ion-exchangers, heterogeneous catalysts, feed additive [134], conductive films [135], and they are widely employed in many sectors of industry, agriculture, medicine, chemical technology, environmental protection, and engineering [136]. In 2016, the market size for zeolites was 5 million metric tons, of which about 40% related to synthetic zeolites [137].

Zeolites occur in nature and they can mostly be found in sedimentary and volcanoclastic deposits [138]. Naturally occurring zeolites are rarely pure and are contaminated to varying degrees by other minerals, metals, or other zeolites. Since industries require uniform, phase pure materials for many ap-

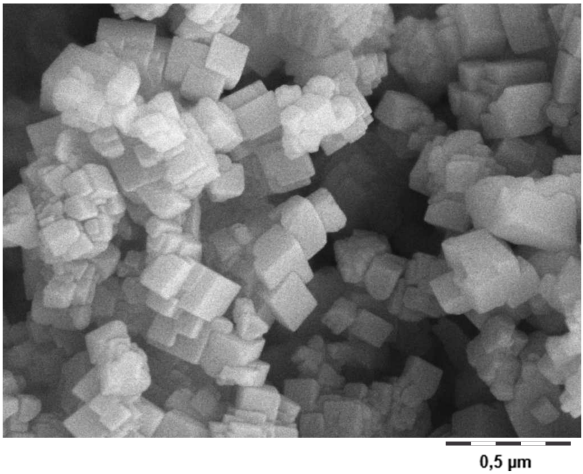

Figure 5.2. SEM image of Chabazite crystal morphology.

plications, and many commercially important products, such as zeolites A, X, and Y, are not present in nature, these porous solids are synthetically produced.

Zeolites can be synthesized in different ways, all of which have in common the presence of a silicon/aluminium oxide source. Crystalline seeds of the final product, alkalis or template agents may also be present in the synthetic procedure. The most common method is hydrothermal synthesis, which simulates the formation process occurred in nature millions of years ago. It consists of heating an alkaline aqueous solution with a source of silicon and aluminium, and a template agent (usually, quaternary ammonium salts) to a temperature above 100 °C on autoclave [139]. This process usually lasts from several hours to days until the final crystalline product is obtained. Since this is a time- and energy-consuming process with relevant consequences in the production costs, many strategies have been developed in the past decades to shorten the synthesis time. Microwave-assisted, ultrasound-assisted, and dry gel conversion syntheses are some of the strategies designed for this purpose. However, these processes still require several hours until the final product is obtained, and the drawback of short crystallization time is the low crys-

tallinity of the target material [140]. The Ultrafast synthesis process overcomes these aspects by shortening the reaction time and increasing the crystallinity of the final product [141].

In this project, two different ultrafast synthesis processes of a zeolite were mainly investigated by isothermal *in situ* X-ray powder diffraction. The target product is Chabazite, which crystallizes in the trigonal space group $R\bar{3}m$. This crystal symmetry reflects on the morphology of the solid showing characteristic pseudo cubic (rhombohedral shaped) crystals (Figure 5.2). Chabazite crystals are industrially important for their catalytic abilities in helping to remove the majority of harmful nitrogen oxides from diesel engine exhaust gases through selective catalytic reduction (SCR) [142]. To elucidate the synthesis process of both approaches, have a clear understanding of the reaction processes and of the energy/kinetics for the designed reactions, freshly prepared solutions were analysed using XRPD. This study contributes to obtain information necessary to transfer the whole process to the plant level.

5.2 Results and discussion

The synthetic process of a zeolite requires the precursors being heated in an autoclave, where a high pressure (more than 12 bars) is generated. In order to investigate this process *in situ*, a sample holder that withstands high pressure and with a hermetic seal must be chosen. Ordinary glass capillaries cannot be used as sample holders because they are easily burst. In order to overcome this problem, quartz capillaries were used to collect *in situ* XRPD data while the reaction occurred at high temperatures. Quartz capillaries withstand pressure at least up to 12/14 bars and were sealed with an oxyhydrogen torch and epoxy bi-component glue (Figure 5.3). For the solvent-free approach, quartz wool was also used to hinder the shifting of the reaction mixture in the capillary caused by the heating process and pressure development.

Figure 5.3. Sealed capillary used for *in situ* synchrotron measurements.

5.2.1 Solvent-free approach

The synthesis of Chabazite with the solvent-free approach was monitored through *in situ* experiments using the synchrotron light source PETRA III (DESY, Germany). Time-dependent *in situ* data at 190 °C were first analyzed in reciprocal space ('standard' XRPD, Figure 5.4). The comparison of the XRPD pattern of the mixture prior to heating, at room temperature (RT), with those of the single precursors (experimental) and sodium sulfate (calculated) revealed the presence of crystalline sodium sulfate forming from the reaction between aluminium sulfate and sodium silicate (Figure 5.5,a). The comparison of the mixture right before the end of the thermal treatment at 190 °C showed the formation of Chabazite and the retention of the sodium sulfate phase (Figure 5.5,b). The presence of Chabazite, with the characteristic cu-

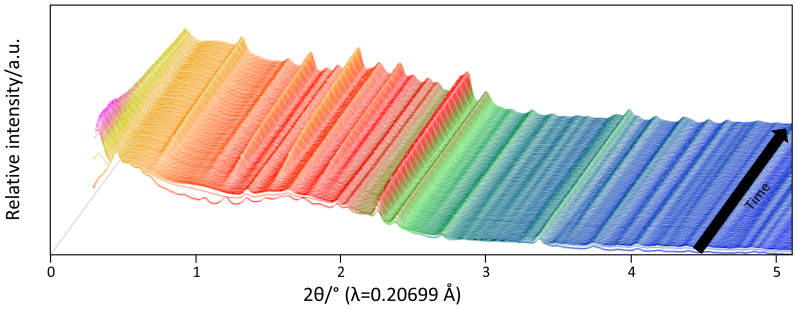

Figure 5.4. Time-dependent *in situ* synchrotron XRPD measurements showing the formation of Chabazite.

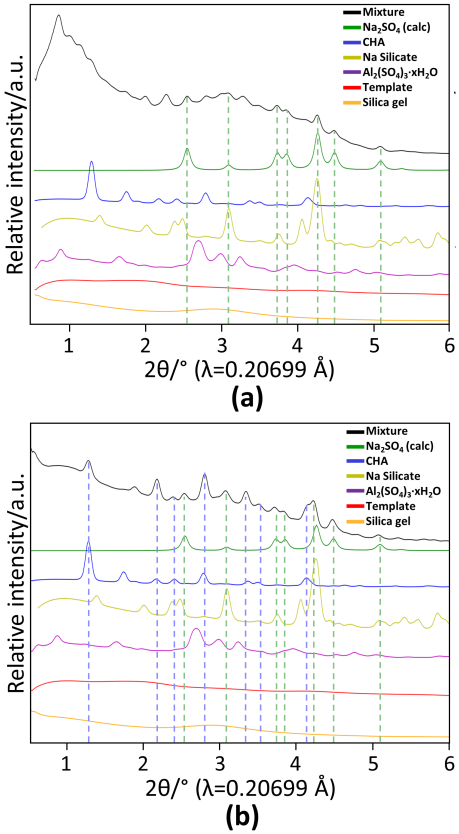

Figure 5.5. Comparison of the XRPD patterns of the final mixture at RT (a) and at the end of the heat treatment at 190 °C (B) with the precursors, and sodium sulfate. The presence of sodium sulfate and the Chabazite is highlighted with dashed lines in green and blue, respectively.

bic morphology, was also observed by SEM while crystals of sodium sulfate were confirmed by SEM-EDX (Figure 5.6).

Since the spatial resolution of the synchrotron XRPD patterns was not high enough to extract structural data through Rietveld refinement (these patterns were initally collected for generating PDF data), the final mixture was re-measured using a laboratory XRPD diffractometer (Figure 5.7). The Ri-

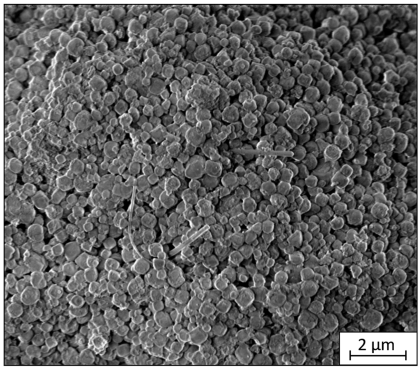

Spectrum label	Spectrum 5/ Atomic %	Spectrum 6/ Atomic %	Spectrum 7/ Atomic %
Na	1.99	18.60	18.05
S	3.35	9.42	9.57

Figure 5.6. SEM image of the cubic morphology of Chabazite (a) and SEM/BSE image of sodium sulfate (brighter crystals) along with the EDX results confirming the presence of sulfate (red rectangle, b).

etveld refinement, using Topas software, confirmed the presence of sodium sulfate and Chabazite in the final mixture after the thermal treatment and allowed to extract structural information about the Chabazite phase. The refined structure of Chabazite, compared to the refined one from the seeds, showed a

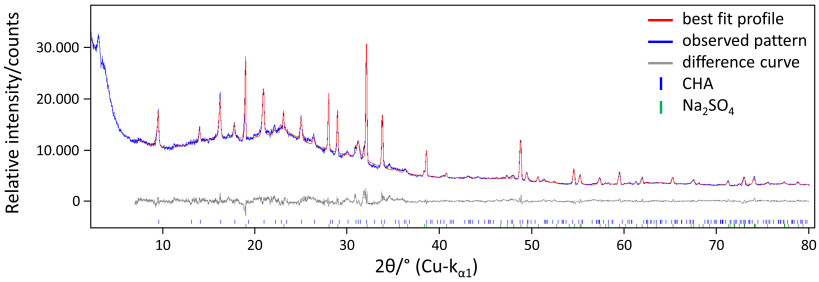

Figure 5.7. Scattered X-ray intensities of the solvent-free reaction mixture after the time-dependent *in situ* experiment at 190 °C as function of diffraction angle 2θ. The observed pattern (blue) measured in Debye-Scherrer geometry, the best Rietveld fit profile (red) and the difference curve between the observed and the calculated profiles (below) are shown. The presence of Chabazite and sodium sulfate is showed by their calculated reflections, represented by blue and green sticks, respectively.

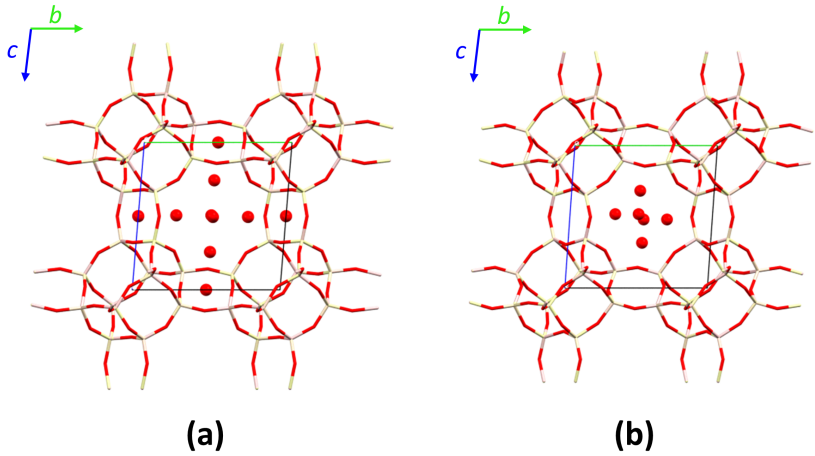

Figure 5.8. Projections of the crystal structure of Chabazite from the industrial seeds (a) and from the heat treatment at 190 °C (b) along the *a*-axis.

different content in the channels. After the heat treatment and storage at RT, structure refinement resulted in a model with an equivalent of 6 oxygen atoms per unit cell versus the 3.6 oxygen atoms per unit cell in the structure model obtained from fitting the XRPD pattern of the seeds (Figure 5.8). Sequential fitting of the (111) peak for sodium sulfate and $(01\overline{2})$ peak for Chabazite was performed in order to extrapolate the integrated area and the peak width. The $(01\overline{2})$ peak for Chabazite was chosen because it is the least affected by the presence of molecules in the pores. The integrated area gives information about the relative amount of the compound in the crystalline state whereas the peak width gives information about the crystallite size. Since no information from a standard was used, a trend of the crystallite size and not the actual value is given. The plot of the relative crystallite size of sodium sulfate and Chabazite versus reaction time (Figure 5.9,a) showed a fast growth in the first 50-60 minutes of the experiment followed by a plateau. The plot of the normalized integrated area of the (111) peak for sodium sulfate and $(01\overline{2})$ peak for Chabazite versus time revealed a sigmoidal trend for the Chabazite phase and negligible further formation of sodium sulfate (Figure 5.9,b).

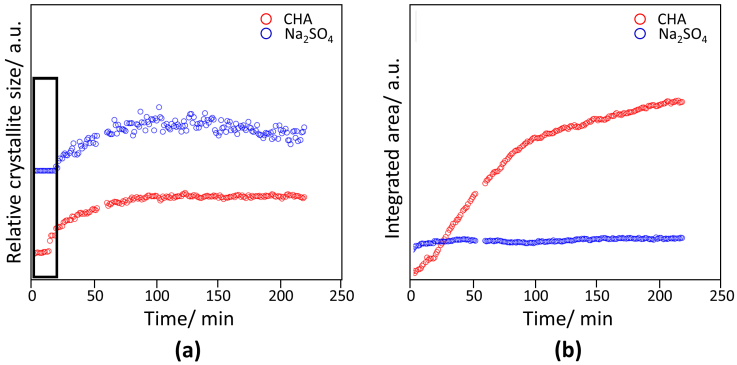

Figure 5.9. Plots of (a) relative crystallite size of Chabazite (red circles) and sodium sulfate (blue circles) versus time and (b) normalized integrated area of Chabazite (red circles) and sodium sulfate (blue circles) versus time. Due to the low intensity/background ratio, the crystallite size values at the beginning of the reaction are not reliable (black rectangle).

PDF patterns of the precursors and the target mixture were generated from the same data collected at Petra III in order to confirm the results previously obtained and extract further information about the short range order. By

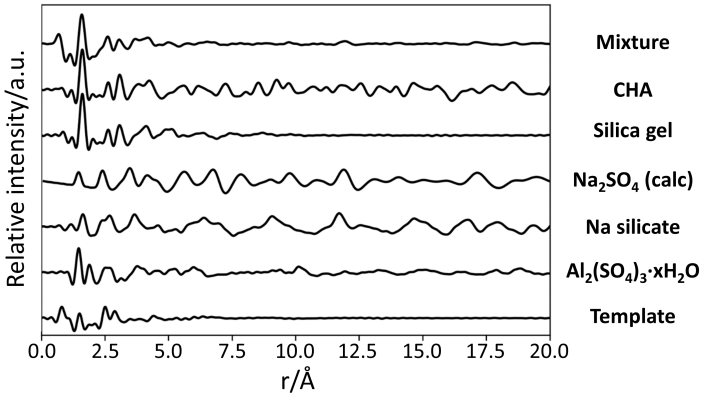

Figure 5.10. Stacking plot showing the experimental PDF patterns of the target mixture (before thermal treatment) and the precursors, and the calculated PDF pattern of sodium sulfate.

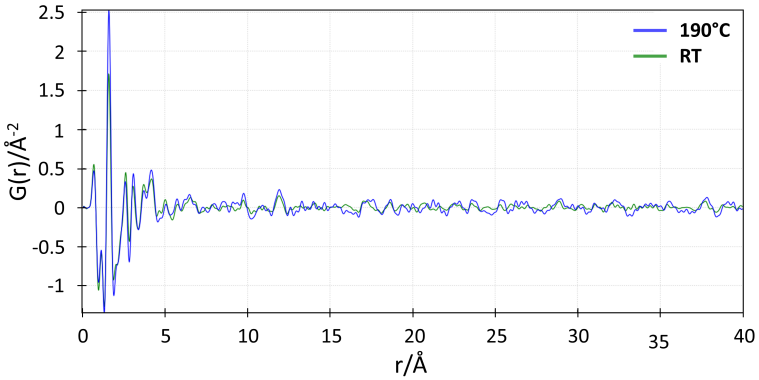

Figure 5.11. Superimposed PDF plots of the mixture at RT (before thermal treatment, green) and at 190 °C, right before the end of the thermal treatment (blue).

observing the short range signals of the PDFs (1-4.5 Å), it can be seen that the local structure signals of the final mixtures are primarily dominated by Chabazite seeds and, in part, silica gel (Figure 5.10). PDF plots of the solvent-free reaction mixture at RT, before the thermal treatment, and at 190 °C, right before the end of the treatment, are superimposed showing the increase in the signal intensity at medium/long range distances (10-40 Å), which means that large crystalline domains formed due to the heating process (Figure 5.11).

A sequential fitting of the first five peaks in the PDFs was performed in order to reveal possible changes in the local structure of the target mixture. The peaks were fit by a Gaussian function, and the expected value (maximum of the peak) for each peak was extrapolated and plotted against the time (Figure 5.12). The analysis of the data suggested that by heating, the position of the first two peaks (related to the T^{th}-O^{th} and O^{th}-O^{th} pairs in the same SiO_4 tetrahedron) did not change whereas the peaks 3-4-5, related to atom pairs of different tetrahedra, approached to the values of Chabazite seeds (r_{CHA}). The local range of the target mixture was fit using experimental PDF patterns collected at RT. In particular, for the refinement, the experimental PDF patterns of the precursors and the calculated PDF pattern of sodium sulfate were used as a model. The scale factor (used to change the signal intensity of the model)

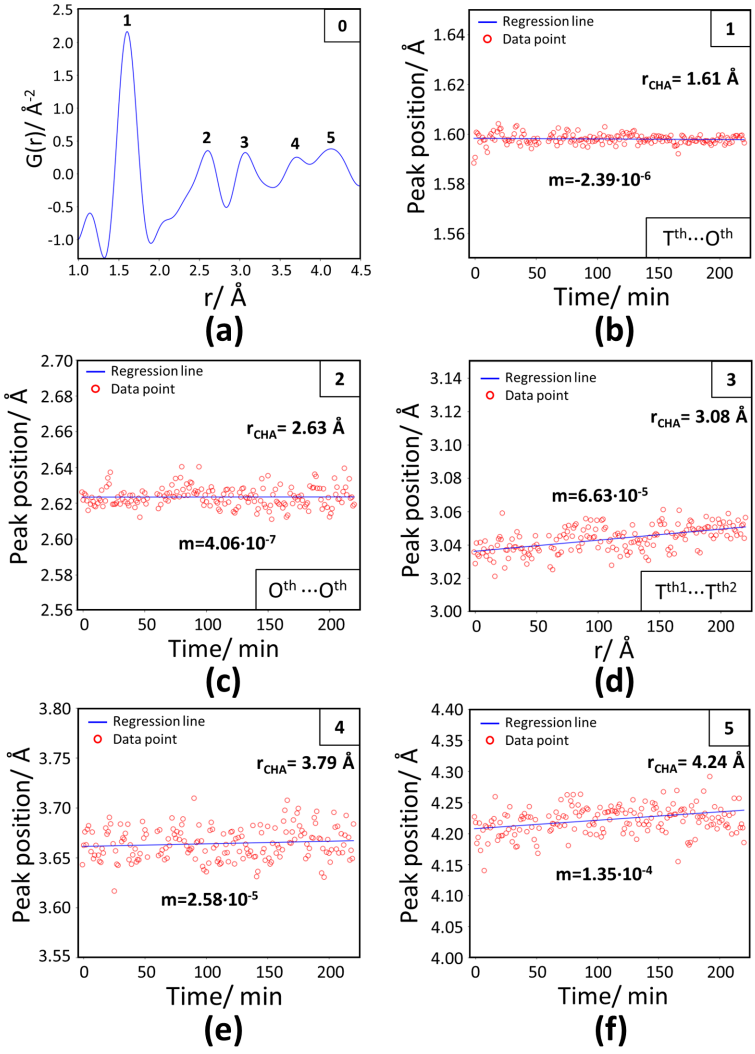

Figure 5.12. (a) PDF pattern of Chabazite seeds at RT (**0**). (b-f) Plots of the expected value of the first five peaks versus reaction time (**1**-**5**). For each plot, the slope value of the trendline (**m**) and the expected value of Chabazite seeds for the studied peak (r_{CHA}) were included.

and the domain size (used to damp the signals at high *r*-value) were the only parameters allowed to refine. Several attempts, using combinations of different experimental patterns as models, were made to obtain the best profile fit. It was observed that sodium silicate, Chabazite, and silica gel contributed to the local-range of the sample (Figure 5.13).

Sequential PDF refinement was performed in order to extrapolate the scale factor values and use them to track the trend of the phases in the reaction system. The model, used to describe the mixture, was again built from a combination of experimental and calculated PDF patterns (Table 5.1). The *r*-value window investigated in the sequential PDF refinement ranged from 0 to 40 Å. During this refinement process, the only value allowed to refine was the scale factor. For the precursors describing the short range order (silica gel, sodium silicate and Chabazite-short range), the domain size values, obtained from the refinement to the first PDF pattern, were fixed during the whole refinement process. For the compounds describing the long range order (sodium sulfate and Chabazite-long range), no domain size factor was used, since they are the

Table 5.1. Information about the PDF patterns used to describe the final model for the sequential PDF refinement.

Type of pattern	**Compound**	**Range order**	**Info**
Experimental	Silica gel	Short	Measured at RT
Experimental	Sodium silicate	Short	Measured at RT
Calculated	Chabazite	Short	From PDF refinement of the model obtained from lab XRPD refinement to the last PDF pattern at 190 °C
Calculated	Chabazite	Long	From PDF refinement of the model obtained from lab XRPD refinement to the last PDF pattern at 190 °C
Calculated	Sodium sulfate	Long	From PDF refinement of the model obtained from lab XRPD refinement to the last PDF pattern at 190 °C

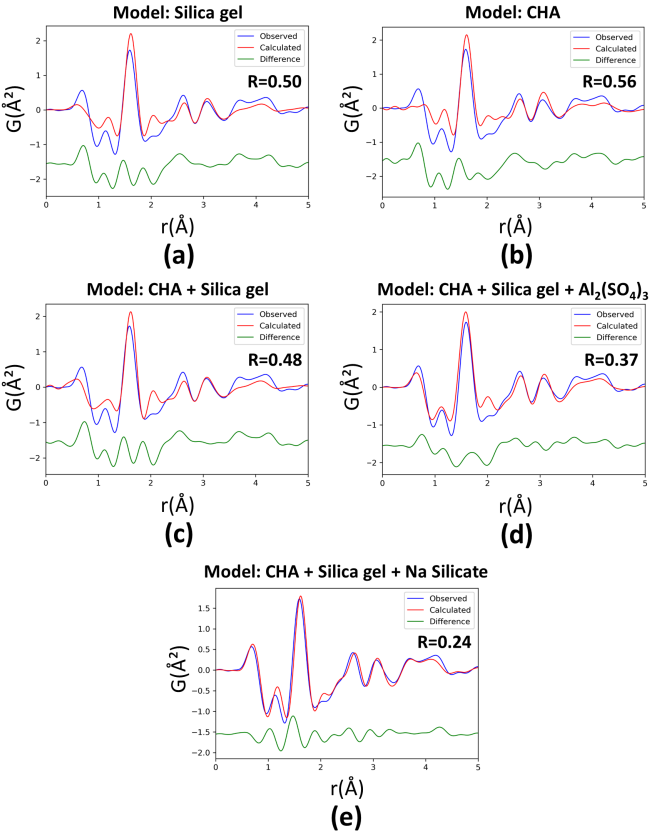

Figure 5.13. PDF patterns of the final reaction mixture at RT. The model was built from a combination of the experimental PDF patterns of: a) silica gel, b) Chabazite seeds, c) Chabazite seeds and silica gel, d) Chabazite seeds, silica gel and aluminium sulfate and e) Chabazite seeds, silica gel and sodium silicate. The observed pattern (blue line), the best fit profile (red line) and the difference curve between the observed and the calculated profile (below) are shown. Agreement factors (**R**) for each refinement are reported in the top-right part of plot.

crystalline components of the mixture with large domain sizes damped by the experimental resolution. The refinement plots of the mixture at RT and 190 °C, right before the end of the thermal treatment, are shown in Figure 5.14.

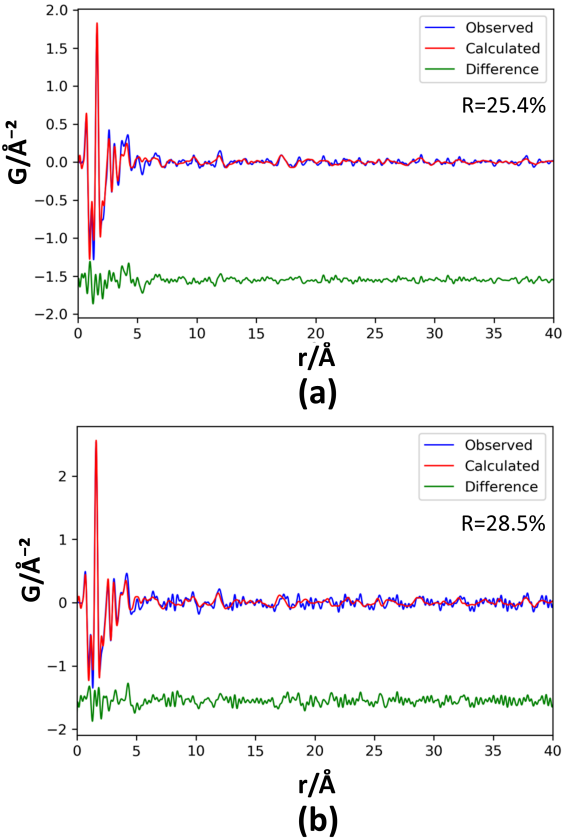

Figure 5.14. PDF patterns of the final solvent-free reaction mixture at RT (a) and right before the end of the thermal treatment at 190 °C (b). The observed pattern (blue line), the best fit profile (red line) and the difference curve between the observed and the calculated profile (below) are shown. The agreement factors (**R**) for each refinement are reported in the top-right part of each plot.

The plot of the scale factor values as function of the reaction time revealed almost no change for the phases describing the short range order (sodium silicate, silica gel and Chabazite-short range) whereas a small formation of crystalline sodium sulfate at the beginning of the reaction and a clear forma-

tion of crystalline Chabazite were observed (Figure 5.15). The results from

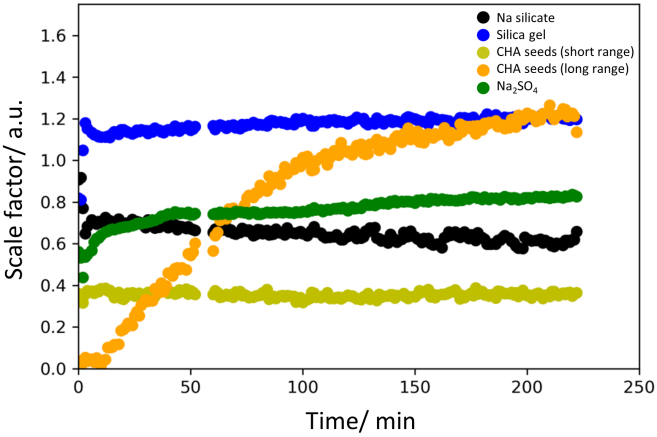

Figure 5.15. Plot showing the scale factor of the precursors and products as function of the reaction time. Sodium silicate (black), silica gel (blue), Chabazite-short range (yellow), Chabazite-long range (orange) and sodium sulfate (green).

sequential PDF refinement showed crystalline Chabazite having a sigmoidal-shape trend like in the sequential Rietveld refinement (Figure 5.9,b).

Kinetic studies on crystalline Chabazite were performed using data coming from sequential peak fitting (reciprocal space approach) and PDF refinement (real space approach). Due to the sigmoidal shape trend, the data can be described by the Avrami equation for the isothermal case (Equation 5.1).

$$\alpha = 1 - e^{-(k(t-t_0))^n} \tag{5.1}$$

Equation 5.1. Avrami equation for the isothermal case. α is the amount of transformed material, k the temperature-dependent rate constant, n the Avrami's exponent which is theoretically related to the crystallization mechanism (it contains terms describing both the number of steps involved in nucleation and the number of dimensions in which the nuclei grow) and t is the reaction time (the induction period is excluded).

The data values (integrated peak area in the first case and scale factor in the second one) were normalized between 0 and 1 and used as input values (α) in the Avrami equation whereas concerning the time values (t), an induction period of 8 minutes was estimated and subtracted. To analyse the data, the Avrami equation must be rearranged to find the n parameter (Equation 5.2). The value of n can be determined by the Sharp-Hancock plots, which is a plot of ln[-ln(1-α)] vs ln(t). This gives a straight line whose slope is the n parameter (Figure 5.16,a-b). This value is used as input value for generating the temperature-dependent rate constant (Equation 5.3), Figures 5.16,c-d).

$$\ln(-\ln(1-\alpha)) = n\ \ln t + c \tag{5.2}$$

$$-\ln(1-\alpha) = k^n t^n \tag{5.3}$$

Equations 5.2-5.3. Rearranged Avrami equation for the isothermal case used for extrapolating the n (5.2) and k (5.3) parameters.

From Table 5.2, it can be observed that both approaches give very similar n and k values. No discussion is done about the meaning of the n value and how this can be related to the crystalline growth and nucleation process. The results from the kinetic study indicated that both approaches give consistent results and could be used for future experiments. It is worth noting that the PDF method could also be used in cases where the reciprocal space method fails due to amorphous/nanocrystalline reactants and products.

Table 5.2. List of n and k values for the reciprocal and real space approach.

Parameter	**Values**	
	Reciprocal space (XRPD)	**Real space (PDF)**
n	1.26(1)	1.07(1)
k/min^{-1}	0.0149(2)	0.0144(1)

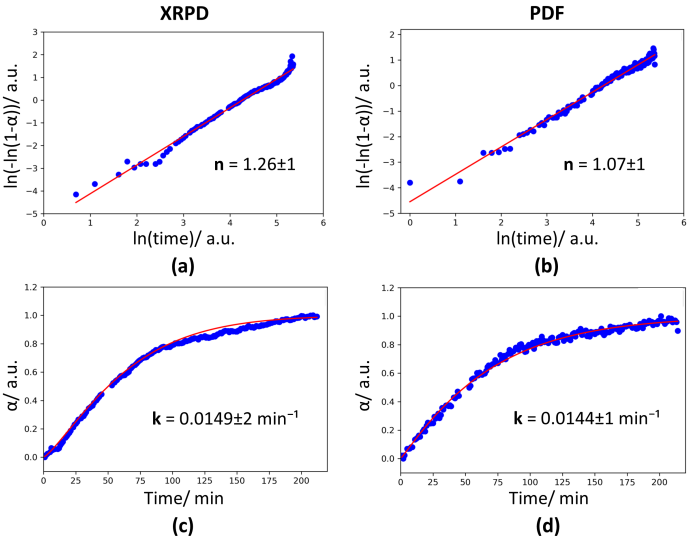

Figure 5.16. Plots of ln(-ln(1-α)) versus ln(time) (a,b) and α versus time (c,d) for the reciprocal (left) and real (right) space approach. The n and k values are also reported.

5.2.2 Solvent-based approach

The solvent-based synthesis of Chabazite through interzeolite trasformation from Zeolite Y was monitored through XRPD *in situ* experiments using the laboratory source. Time-dependent *in situ* XRPD measurements were performed on a suspension that was freshly prepared in the lab right before the experiment. The first XRPD pattern collected at 190 °C clearly showed the presence of Zeolite Y, as the only crystalline compound in the suspension (Figure 5.17). The time-dependent XRPD experiments revealed the fast formation of the crystalline Chabazite product (Figure 5.18). Interestingly, the interconversion of the two zeolites is not instantaneous but co-existence of the two zeolites was observed for a long period of time before Zeolite Y completely transformed to Chabazite. This behavior is expected for a solid reaction that proceeds by nucleation and growth of the forming crystalline phase.

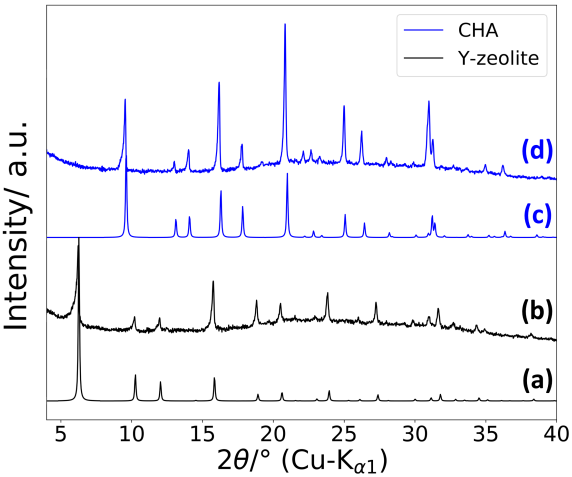

Figure 5.17. Stacking plot showing XRPD patterns of (a) calculated and (b) experimental Zeolite Y at the beginning of the reaction at 190 °C (black) and XRPD patterns of (c) calculated and (d) experimental Chabazite at the end of the reaction at 190 °C (blue).

Sequential fitting of the (111) peak for the Zeolite Y and 100 peak for Chabazite was performed in order to extrapolate the integrated area (Figure 5.19). The plots of the normalized integrated area of the chosen peaks versus

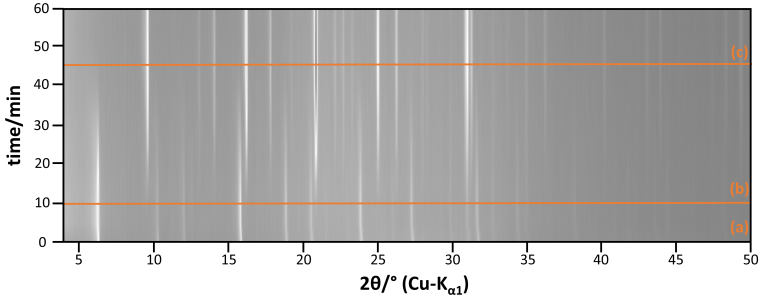

Figure 5.18. Time-dependent *in situ* XRPD measurement of sample A at 190 °C showing: (a) Zeolite Y, (b) Zeolite Y and formation of Chabazite, (c) Chabazite.

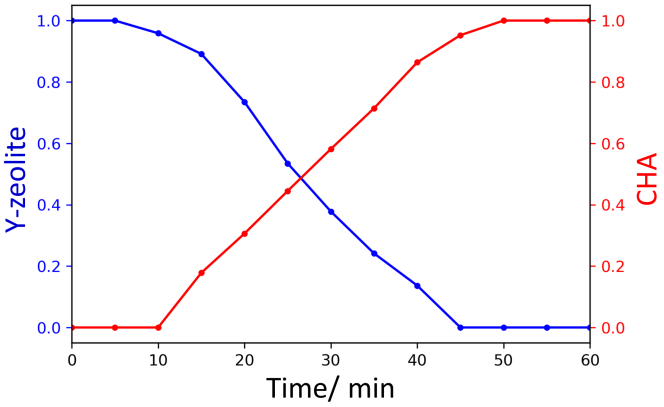

Figure 5.19. Plot of normalized integrated peak area showing the consumption of Zeolite Y (blue) and the formation of Chabazite (red) as function of time.

time revealed a sigmoidal trend for the Chabazite product and a gradual consumption of Zeolite Y during the reaction.

An attempt to study the kinetics of the crystalline formation of Chabazite was done using data coming from sequential peak fitting. Due to the sigmoidal shape trend, the data can be described by the Avrami equation for the isothermal case. As in the solvent-free approach, the data values (integrated peak area) were normalized between 0 and 1 and then used as input values (α) in the Avrami equation. Concerning the time values (t), an induction time of 10 min was estimated and subtracted. From the fitting of the Avrami equation to the data, n and k values were extrapolated (Figure 5.20,a). A careful inspection of the Sharp-Hancock plot revealed a change in the slope (Figure 5.20,b). When a change in the slope is observed, it suggests a change in the reaction mechanism related to the nucleation or crystal growth process. The change was observed after 35 minutes (α=0.73) from the starting of the measurement.

The product, after the thermal treatment, was further investigated by SEM in order to check the morphology and the size, which play an important role on the catalytic performance. SEM images showed the presence of the char-

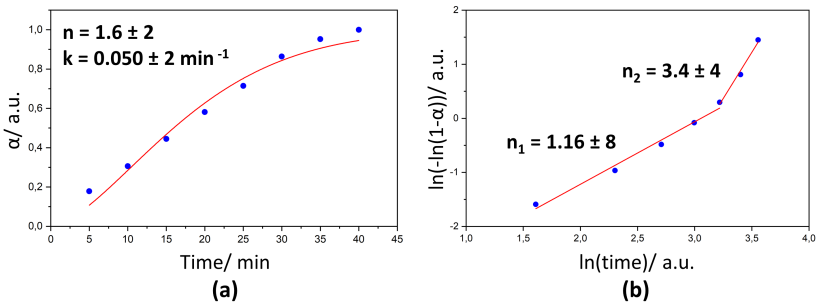

Figure 5.20. Plots of α versus time (a) and ln(-ln(1-α)) versus ln(time) (b) for the solvent-based synthesis approach. The n and k values are also reported.

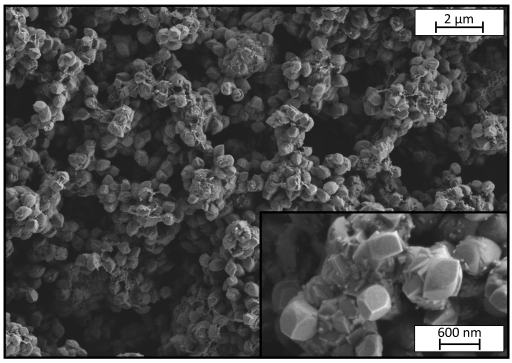

Figure 5.21. SEM image showing the presence of pseudo-cubic particles of Chabazite with dimensions ranging between 400-600 nm.

acteristic pseudo-cubic particles of Chabazite with dimensions ranging between 400-600 nm (Figure 5.21).

5.3 Conclusions

In this chapter, two approaches for ultrafast synthesis of Chabazite crystals were investigated through X-ray powder diffraction and electron microscopy. In the solvent-free approach, the mixture heated at 190 °C was analysed through sequential Bragg peak and PDF refinements using synchrotron X-ray diffraction data. The investigation confirmed the presence of crystalline

sodium sulfate originating from the mixing stage prior and not during the heating process. The short range order was probed through PDF refinements revealing that silica gel, Chabazite seeds, and sodium silicate are the most abundant phases. Kinetics studies using the Avrami equation for solid state reactions were performed on the results obtained from the Bragg peak and PDF refinements. The results showed that both approaches give consistent results and PDF could be used for future experiments especially in cases of amorphous or nanocrystalline reactants where reciprocal space approaches fail. In the solvent-based approach, the investigation of the reaction was performed with laboratory data. Sequential peak refinements to the *in situ* XRPD data at 190 °C revealed the co-existence of the precursor and the product for a long period of time before the Zeolite Y completely transformed to Chabazite. This is a behaviour expected for a solid reaction that proceeds by nucleation and growth of the forming crystalline phase. In addition, the kinetics study shows the possible presence of two reaction mechanisms related to the nucleation and crystal growth process.

This study contributed to elucidating the synthetic process of both approaches and developing an understanding of the kinetics of the reactions, which could be used to transfer the whole process to the plant level.

5.4 Experimental section

Samples

Samples were freshly prepared before each experiment according to the recipes designed by BASF SE. For the solvent-free approach, silica gel (29.5 wt-%), sodium silicate (30.4 wt-%), aluminum sulfate (13.1 wt-%), and Chabazite seeds (3.6 wt-%) were added to a 50 wt-% aqueous solution of TMdAOH (22.4wt-%) and water (VE, 1.0 wt-%). The solid solution was stirred with a spatula before measuring it. For the solvent-based approach, Y zeolite (16.45 wt-%) was added to a solution composed by the template (24.36 wt-%) and NaOH (10% water solution, 59.19 wt-%). The suspension was stirred with a magnetic stirrer for 20 minutes.

SEM

SEM images were collected with a Merlin SEM from Zeiss at an accelerating voltage of 1.5 kV whereas SEM/BSE images and EDX analysis were obtained with TESCAN Vega TS 5130 equipped with X-Man^N 20 SDD (Oxford instruments).

X-ray powder diffraction

1) Laboratory source

The XRPD patterns were collected on a laboratory powder diffractometer in Debye-Scherrer geometry (Stadi P- Diffractometer (Stoe), Cu-$K_{\alpha 1}$ radiation from primary Ge (111)-Johann-type monochromator, 3 Mythen 1K detectors (Dectris)). For the *in situ* XRPD experiments of the solvent-based suspensions, the XRPD patterns were measured in a 2θ range from 2.0° to 54° for 5 minutes. No delay time was applied between each measurement. The temperature was adjusted using an Oxford Cryosystem device (Oxford Cryosystem). Pawley and Rietveld refinements were performed with the program TOPAS 6.0 [64].

1) Synchrotron light source

Time-dependent *in situ* synchrotron X-ray total scattering measurements at 190 °C used for both XRPD and PDF analysis were carried out at beamline P02.1 at Petra III synchrotron (DESY, Germany) in a capillary transmission geometry. The wavelength used for the experiment was 0.20699Å (≈60KeV) and the 2D-detector was a PerkinElmer XRD1621. The capillary was spun during the measurements and the temperature was adjusted using an Oxford Cryosystem device (Oxford Cryosystem). A standard (nickel), all the precursors, empty capillary (used as background) and the final mixture were measured in a 2θ range from 0.55° (Q≈0.29 $Å^{-1}$) to 57.08° (Q≈29 $Å^{-1}$) applying a total scan time of 1 min per measurement. Chabazite seeds and the empty capillary were measured at RT and 190 °C, whereas the other precursors only at RT. At the beginning, the total mixture was measured at RT, and then the nozzle of the cryosystem device (already set at 190 °C) was moved close to the sample. The mixture was measured at 190 °C for a total of 220 min,

beyond which no further change in the patterns was observed. Pawley refinement was performed with the program TOPAS 6.0 [64].

6 Crystal structure of 1,4-dinitrosobenzene polymer

The following chapter presents the study of an organic polymer, which can potentially be used as a wide-bandgap semiconductor (WBG). In particular, the polymer poly(1,4-phenylenazine-N,N-dioxide) (PDNB), obtained from polymerization of 1,4-dinitroso benzene, was investigated by X-ray powder diffraction (XRPD), solid-state NMR (ssNMR) and thermal analyses (TGA/ DSC/ DTA). This study was done in collaboration with the research group of Prof. Hrvoj Vančik from the University of Zagreb (Croatia) who provided the sample, performed DFT calculations and studied the reversibility of the polymerization reaction. The results are published the journal *POLYMER* (2020) [143].

6.1 Introduction

C-nitroso compounds are a class of organic molecules having the nitroso group (R-N=O) attached to a carbon atom. When R is an aryl group, aromatic C-nitroso compounds, a particular subset of nitroso compounds, can

be obtained. Despite their long chemical history, aromatic C-nitroso compounds continue to draw the attention of many scientists [144, 145]. This ongoing interest is in part due to their numerous application in synthetic organic chemistry [146, 147], their role as reactive metabolites [148, 149] and their use as spin traps [150, 151]. Another reason is the characteristic property of these molecules to participate in a monomer-dimer equilibrium, which can be exploited as a molecular ON-OFF switch. Indeed, even without any special condition, monomers undergo a reaction that gives *Z*- and *E*-azodioxy dimers (Figure 6.1). This phenomenon is mainly attributed to the energy of

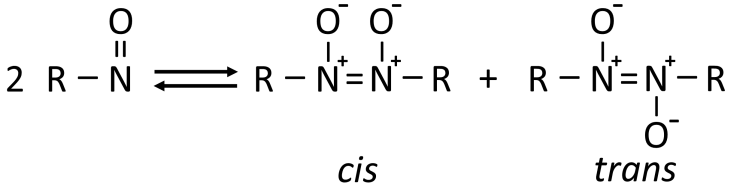

Figure 6.1. Schematic plot of the dimerization reaction of two C-nitroso molecules giving azodioxide compounds. The two possible geometric isomers (*cis-trans*) are also depicted.

the N=N bond, which is weaker than a covalent bond and stronger than an hydrogen bond, and to the low activation energy of the dimerization process (less than 50 KJ/mol) [145]. At cryogenic temperatures, crystalline azodioxides undergo photodissociation, which produces nitroso forms, while thermal re-dimerization occurs above 80 K [152]. Interestingly, the dimerization process can visually be monitored due to the different color of the monomer (green or blue) and the product (colorless or pale yellow). The equilibrium can be tuned by varying structure (substituents on the monomer) or environmental conditions. For instance, the monomer is favoured in solution whereas the dimer in the solid state.

When a dinitroso aromatic compound is used, polymers can be obtained through a 'living' polymerization [153], which does not require any special conditions for initiation. The simplest azodioxide polymer, poly(1,4-phenyleneazine-N,N-dioxide) (PDNB, **1**), can be obtained using 1,4-dinitroso-

benzene as monomer (Figure 6.2). In the past, the research groups of Hacker

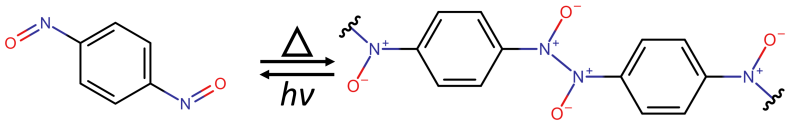

Figure 6.2. Schematic plot of the polymerization reaction of **1**.

[154, 155] and Vančík [156, 157] investigated the formation and stability of this compound. These studies showed that PDNB is extraordinarily stable against solvents, acids, and bases as well as having very low solubility in organic solvents. Also, in the solid form, it can form crystals on the submicrometer scale.

In addition, this polymer appears to be 100% recyclable [155]. Indeed, photolysis of **1** occurs at 12-15 K yielding the starting monomers, which by heating to 120 K or more, re-polymerize to the starting polymer. The thermal re-dimerization process is a fast process with low enthalpy of activation (14.1 to 15.5 kJ mol^{-1}) and high negative entropy of activation (-179.7 to -183.0 J K^{-1} mol^{-1}) [157]. The low activation enthalpy has been explained by the findings that nitroso groups, appearing in the solid after the photolysis of azodioxide, retain their spatial position with the N-atoms close to each other (topochemical argument) [158]. This hypothesis is additionally supported by the fact that the polymerization of 1,4-dinitrosobenzene, starting from the deposited monomer *in vacuo* on the cooled surface, follows a different mechanism with the parallel formation of both forms, the *E* and the *Z* azodioxides, respectively [156].

The alternate aromatic and azodioxide planes could be the origin of interesting physical properties in photoelectronics: indeed, the extent of the conjugated double bond system, depending on the angle between these two planes, might affect its conductivity. Additionally, Hacker previously reported an absorption band of a film made of **1** at 400 nm [154]. This spectral characteristic suggests an unusually low bandgap, which is an important feature for organic semiconductors, a fast-developing class of compounds, used as solar cells,

quantum dots or photodetectors [159–161].

In this project, the crystal structure of **1** was investigated by using XRPD with the aim to support the topochemical argument of the mechanism of polymerization and re-polymerization of the 1,4-dinitrosobenzene proposed in the past. Additionally, the crystal structure was used for DFT calculations in order to elucidate the electronic structure of **1**. Eventually, the thermal stability of **1** is investigated by TGA/DSC/DTA analysis in dynamic oxygen and argon atmospheres and temperature dependent *in situ* XRPD measurement.

6.2 Results and discussion

Compound **1** was initially investigated by XRPD in order to determine the crystal structure. The obtained structure revealed that the polymer crystallizes in the monoclinic space group $P2_1/n$[1] (a = 6.3858(2) Å, b = 11.2812(4) Å, c = 3.6984(1) Å, β = 92.209(6)° and V = 266.233(15) Å^3, Table 6.1). The projections of the crystal structure along the crystallographic axes are depicted in Figures 6.3-6.4. The asymmetric unit contains half of the monomer located close to a centre of inversion. Structure solution reveals that the compound polymerizes with the azodioxide group in the *E* configuration. As a consequence, the crystal is made up of linear chains running parallel along the crystallographic *a*-axis and stacked along the *c*-axis. The atoms in the polymeric chains lie on two different planes running in alternative fashion: one plane is defined by the aromatic ring and the other by the ONNO azodioxide system . The planes are rotated by a dihedral angle of 48.9(3)° (Figure 6.6). CH···O interactions between the oxygen and the arene-related hydrogen atoms (C···O distance: 3.110 Å, CHO angle: 128.24°) and running along the [011] direction are responsible for the connection of one polymeric chain with four other chains (Figure 6.7).

Inspection of the XRPD pattern (Figure 6.5) of the polymer shows anisotropic line-shape broadening. This feature was modelled by applying the phe-

[1] $P2_1/n$ was preferred over the standard cell setting $P2_1/c$ because of the monoclinic angle being close to 90°.

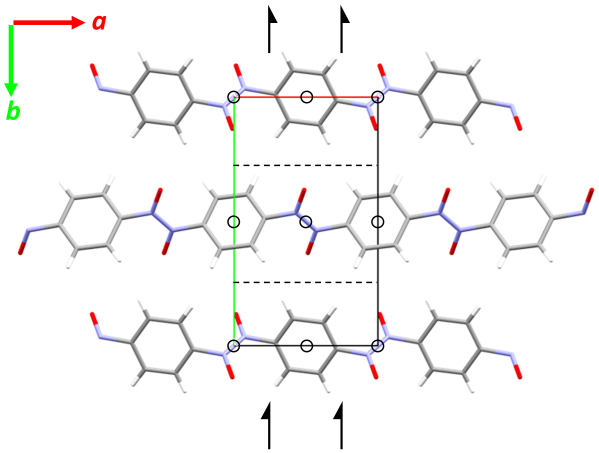

Figure 6.3. Projection of the crystal structure of **1** along the crystallographic *c*-axis together with the symmetry elements.

nomenological Stephens model for the monoclinic crystal system as defined in TOPAS [162]. The model was introduced to compensate the disorder in the crystal structure, which leads to the anisotropic broadening of the reflection (appearing as microstrain) [163,164]. Figure 6.8 shows the three-dimensional distribution of the micro strain and its two-dimensional projection on the *yz* plane (corresponding to *bc* plane). The strain is minimum along the polymeric chain direction along *x* (*a*-axis) but maximum along the diagonals of the *yz* plane (corresponding to the shortest distance between neighbouring stacks of chains, which are shifted by *c*/2 (Figure 6.4, a).

ssNMR was used to further confirm the crystal structure model, the polymeric nature of the compound, and the absence of impurities (Figure 6.9). The ^{13}C CP-MAS spectrum exhibits two signals at 121.9 and 139.0 ppm corresponding to the three crystallographically independent carbon atoms in the asymmetric unit of the crystal structure. The presence of two peaks is attributed to the same chemical environment of two carbon atoms that makes them indistinguishable at the NMR. However, the integrated intensity ratio of 2 between the two signals matches the double abundance of the carbon atom

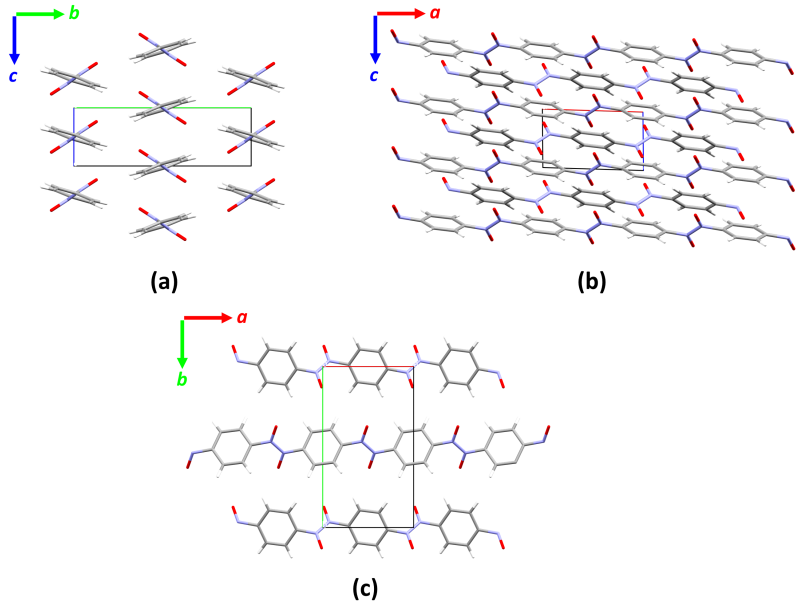

Figure 6.4. Projections of the crystal structure of **1** along the crystallographic *a* (a), *b* (b) and *c* (c) axes.

bound to nitrogen with respect to the carbon atom belonging to the rest of the benzene ring. The ^{15}N NMR spectrum showed only one nitrogen signal at 82.7 ppm and there are no detectable peaks related to nitroso end-groups, as expected for a polymer without impurities and full polymerization.

Compound **1** was further analysed by thermal analyses (TGA/DSC and TGA/DTA) and temperature dependent *in situ* XRPD measurements in order to investigate the thermal behaviour. The thermal analyses were conducted in two different atmospheres to observe differences in the thermal behaviour of the polymer when exposed to oxidizing and inert atmospheres (Figure 6.10). The analysis of the two measurements reveals that the polymer is thermally stable up to 100°C. A weight loss in the TG curve (Δm_{exp}= 78.4 wt-% in Ar-flow and Δm_{exp}=69.0 wt-% in O_2-flow) associated with a sharp exothermic peak in the DTA/DSC curves is observed in both measurements. This could be attributed either to a depolymerization or to a decomposition pro-

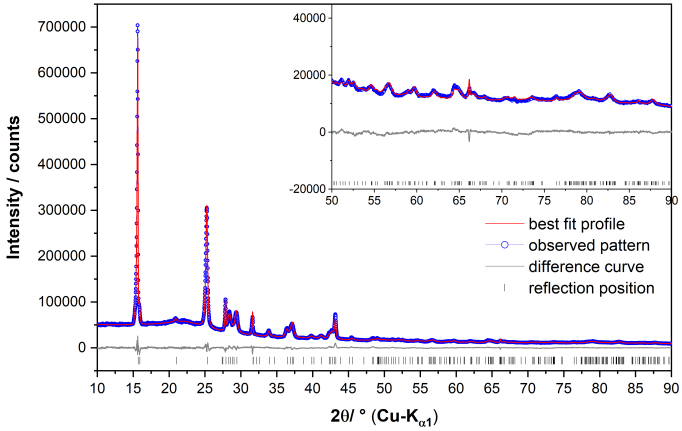

Figure 6.5. Scattered X-ray intensities of **1** at ambient conditions as a function of diffraction angle 2θ. The observed pattern (circles) measured in Debye-Scherrer geometry, the best Rietveld fit profile (line), the difference curve between the observed and the calculated profile (below), and the calculated reflection positions (vertical tick marks) are shown. The high angle part starting at 50° in 2θ is enlarged for clarity in the inset. Adapted from [143].

cess, which could be vigorous in presence of oxygen as it can be seen from the feature at 200°C in the TG curve (the measurement was carried out twice

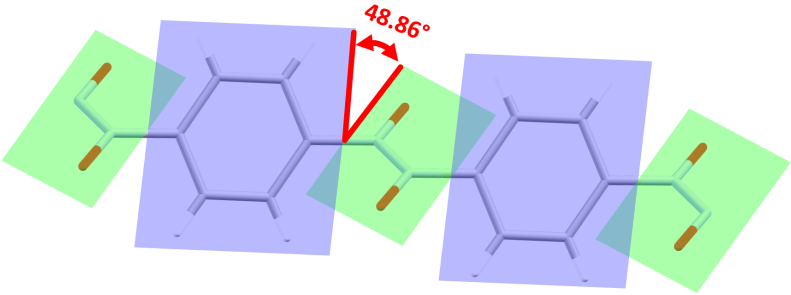

Figure 6.6. View of the dihedral angle between the planes defined by the aromatic ring (blue) and the ONNO azodioxide system (green). The value of the angle is showed in red.

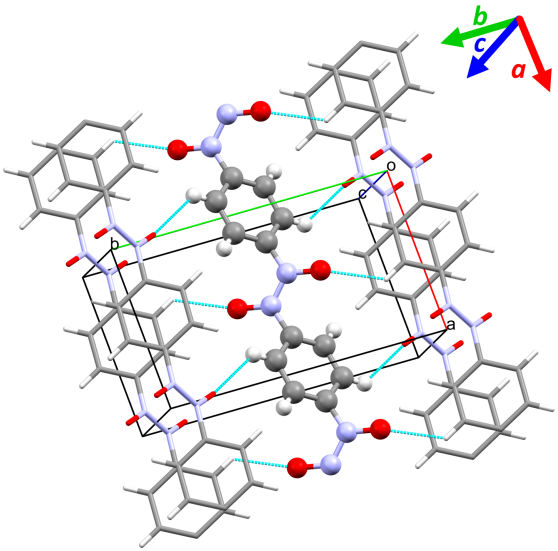

Figure 6.7. View of the CH···O interactions between the oxygen and the arene-related hydrogen atoms. The interactions are depicted in light blue.

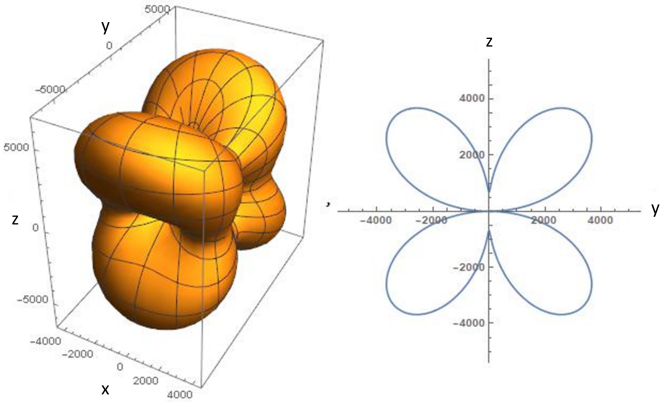

Figure 6.8. Representation of the distribution of the anisotropic strain in **1** (arbitrary units) in 3D (left) and in 2D projections on the *yz*-plane (right). Adapted from [143].

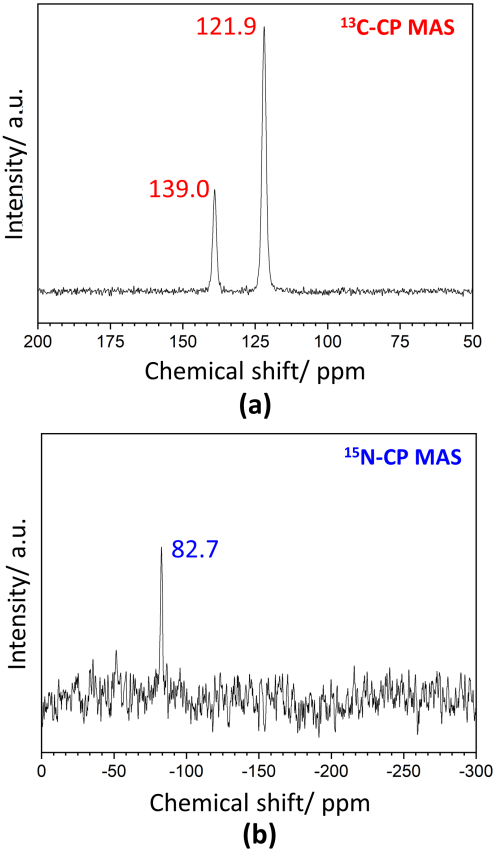

Figure 6.9. ^{13}C (a) and ^{15}N (b) CP/MAS ssNMR spectra of **1**.

to confirm it). In the measurement with argon flow, this step is followed by a gradual weight loss (Δm_{exp}= 6.6 wt-%) in the temperature range (200-800)°C associated with a broad exothermic peak. At the end of the measurement, the crucible contained a black residue (Δm_{exp}= 15 wt-%). Instead, the measurement in the presence of oxygen reveals a two-step decomposition process with the second weight loss of circa 27.9 wt-% associated with a broad exothermic peak. After the thermal process, a very tiny amount of decomposition residue was still present in the crucible (Δm_{exp}= 3.1 wt-%). Temperature dependent

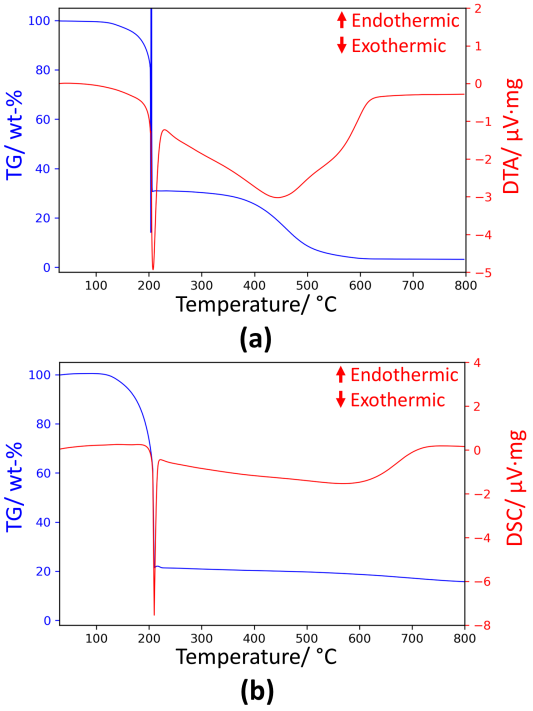

Figure 6.10. TG (blue line) and DTA (red line) curves of **1** measured in dynamic oxygen atmosphere (a), and TG (blue line) and DSC (red line) curves of **1** measured in dynamic argon atmosphere (b).

in situ XRPD measurements were performed to further investigate the thermal behaviour of the polymer (Figure 6.11). The temperatures deviate from those in the thermal analyses due to the different atmospheres and sample environment (static and closed capillary for XRPD measurements, whereas dynamic and Al_2O_3 crucible for the thermal analyses). The experiment shows the stability of the sample until around 150°C where the decomposition occurs without any crystalline intermediate. After the experiment, the capillary contained a small amount of white solid.

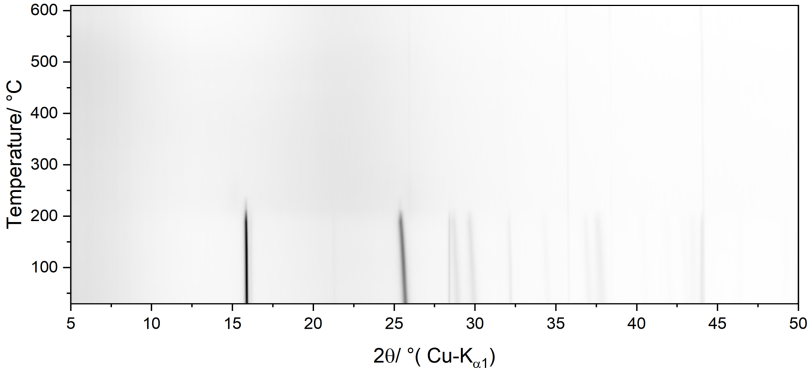

Figure 6.11. Temperature dependent *in situ* XRPD measurement showing the thermal stability of **1** until approximately 150 °C. Artefacts from the oven are visible at high temperatures.

6.3 Conclusions

In this work, the solution for a long-standing problem was achieved: the crystal structure of **1** was successfully determined by XRPD after almost thirty years of its discovery. The crystal structure was used by the research group of Prof. Vančik as model for DFT calculations to investigate electronic properties, such as semiconducting properties. Since the gap between conducting and valence bands is 2.3 eV, **1** could be classified as a wide-bandgap (WBG) semiconductor that absorbs in the spectral region around 400 nm. In addition, the research group of Prof. Vančik observed that photolysis of **1** at cryogenic temperatures (15K) yields monomers that can re-polymerize at temperatures higher than 80K giving the original polymorph. This result, as well as the observed regularity of the molecular arrangements in the crystal lattice, indicate that after the photolysis, monomeric molecules retain their positions in the crystal. Such a topochemical condition explains the low activation enthalpy (14.1 to 15.5 kJ mol-1) that has previously been measured for polymerization. These properties, as well as its high stability against heat (up to 150 °C in a static air atmosphere of a closed capillary) and resistance to organic solvents show that this material is a promising candidate for molecular

photoelectronic devices.

6.4 Experimental section

Sample and DFT calculation

Synthesis of the sample and DFT calculations were performed by the research group and collaborators of Prof. Vančik according to the publication [143].

Thermal analysis

Thermal analyses were carried out using a STA 449 F5Jupiter (Netzsch) device for TGA/DTA- and TGA/DSC-measurements. For both measurements, the sample was placed in Al_2O_3 crucible and heated from 30 °C to 800 °C with a heating rate of 5 °C/min in a 20 mL/min Ar-/O_2-stream. An empty crucible was used as reference material.

Solid-state NMR

Solid-state NMR spectra were collected on a Bruker Neo 600 with a magnetic field of 14.1 T. ^{13}C and ^{15}N ssNMR spectra were obtained under Cross-Polarization Magic Angle Spinning conditions at Larmor frequencies of 150.9 MHz and 60.83 MHz, respectively.

X-ray powder diffraction

XRPD measurement for structure solution and Rietveld refinement of **1** was carried out at room temperature on a Stadi-P Diffractometer (Stoe) in Debye-Scherrer geometry with Cu-$K_{\alpha 1}$ radiation from primary Ge(111)-Johann-type monochromator and 3 Mythen 1K detectors (Dectris). The sample was loaded into a 0.5 mm diameter boroglass capillary (WJM-Glas/Mueller GmbH), which was spun during the measurement. The pattern was measured in the 2θ range from 0° to 110.0°. A total scan time of 12 hours was applied.

Temperature dependent *in situ* XRPD measurement was carried out on a Bruker D8-Advance powder diffractometer in Debye-Scherrer geometry with Cu-$K_{\alpha 1}$ radiation from primary Ge(111)-Johannson-type monochromator and

Table 6.1. Crystallographic and Rietveld refinement data of compound **1**.

Compound	**1**
Crystal system	Monoclinic
Space group (No.)	$P2_1/n$ (14)
Wavelength/ Å	1.5406
a/ Å	6.3858(2)
b/ Å	11.2812(4)
c/ Å	3.6984(1)
β/ °	92.209(6)
V/ Å^3	266.23(2)
Z	4
T/ K	298
Refined parameters	36
D_{calc}/ g·cm^{-3}	1.70
R_{wp}/ % [a]	3.53
R_p/ % [a]	2.56
R_{Bragg}/ % [a]	1.74
Starting angle measured/° 2θ	0
Final angle measured/° 2θ	110
Starting angle used/° 2θ	10
Final angle used/° 2θ	75
Step width/° 2θ	0.01
Time/ h	12

[a] As defined in section 2.2.3.

Våntec detector. The sample was loaded into a 0.5 mm diameter quartz capillary, which was spun during the measurements. The patterns were measured in the 2θ range from 5.0° to 50.0°. A total scan time of 3 hours was applied per measurement. The temperature was adjusted using a TC-transmission furnace (mri). The sample was heated from 30 °C to 410 °C in 20 °C steps and from 410 °C to 610 °C in 50°C steps with a heating rate of 5 °C/min. During each step, a diffraction pattern was collected after a delay time of 5 minutes to ensure thermal equilibration of the sample.

Indexing, space group determination, Pawley refinement, crystal structure solution through Simulated Annealing and Rietveld refinement were performed with the program TOPAS 6.0 [64].

7 Metal thiocyanate coordination compounds

This chapter deals with the study of different metal thiocyanate coordination compounds. In particular, structure solutions and refinements as well as investigation of the thermal transformation of different coordination compounds with the general formula $M(NCS)_2L_n$ (with M as divalent transition metal and L as a neutral co-ligand) were carried out using XRPD. This study was done in collaboration with the research group of Prof. Christian Näther from the Christian-Albrechts University in Kiel (Germany) who provided the samples. The results were included in several publications [165–170].

7.1 Introduction

Metal thiocyanate coordination complexes with formula $M(NCS)_2L_n$ (n = 1, 2, 4) are composed of a divalent transition metal (M^{2+}), a neutral co-ligand (L), and the thiocyanate group (NCS).

The thiocyanate ion is a pseudohalide for the similarity of its reactions to that of halide ions and, together with cyanate and selonocyanate, belongs to the chalcogenocyanates. Thiocyanate is a versatile ligand for the property of being either ambidentate or a bridging ligand. Indeed, this group can coordinate to a Lewis acid using either N or S atom or it can bridge two metal ions with both terminal sides. This preference depends on many factors such as

the nature of the metal ions, the type of co-ligand, and whether the complex is in the solid state or in solution [171].

The ability of thiocyanate to show multiple coordination modes drew the attention of many scientists in the last decades since a large number of coordination compounds with different topologies of the coordination networks can be obtained [172, 173].

The synthetic procedures of thiocyanate coordination complexes are similar to those of the coordination compounds or polymers, which are generally synthesized from solution. However, although the use of solvent can be convenient for substance separation or product crystallization, it actually may coordinate the metal centres giving different results than expected [174]. Therefore, other synthetic routes, based on solvent-free approaches, were developed in last years, such as the synthesis in a molten-flux of the organic ligands [175, 176] or the molecular milling synthesis [177–179]. An alternative approach, frequently used by the research group of Prof. Näther in Kiel, is the thermal decomposition of suitable discrete coordination complexes with a higher number of ligands. These coordination compounds are intentionally synthesized to be decomposed by controlled heating. Under this process, the ligands are stepwise released, whose now empty coordination sites are replaced by thiocyanate acting as bridging ligand. As a consequence, the formation of previously unknown compounds with condensed networks of higher dimensionality can be obtained. In particular, through the irreversible removal of ligands, metastable polymorphic or isomeric modifications, which cannot be accessible in solution [180], may be synthesized in quantitative yields [181, 182] (Figure 7.1).

However, using this approach, crystals suitable for single crystal X-ray diffraction (SC-XRD) are difficult to obtain. Therefore, structural information have to be extracted by XRPD using either *ab initio* structure solution (*e.g.* simulated annealing) or Rietveld refinement. For the latter case, the required starting model is obtained by exploiting the different chemical affinity of the transition metals for the thiocyanate related nitrogen or sulphur atom. Indeed, structural models for new metastable coordination polymers, contain-

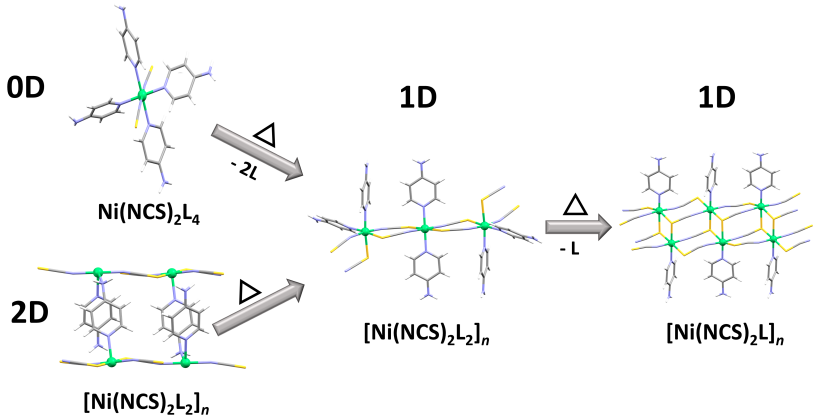

Figure 7.1. Schematic plot of the structural changes in nickel thiocyanate coordination complexes by controlled thermal decomposition (L = 4-aminopyridine, 0D = discrete complex, 1D = mono-dimensional network (chain), 2D = two-dimensional network (layer)) adapted from Neumann *et al.* [181].

ing less chalcophilic metals (such as Mn^{II}, Fe^{II}, Co^{II} and Ni^{II}) bridged by the thiocyanate ligands, can be obtained by crystallizing from solution the isomorphous compound with a more chalcophilic metal (*e.g.* Cd^{II}), which can be easily characterized by SC-XRD.

The discovery of new structures, in most cases polymorphic modifications, with different atomic arrangement led scientists to explore their properties and correlate them to the structure. Previous studies demonstrated that thiocyanate coordination complexes exhibit several interesting properties such as magnetism [181, 182], non-linear optics [183], luminescence [184, 185] and fluorescence [186, 187]. All these properties are mostly related to the type of the metal and the different connectivities of the ligands. Therefore, these properties can be properly tuned by choosing appropriate metal ions and ligands or by triggering a transition from a less active crystalline phase to a more active one.

In this project, an important contribution to the identification of new crystalline forms of metal thiocyanate coordination compounds and the develop-

ment of new synthetic routes in the solid-state has been given. In particular, crystal structures of thiocyanate coordination compounds with Mn(II), Fe(II), and Cd(II) as metal centres and 4-picoline, 2-methoxypyridine and 4-cyanopyridine as neutral co-ligands were determined *ab initio*, and by Rietveld refinement using XRPD. Furthermore, the synthesis of these compounds by thermal decomposition of precursors were investigated by temperature dependent *in situ* XRPD measurements.

7.2 Results and discussion

7.2.1 Cadmium thiocyanate coordination complexes

Systematic studies of cadmium thiocyanate with 4-methoxypyridine led to the formation in solution of four different compounds. Two of them were successfully obtained as single crystals and consequently characterized by SC-XRD. No crystals suitable for SC-XRD characterization were obtained for the other two compounds (**Cd-I** and **Cd-II**) and therefore, the crystal structures were determined by XRPD.

Prior to the structure solution, both compounds were characterized by elemental analysis and IR spectroscopy in order to extract information about the molecular structure that can support the structure solution by XRPD. The first analysis revealed that both compounds have the composition $Cd(NCS)_2$(4-methoxypyridine)$_2$, suggesting that they are polymorphs. The IR spectra exhibited CN stretching vibrations at 2045 cm^{-1} for **Cd-I** and 2042 cm^{-1} for **Cd-II** indicating that the thiocyanate anions coordinate the metal exclusively through the nitrogen bond. As a consequence, both compounds should consist of discrete complexes with no bridging thicyanate ions.

Since the two crystal structures consist of discrete complexes, single crystals of Mn $(NCS)_2$(4-methoxypyridine)$_4$, where manganese is a less chalcophilic metal and therefore thiocyanate-bridged complexes are less favoured, were synthesized to obtain a structural model for XRPD characterization. The

analysis of the XRPD spectra confirmed that the structure of the manganese-based complex is isotypic and isomorphous to **Cd-I**. Therefore, the structure of **Cd-I** was determined by Rietveld refinement using the atomic coordinates of the isotypic manganese structure as starting point, whereas structure determination of **Cd-II** was performed *ab initio* using the simulated annealing method.

Compound **Cd-I**, isotypic to $Mn(NCS)_2(4\text{-methoxypyridine})_4$, crystal-

Table 7.1. Crystallographic and Rietveld refinement data of compounds **Cd-I** and **Cd-II**.

Compound	**Cd-I**	**Cd-II**
Crystal system	Monoclinic	Tetragonal
Space group (No.)	*C*2/*c* (15)	$P4_1$ (76)
Wavelength/ Å	1.5406	1.5406
a/ Å	18.8364(7)	13.9707(2)
b/ Å	9.7410(4)	13.9707(2)
c/ Å	19.0174(7)	15.6984(2)
β/ °	119.237(3)	90
V/ $Å^3$	3044.9(2)	3064.02(6)
Z	4	4
T/ K	295	295
Refined parameters	42	63
D_{calc}/ $g \cdot cm^{-3}$	1.70	1.44
R_{wp}/ % [a]	2.86	4.29
R_p/ % [a]	2.27	3.17
R_{Bragg}/ % [a]	1.10	1.69
Starting angle measured/ ° 2θ	1	6
Final angle measured/ ° 2θ	110	60
Starting angle used/ ° 2θ	6	6
Final angle used/ ° 2θ	80	60
Step width/ ° 2θ	0.015	0.015

[a] As defined in section 2.2.3.

lizes in the monoclinic space group *C*2/*c* (a = 18.8364(7) Å, b = 9.7410(4)

Å, c = 19.0174(7) Å, β = 119.237(3) °, and V = 3044.9(2) Å^3, Table 7.1). The asymmetric unit consists of one thiocyanate and two 4-methoxypyridine molecules located on general positions, and the metal cation on a centre of inversion. By considering the H-bonds between the sulphur atom and the 4-methoxypyridine-related hydrogen atom (S···H-C distance: 2.884 Å, S-H-C angle: 161.02°), the complexes are arranged into chains running along the diagonals of the *ab*-plane (along [110] and [1$\bar{1}$0] directions, alternately). These chains are connected by weak interactions, most likely hydrogen bonds, between the 4-methoxypyridine ligands (Figure 7.2).

Compound **Cd-II**, a polymorphic form of **Cd-I**, crystallizes in the non-

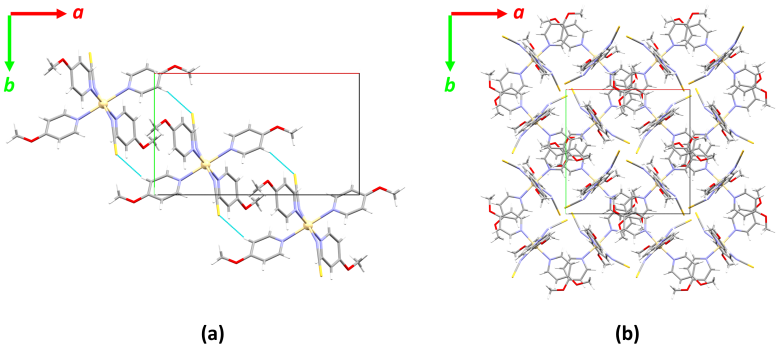

Figure 7.2. View along the *c*-axis of the chain-like structural motif formed by hydrogen bonds (light blue) along the diagonal of the *ab*-plane in **Cd-I** (a) and projection of the crystal structure along the *c*-axis in **Cd-II** (b).

centrosymmetric tetragonal space group $P4_1$ (a = 13.9707(2) Å, c = 15.6984(2) Å and V = 3064.02(6) Å^3, Table 7.1). The asymmetric unit consists of one metal cation, two thiocyanate molecules and four 4-methoxypyridine molecules located on general positions. The crystal structure exhibits an arrangement different from the previous compound. Indeed, as a consequence of the four-fold screw axis, the complexes are stacked along the *c*-axis leading to a helical arrangement (Figure 7.2).

7.2.2 Iron thiocyanate coordination complexes

Synthetic studies in solution and in solid state of Fe(II) thiocyanate compounds with 4-picoline led to the identification of several new coordination complexes. Before these studies, only two crystal structures based on 4-picoline as co-ligand with the chemical compositions $[4\text{-picolineH}]_2^{2+}$ $[Fe(NCS)_2(4\text{-picoline})_4]^{2-}$ and $[Fe(NCS)_2(4\text{-picoline})_4 \cdot 4\text{-picoline}]$ were reported in literature [188, 189].

In aqueous solution, two new crystalline compounds were synthesised. One compound (porous $Fe(NCS)_2(4\text{-picoline})_4 \cdot$solvate, **0-Fe**) was characterized by SC-XRD, whe-reas for the other one (**1-Fe**), no single crystals were obtained. The elemental analysis of **1-Fe** suggested a chemical composition $Fe(NCS)_2(H_2O)_2(4\text{-picoline})_2$ but it was not possible to extract any information about the coordination mode of the thiocyanate ligands from IR and Raman spectroscopy. *Ab initio* structure solution from XRPD revealed that this compound crystallizes in the monoclinic space group $P2_1/c$ (a = 10.2833(6) Å, b = 12.3146(6) Å, c = 7.6860(3) Å, β = 103.823(4)° and V = 945.12(8) Å^3, Table 7.2). The metal cation is located on a centre of inversion and octahedrally coordinated by two thiocyanates, two water molecules and two 4-picoline ligands. The different complexes are mainly connected by H-bonds between thiocyanate and 4-picoline (S···H-C distance: 2.856 Å, S-H-C angle: 164.75°) giving a chain-like structural motif running along the [101] direction (minor diagonal of the *ac*-plane). Weak H-bonds between thiocyanate and water molecules (S···O distance: 3.227 Å) allow the different chain motifs to interact with each other along the crystallographic *c*-axis (Figure 7.3, a).

To investigate new 4-picoline deficient crystalline phases, controlled thermal decomposition of **0-Fe** and **1-Fe** compounds was performed using combined TGA/DSC measurements. The TG-curves shows distinct mass losses related to the presence of at least two new compounds (Figure 7.4). The first weight loss is associated with the removal of two 4-picoline ligands for **0-Fe** (Δm_{calc}=34.2 wt-%, Δm_{exp}=35.1 wt-%, Figure 7.4, (1a)) and two water

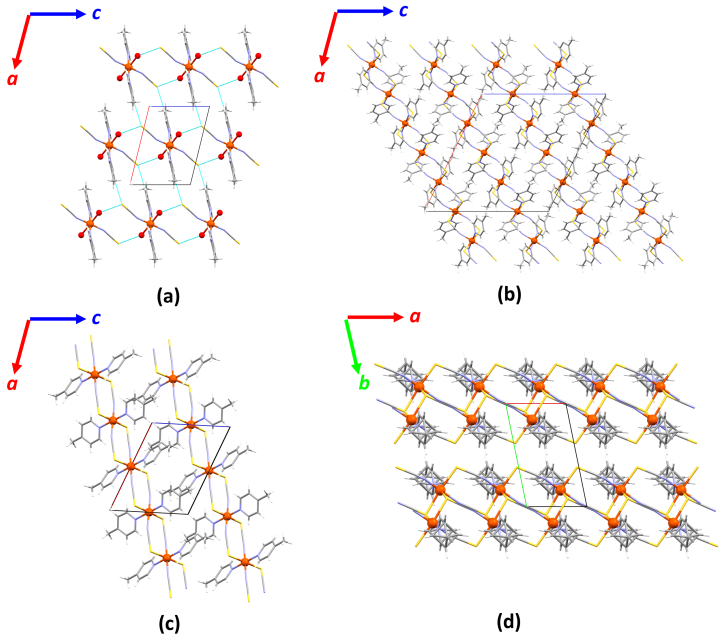

Figure 7.3. View of the structural features of **1-Fe** (a), **2-Fe-I** (b), **2-Fe-II** (c) along the *b*-axis, and **3-Fe** along the *c*-axis (d).

molecules for **1-Fe** ($\Delta m_{calc.}$=9.1 wt-%, Δm_{exp}= 8.8 wt-%, Figure 7.4, (1b)). The second step shows a weight loss of 15.7 wt-% for **0-Fe** (Δm_{calc}=17.1 wt-%, Figure 7.4, (2a)) and 24.4 wt-% for **1-Fe** (Δm_{calc}=23.6 wt-%, Figure 7.4, (2b)) and corresponds to the removal of one 4-picoline molecule. The last weight loss corresponds to the removal of the last 4-picoline molecule and the formation of $Fe(NCS)_2$ (Δm_{exp}=14.1 wt-%, Figure 7.4, (3a) and Δm_{exp}=22.5 wt-%, Figure 7.4, (3b)).

Additional TG measurements were carried out with the aim to selectively obtain the phases after each mass loss step and characterize them with *ex situ* XRPD. Surprisingly, three new 4-picoline deficient coordination complexes, two polymorphs $Fe(NCS)_2(4\text{-picoline})_2$ (**2-Fe-I** and **2-Fe-II**) and $Fe(NCS)_2$(4-picoline) (**3-Fe**), were identified during this process.

2-Fe-I, synthesised by controlled thermal decomposition at 75 °C for

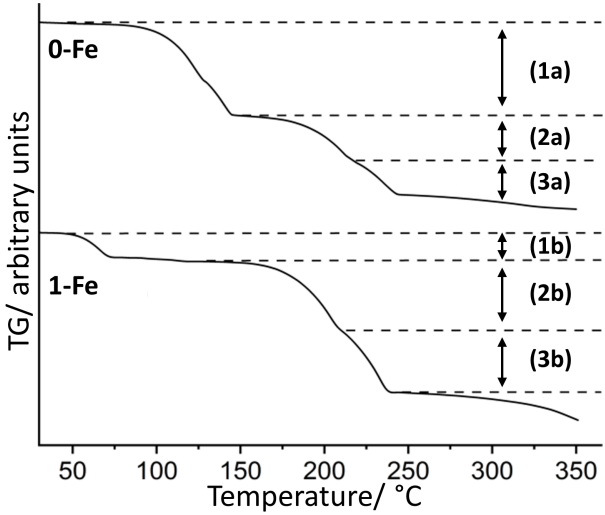

Figure 7.4. TG curves of **0-Fe** (top) and **1-Fe** (bottom) measured at heating rate of 1 °C/min in dynamic nitrogen atmosphere. Adapted from [166].

more than 43 hours, was found to be isotypic to a previously reported complex based on cadmium [190, 191] and crystallizes in the monoclinic space group $C2/c$ (a = 20.2576(8) Å, b = 9.3191(3) Å, c = 19.2831(6) Å, β = 116.135(2) ° and V = 3268.1(2) Å^3, Table 7.2). The asymmetric unit consists of two crystallographically independent metal cations octahedrally coordinated by two 4-picoline and four thiocyanate ligands. One metal site shows the 4-picoline ligands and two thiocyanate ions in *cis*-position whereas on the other metal site, they are in *trans*-position. Interestingly, the thiocyanate ligands bridge the metal centres forming chains running along a direction almost parallel to the minor diagonal of the *ac*-plane (Figure 7.3, b).

2-Fe-II was initially synthesised by controlled thermal decomposition at a temperature slightly below 70 °C for around 1 hour. It was observed that this compound transforms into **2-Fe-I** upon extended heating at high temperature. Rietveld refinement, using the previously reported crystal structure of $[Cu(NCS)_2(4\text{-cyano-pyridine})_2]_n$ [192] as model, reveals that **2-Fe-II** is a polymorphic form of **2-Fe-I** and crystallizes in the monoclinic space group

$P2_1/c$ (a = 11.2197(16) Å, b = 17.949(2) Å, c = 9.0538(12) Å, β = 112.712(7)° and V = 1681.9(4) Å^3, Table 7.2). In contrast to **2-Fe-I**, all ligands, coordinated to the two crystallographically independent iron atoms, are in *trans*-position. As a consequence, the metals are linked by bridging thiocyanate ions in linear chains running along the minor diagonal of the *ac*-plane (the [101] direction, Figure 7.3, c).

3-Fe, the most 4-picoline deficient structure, was found to be isotypic to

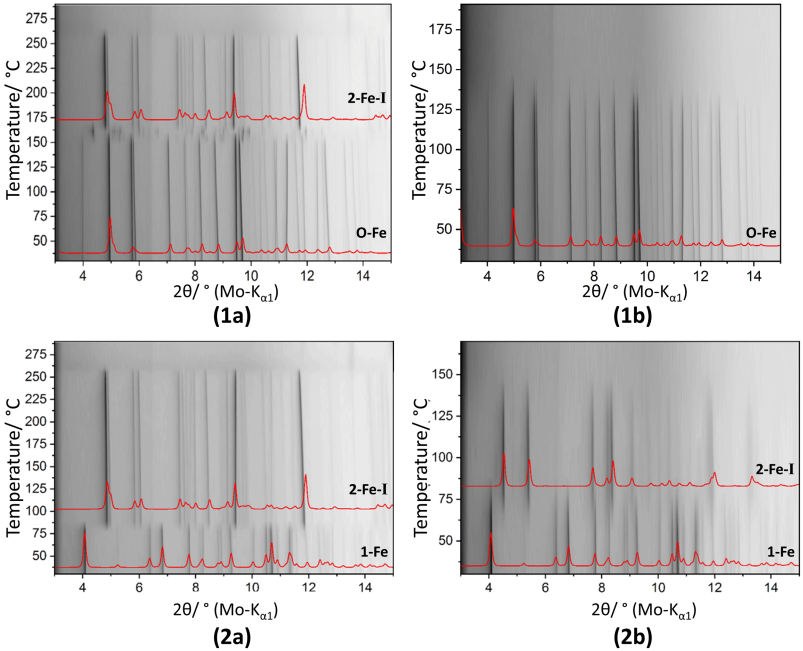

Figure 7.5. Temperature dependent *in situ* XRPD measurements of **0-Fe** in a sealed (**1a**) and in an open capillary (**1b**), and of **1-Fe** in a sealed (**2a**) and in an open capillary (**2b**). The calculated XRPD patterns of **0-Fe**, **1-Fe**, **2-Fe-I**, and **2-Fe-II** are given in red. Adapted from [166].

the cadmium-related compound, which was previously characterized by Neumann from the research group of Prof. Näther during this project and used as model for the Rietveld analysis of the iron complex. The iron compound crystallizes in the triclinic space group $P\bar{1}$ (a = 5.6544(4) Å, b = 10.3052(8)

Table 7.2. Crystallographic and Rietveld refinement data of compounds **1-Fe**, **2-Fe-I**, **2-Fe-II** and **3-Fe**.

Compound	**1-Fe**	**2-Fe-I**	**2-Fe-II**	**3-Fe**
Crystal system	Monoclinic	Monoclinic	Monoclinic	Triclinic
Space group (No.)	$P2_1/c$ (14)	$C2/c$ (15)	$P2_1/c$ (14)	$P\bar{1}$ (1)
Wavelength/ Å	0.7093	0.7093	0.7093	0.7093
a/ Å	10.2833(6)	20.2576(8)	11.2197(16)	5.6544(4)
b/ Å	12.3146(6)	9.3191(3)	17.949(2)	10.3052(8)
c/ Å	7.6860(3)	19.2831(6)	9.0538(12)	10.4498(7)
α/ °	90	90	90	70.083(5)
β/ °	103.823(4)	116.135(2)	112.712(7)	78.969(7)
γ/ °	90	90	90	75.518(4)
V/ Å^3	945.12(8)	3268.1(2)	1681.9(4)	550.52(7)
Z	2	8	4	2
T/ K	298	298	298	298
Refined parameters	40	59	50	55
D_{calc}/ g·cm^{-3}	1.371	1.456	1.415	1.581
R_{wp}/ % [a]	3.82	2.23	2.44	3.12
R_p/ % [a]	2.97	1.68	1.91	2.50
R_{Bragg}/ % [a]	2.18	0.98	0.68	1.46
Starting angle measured/° 2θ	2	2	2	2
Final angle measured/° 2θ	50	50	50	50
Starting angle used/° 2θ	2	2	2	2
Final angle used/° 2θ	40	40	30	40
Step width/° 2θ	0.015	0.015	0.015	0.015

[a] As defined in section 2.2.3.

Å, *c* = 10.4498(7) Å, α = 70.083(5)°, β = 78.969(7)°, γ = 75.518(4)° and *V* = 550.52(7) Å^3, Table 7.2). In the unit cell, the iron centre is octahedrally coordinated by one 4-picoline and five thiocyanate ligands with all atoms on general positions. The cations are linked by pairs of bridging thiocyanates into linear chains running along the *a*-axis (Figure 7.3). It should be noted that this structural motif is very rare and only few examples, mostly with cadmium cations and only one with a less chalcolphilic metal (nickel), are reported in literature [181, 193, 194].

The phase transitions and the formation of the 4-picoline deficient com-

pounds were investigated in detail by performing temperature dependent *in situ* XRPD measurements on **0-Fe** and **1-Fe**. Interestingly, the measurements revealed two different thermal behaviours of the iron compounds when heated in an open or a sealed capillary. Indeed, when **0-Fe** is heated in an open capillary, it decomposes at circa 130 °C without showing any phase transition to a crystalline compound whereas if the measurement is repeated in a sealed capillary, the porous compound transforms into **2-Fe-I** through a crystalline unknown compound (Figure 7.5, 1). When **1-Fe** is heated in a sealed capillary, it behaves like **0-Fe** by undergoing a transition into **2-Fe-I**. However, when the measurement is repeated in an open capillary, the other polymorph, **2-Fe-II**, is obtained (Figure 7.5, 2). Surprisingly, the transition from **2-Fe-II** to **2-Fe-I**. as well as the formation of **3-Fe** were not observed during TG measurements, as shown by *ex situ* XRPD. This may be due to the different sample environment (quartz capillary versus Al_2O_3 crucible), atmospheres (static air versus continuous nitrogen flow) and heating program.

7.2.3 Nickel thiocyanate coordination complexes

Reaction of nickel(II) thiocyanate with 3-ethylpyridine in different solvents led to the crystallization of two known discrete coordination complexes with formula $Ni(NCS)_2(3\text{-ethylpyridine})_4$ (two polymorphs, **1-I** and **1-II**), already reported in literature [195], and many new compounds, among them $Ni(NCS)_2(3\text{-ethylpyridine})_2(H_2O)_2$ (**2**, a discrete octahedral aqua complex) and $Ni(NCS)_2(3\text{-ethylpyridine})_2$ (two polymorphs, **3-I** and **3-Ic**), having cations linked by bridging thiocyanates into chains.

Our investigations on new 3-ethylpyridine deficient complexes and new solvent-free synthetic routes were carried out through controlled thermal ligand removal using coupled TGA/DTA. Analysis of the TG and DTA curves of **1-I** and **1-II** revealed that they possess the same thermal behaviour (Figure 7.6). In the DTA curve of **1-I**, an endothermic peak can be observed at 98 °C. This feature, which is not associated with any mass loss in the TG curve, can be attributed to the formation of a new polymorph ((0) inFigure 7.6,a).

Further heating of the sample up to 300 °C leads to three well resolved mass loss steps as shown in the DTG curve, which are associated with endothermic events in the DSC curve at 152 °C, 184 °C and 211 °C, respectively. The first step shows a weight loss of 35.4 wt-%, which corresponds to the removal of two 3-ethylpyridine ligands (Δ_{calc}=35.5 wt-%, (1) in Figure 7.6,a) and the formation of a complex with the formula $Ni(NCS)_2(3\text{-ethylpyridine})_2$ (**3-I**, **3-Ic** or a mixture of them). The second and third steps correspond to the removal of one ligand each (Δ_{calc}=17.8 wt-%, Δ_{exp}=18.1 wt-%, (2) in Figure 7.6,a and Δ_{exp}=18.0 wt-%, (3) in Figure 7.6,a) and the subsequent formation of a new 3-ethylpyridine deficient complex with formula $Ni(NCS)_2(3\text{-ethylpyridine})$ and lastly transforms to $Ni(NCS)_2$.

Temperature dependent *in situ* XRPD measurements were performed on

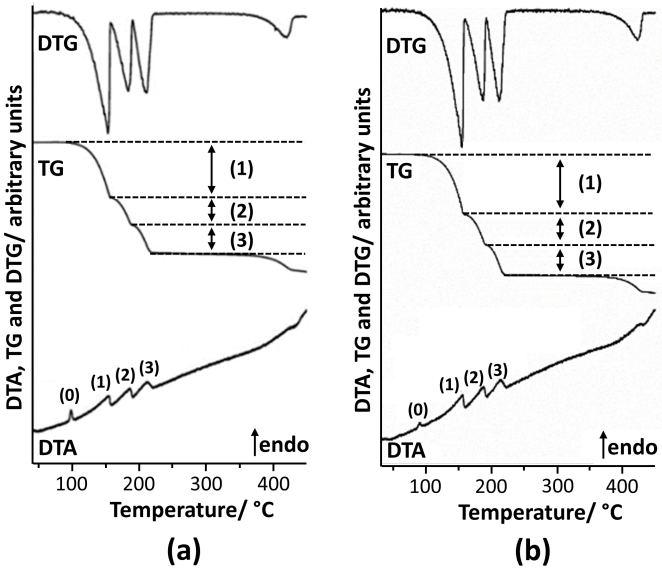

Figure 7.6. DTG, TG and DTA curves for **1-I** (a) and **1-II** (b) measured with a heating rate of 1 °C/min under a dynamic nitrogen atmosphere. Adapted from [167].

1-I, **1-II**, **3-I** and **3-Ic** in order to extract structural information and further

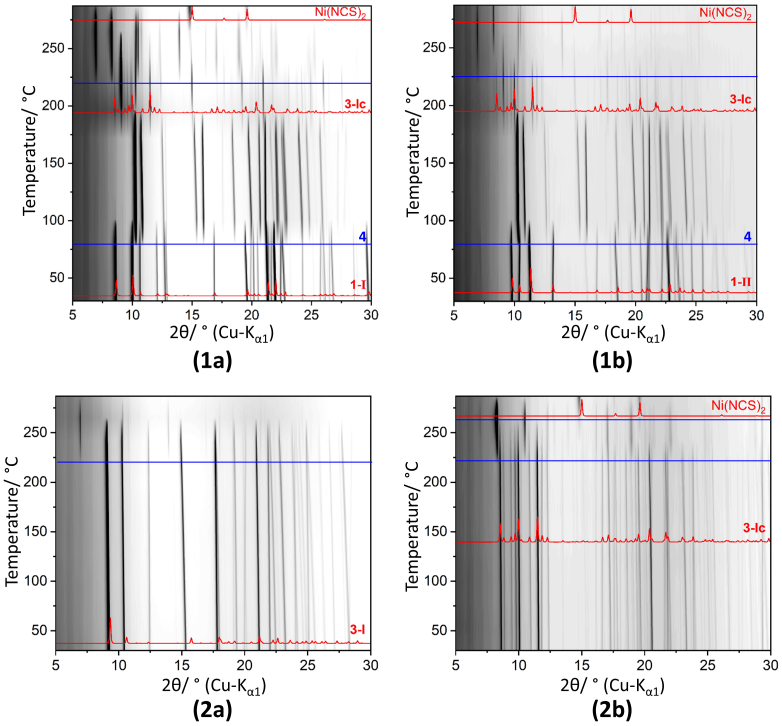

Figure 7.7. Temperature dependent *in situ* XRPD measurements of **1-I** (1a), **1-II** (1b), **3-I** (2a) and **3-Ic** (2b). The onsets of phase transformation are marked with a blue line. The calculated XRPD patterns of **1-I**, **1-II**, **3-I**, **3-Ic** and **Ni(NCS)$_2$** are given in red. Adapted from [167].

explore the formation of new 3-ethylpyridine deficient nickel complexes, as suggested by the thermal analysis. Measurements carried out on **1-I** and **1-II** showed the same thermal behaviour (Figure 7.7, 1a and 1b). Starting at about 80 °C, Bragg peaks corresponding to a new crystalline phase occurred. The temperature matches that of the endothermic peak in the DSC curve where no weight loss was observed. Therefore, a new crystalline polymorph of **1-I** and **1-II** formed (**4**). Then, the formation of a mixture containing the phase **3-Ic** and an unknown compound was observed at 160 °C. Further heating led to the formation of a new crystalline compound, most likely with the chem-

ical composition $Ni(NCS)_2$(3-ethylpyridine), followed by decomposition to crystalline $Ni(NCS)_2$. Investigation of the two polymorphs **3-I** and **3-Ic** led to two different results (Figure 7.7, 2a and 2b). The *in situ* measurements of the first polymorph showed a transition at around 225 °C leading to a different unknown crystalline compound followed by a decomposition to a non crystalline compound, most likely $Ni(NCS)_2$. Instead the second polymorph exhibits at around 225 °C the formation of a mixture of unknown compounds followed by the decomposition to $Ni(NCS)_2$. Unfortunately, given that in most of the cases, mixtures were observed, it has not been possible to determine the crystal structures of these new compounds for which even the indexing procedure of the XRPD patterns did not provide any reasonable solution. The only exception is observed for compound **4**, for which a unit cell and space group have been suggested (Table 7.3).

Table 7.3. Selected crystallographic information from the Pawley refinement for compound **4**.

Compound	**4**
Crystal system	Tetragonal
Space group (No.)	$I4_1/acd$ (142)
Wavelength/ Å	1.5406
a/ Å	16.0804(2)
c/ Å	25.7072(3)
V/ Å^3	6647.4(2)
T/ K	298
R_{wp}/ % [a]	1.27
R_p/ % [a]	0.97
Starting angle measured/° 2θ	2
Final angle measured/° 2θ	80
Starting angle used/° 2θ	6
Final angle used/° 2θ	70
Step width/° 2θ	0.015

[a] As defined in section 2.2.3.

7.2.4 Manganese thiocyanate coordination complexes

4-picoline-based coordination compounds

Investigation of new coordination complexes of manganese thiocyanate with 4-picoline (4-methylpyridine) in solution led to the synthesis of many crystalline forms with formula $[Mn(NCS)_2(4\text{-picoline})_4] \cdot 0.67(4\text{-picoline}) \cdot 0.33(H_2O)$ (**1-Mn**), $Mn(NCS)_2(4\text{-picoline})_2\ (H_2O)_2$ (**2-Mn-H_2O**) and $[Mn(NCS)_2(4\text{-picoline})_2]_2$ (**2-Mn-I**). For these crystalline compounds, single crystals suitable for SC-XRD analysis were obtained by the research group of Prof. Näther.

The crystal structure of **1-Mn** was already reported in literature [196] and it consists of discrete complexes with terminally coordinated thiocyanate anions, and solvent located in channels. Compound **2-Mn-H_2O** is isotypic to **0-Fe** (see section 6.2.2). Contrary to **1-Mn**, the crystal structure of **2-Mn-H_2O** does not show any channels filled with solvent molecules but discrete complexes where two crystallographically independent manganese atoms are located on a inversion centre and coordinated by two terminally N-bonded thiocyanate anions, two 4-picoline and two water molecules. Crystal structure of **2-Mn-I**, isotypic to **2-Fe-I**, consists of two crystallographically independent metal ions, one located on a centre of symmetry and the other one on a 2-fold axis, that are octahedrally coordinated by two 4-picoline and four thiocyanate ions. In this case, the metals ions are linked by bridging thiocyanate ions in linear chains.

Combined TGA/DSC measurements were performed on **1-Mn** and **2-Mn-H_2O** in order to explore new 4-picoline deficient Mn complexes. For both compounds, three weight loss steps, accompanied with three endothermic peaks in the DSC curve, were observed (Figure 7.8). A first weight loss (38,7 wt-%) was observed for **1-Mn**, correlated to an endothermic peak at 130 °C in the DSC, corresponding to the removal of the solvate molecules and two 4-picoline ligands (Δ_{calc}= around 40.6 wt-%, (1) in Figure 7.8,a). The second and third steps showed two weight losses of 16.3 wt-% and 15.6 wt-% associated with two endothermic peaks at 205 °C and 240 °C in the

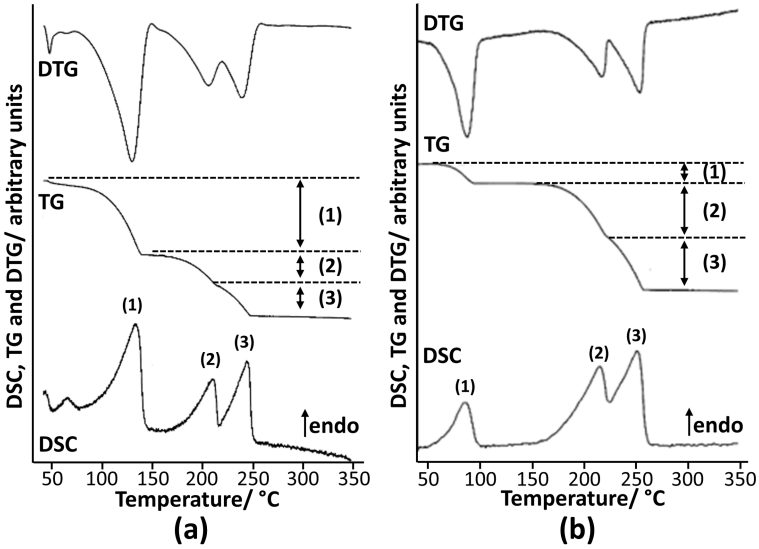

Figure 7.8. DTG, TG and DSC curves for **1-Mn** (a) and **2-Mn-H_2O** (b) measured with a heating rate of 4 °C/min under a dynamic nitrogen atmosphere. Adapted from [168].

DSC curve (Δ_{calc}= 15.2 wt-%, (2-3) in Figure 7.8,a). These two steps correspond to the removal of one co-ligand each, and to the subsequent formation of $Mn(NCS)_2(4\text{-picoline})_2$ (most likely **2-Mn-I**) and new compounds with formula $Mn(NCS)_2$(4-picoline), and $Mn(NCS)_2$. Similar discussion can be made for **2-Mn-H_2O**. The first step showed a mass loss of 7.6 wt-%, associated with an endothermic peak at 87 °C in the DSC curve, corresponding to the removal of two water molecules (Δ_{calc}= 9.2 wt-%, (1) in Figure 7.8,b). The second and third steps showed two weight losses of 22.8 wt-% and 24.2 wt-%, associated with two endothermic peaks at 215 °C and 251 °C in the DSC curve that correspond to the removal of one 4-picoline ligand each (Δ_{calc}= 23.6 wt-%, (2-3) in Figure 7.8,b).

Temperature dependent *in situ* XRPD measurements were performed on **1-Mn** and **2-Mn-H_2O** in order to investigate the existence of new crystalline polymorphs and 4-picoline deficient coordination complexes, as indicated by

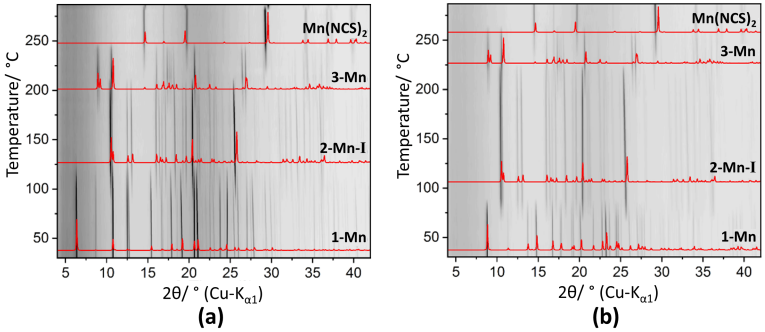

Figure 7.9. Temperature dependent *in situ* XRPD measurements of **1-Mn** (a) and **2-Mn-H_2O** (b). The calculated XRPD patterns of **1-Mn**, **2-Mn-H_2O**, **2-Mn-I**, **3-Mn** and **Mn(NCS)$_2$** are given in red. Adapted from [168].

the thermal analysis. Although the transition temperatures were quite different, the general thermal transformation mechanism for both compounds was found to be similar according to temperature dependent XRPD measurements (Figure 7.9). Upon heating **1-Mn** and **2-Mn-H_2O**, the transition to **2-Mn-I** was observed at around 90 °C and 70 °C, respectively. **2-Mn-I** further transformed to a new crystalline form (**3-Mn**) that decomposed to $Mn(NCS)_2$ above 220 °C. Surprisingly, no crystal structure for $Mn(NCS)_2$ was reported in literature.

To collect a high quality XRPD pattern of **3-Mn** for structure determination, the new 4-picoline deficient complex was synthesised *ex situ* via controlled thermal decomposition of **1-Mn** and **2-Mn-H_2O** in a thermobalance.

The crystal structure of **3-Mn**, isotypic to **3-Fe**, was refined by Rietveld refinement. The compound crystallizes in the triclinic space group $P\bar{1}$ (a = 5.7264(4) Å, b = 10.3512(4) Å, c = 10.521(4) Å, α = 70.867(3)°, β = 78.754(4)°, γ = 75.786(2)° and V = 568.29(4) Å^3, Table 7.4). The metal ions, located on general positions, are octahedrally coordinated by two N- and three S-bonding thiocyanate anions, and by one 4-picoline ligand. The refinement showed the presence of positional disorder for the picoline molecule, which in half of the cases is parallel and in the other half perpendicular to the *ac*-plane. Additionally, the manganese atoms are linked by μ-1,3 (N,S) and μ-

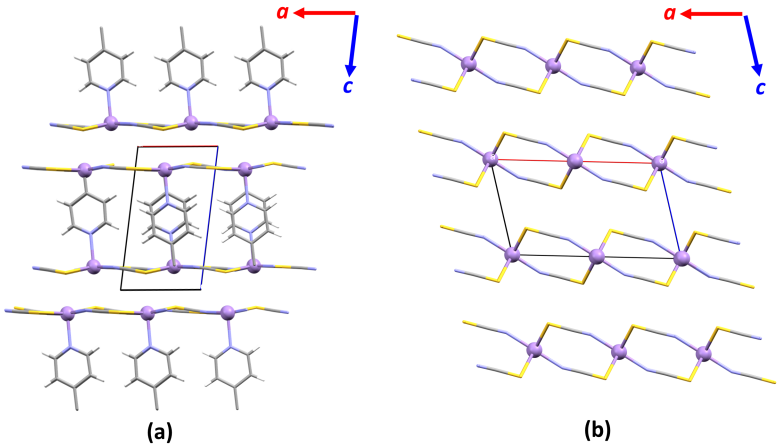

Figure 7.10. Projections of the crystal structures of **3-Mn** (a) and **Mn(NCS)$_2$** (b) with view along the *b*-axis.

1,3,3 (N,S,S) bridging thiocyanate ligands. As a consequence, a double chain running along the *a*-axis is formed (Figure 7.10, a).

By heating above circa 250 °C **1-Mn** and **2-Mn-H$_2$O**, temperature dependent *in situ* XRPD measurements revealed the formation of crystalline $Mn(NCS)_2$. As stated before, surprisingly, no crystal structure for $Mn(NCS)_2$ was reported neither in literature nor in databases like ICSD (by FIZ Karlsruhe) and CSD (by CCDC). The structure, isotypic to $Ni(NCS)_2$, was determined by Rietveld refinement and the compound crystallizes in the monoclinic space group *C*2/*m* (a = 10.7918(5) Å, b = 3.9104(2) Å, c = 6.2309(4) Å, β = 104.267(3)° and V = 254.84(3) Å^3, Table 7.4). The asymmetric unit consists of a metal ions located on an inversion centre and one thiocyanate ligand on a mirror plane. The metal cation is octahedrally coordinated by four thiocyanate-related sulphur atoms on the equatorial plane and two thiocyanate-related nitrogen atoms on axial sites. The sulphur atoms are shared by the metal ions and they form chains running along the *b*-axis. These chains are connected with each other through the μ-1,3,3 (N,S,S) bridging ligand forming layers parallel to the *ab*-plane and stacked along the crystallographic *c*-axis (Figure 7.10, b).

Table 7.4. Crystallographic and Rietveld refinement data of compounds **3-Mn** and **Mn(NCS)$_2$**.

Compound	**3-Mn**	**Mn(NCS)$_2$**
Crystal system	Triclinic	Monoclinic
Space group (No.)	$P\bar{1}$ (2)	$C2/m$ (12)
Wavelength/ Å	0.7093	0.7093
a/ Å	5.7264(2)	10.7918(5)
b/ Å	10.3512(4)	3.9104(2)
c/ Å	10.512(4)	6.2309(4)
α/ °	70.867(3)	90
β/ °	78.754(4)	104.267(3)
γ/ °	75.786(2)	90
V/ Å^3	568.29(4)	254.84(3)
T/ K	298	298
Refined parameters	83	37
D_{calc}/ g·cm^{-3}	1.526	2.230
R_{wp}/ % [a]	2.80	3.98
R_p/ % [a]	2.15	2.70
R_{Bragg}/ % [a]	1.46	1.68
Starting angle measured/° 2θ	2	2
Final angle measured/° 2θ	50	55
Starting angle used/° 2θ	2	2
Final angle used/° 2θ	40	40
Step width/° 2θ	0.015	0.015

[a] As defined in section 2.2.3.

4-cyanopyridine-based coordination compounds

Synthetic studies of new coordination complexes of manganese thiocyanate were performed using 4-cyanopyridine (CNpy) as co-ligand. This co-ligand was chosen because, contrary to the 4-picoline, it does not only act as a terminal ligand through the ring-related nitrogen atom but it also acts as bridging ligand through the cyano group. Therefore, a different thermal behaviour compared to the 4-picoline coordination compounds is expected, such as the formation of 2D/3D coordination polymers.

Synthesis conducted in solution yielded new coordination compounds, some of which with formula $Mn(NCS)_2(CNpy)_4$ (**1-MnCN**), $Mn(NCS)_2\ (H_2O)_2\ (CNpy)_2$ (**2-MnCN**), [Mn $(NCS)_2(H_2O)_2(CNpy)_2$]·4(CNpy) (**3-MnCN**), [Mn

$(NCS)_2(CNpy)_2]_n$ (**4-MnCN**) and [Mn $(NCS)_2(CNpy)]_n$ (two polymorphic forms, **5-MnCN-I** and **5-MnCN-II**). Compounds **3-MnCN**, **4-MnCN** and **5-MnCN-I** were obtained as single crystals and characterized through SC-XRD by the research group of Prof. Näther. The crystal structure of **3-MnCN** shows discrete complexes, having the metal ions octahedrally coordinated by two thiocyanate atoms, two CNpy, and two water molecules ligands, linked to non-coordinated CNpy ligands via hydrogen bonds. In compound **4-MnCN**, the metal atoms are octahedrally coordinated by four thiocyanate and two CNpy and they are linked into chains by pairs of μ-1,3-bridging thiocyanate ligands. In the crystal structure of **5-MnCN-I**, the coordination of the manganese atoms is similar to that in **4-MnCN**. However, μ-1,3-bridging thiocyanate ligands bridge the metal ions by forming layers, which are connected by bridging CNpy molecules to give a 3D network.

For **1-MnCN**, **2-MnCN**, and **5-MnCN-II**, no single crystals could be grown and therefore, structural information was obtained through XRPD analysis. Elemental analysis and IR spectroscopy were first applied to extract structural information including the empirical formula and the coordination environment of the 4-cyanopyridine ligands. Compound **1-MnCN** crystallizes in the monoclinic space group $P2_1/c$ (a = 7.9069 (2) Å, b = 11.6319(3) Å, c = 15.7392(5) Å, β = 94.4352(18)° and V = 1443.24(7) Å^3, Table 7.5). The crystal structure shows the metal ions, located on a centre of inversion, octahedrally coordinated by two terminal N-bonded thiocyanate ligands and four CNpy ligands through the pyridine-related nitrogen atoms (Figure 7.11, a). Compound **2-MnCN** crystallizes in the monoclinic space group $P2_1/c$ (a = 10.8842(5) Å, b = 12.4527(6) Å, c = 7.5244(2) Å, β = 104.966(3)° and V = 985.25(7) Å^3, Table 7.5). In this crystal structure (Figure 7.11, b), the manganese atoms are located on a centre of inversion and they are octahedrally coordinated by two water molecules, two thiocyanate and two CNpy ligands. The thiocyanate and CNpy act as terminal ligands and they are bonded to the metal ions via nitrogen atoms as in **1-MnCN**. The discrete complexes are connected to each other along the c-axis through hydrogen bonds between the water molecules and thiocyanate ligands (O···S distance: 3.225 Å). Along

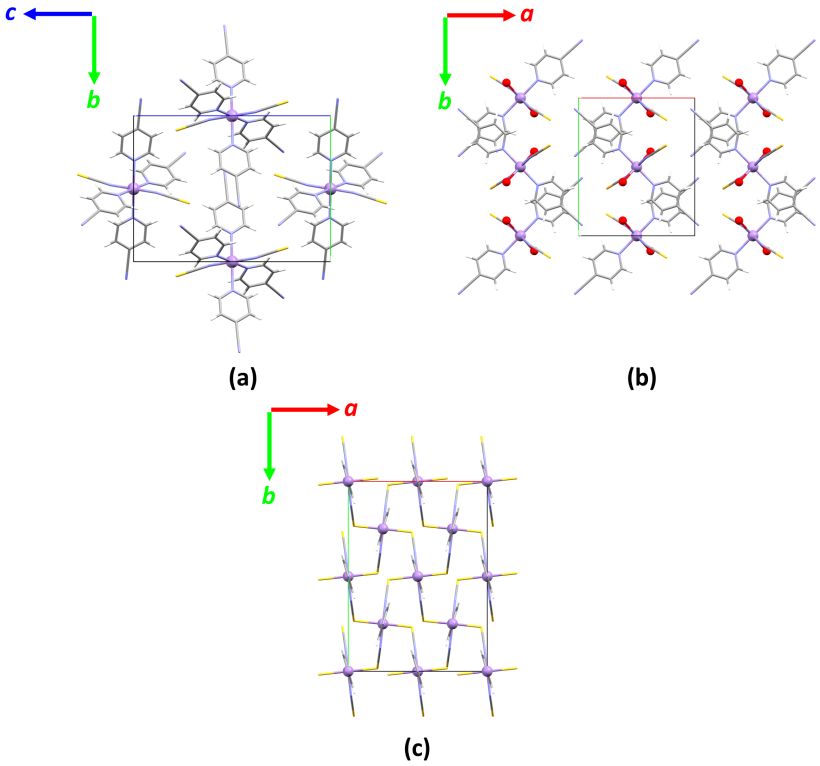

Figure 7.11. Projections of the crystal structures of **1-MnCN** along the *a*-axis (a), and of **2-MnCN** (b) and **5-MnCN-I** (c) along the *c*-axis.

the *c*-axis, the CNpy ligands are stacked into columns indicating possible $\pi\cdots\pi$ interactions (shortest distance between aromatic rings: 3.3822 Å, distance between aromatic ring centroids: 3.914 Å). Compound **5-MnCN-II** crystallizes in the orthorhombic space group *Fdd*2 (a = 12.65419(2) Å, b = 17.2815(2) Å, c = 9.8179(1) Å and V = 2146.99(4) Å^3, Table 7.5). The crystal structure (Figure 7.11, c) shows metal ions octahedrally surrounded by four thiocyanate ligands and two CNpy molecules. Interestingly, contrary to the previous compounds, the CNpy ligands, located on a 2-fold axis, connect the metal cations into chains along the *c*-axis by using the cyano group as well. Additionally, the metals are also linked by μ-1,3-bridging thiocyanate ligands

giving rise to a 3D network, which is rare for metal thiocyanate coordination complexes and has to the best of our knowledge just been observed once so far [197].

TG analysis was performed on compounds **1-MnCN**, **2-MnCN**, **3-MnCN**, and **4-MnCN** in order to reveal hints for possible structural relationships among the characterized compounds or the formation of new cyanopyridine-deficient coordination complexes. In all the cases, the analysis of the TG curves reveals the presence of several mass losses (Figure 7.12). In particular, the TG curve of **1-MnCN** shows three mass losses corresponding to the removal of two CNpy ligands in one step (Δ_{calc}= 35.4 wt-%, Δ_{exp}= 35.0 wt-%, Figure 7.12, (1a)) followed by the removal of one CNpy ligand per step

Table 7.5. Crystallographic and Rietveld refinement data of compounds **1-MnCN**, **2-MnCN** and **5-MnCN-II**.

Compound	**1-MnCN**	**2-MnCN**	**5-MnCN-II**
Crystal system	Monoclinic	Monoclinic	Orthorhombic
Space group (No.)	$P2_1/c$ (14)	$P2_1/c$ (14)	$Fdd2$ (43)
Wavelength/ Å	0.7093	0.7093	1.5406
a/ Å	7.9069(2)	10.8842(5)	12.65419(2)
b/ Å	11.6319(3)	12.4527(6)	17.2815(2)
c/ Å	15.7392(5)	7.5244(2)	9.8179(1)
α/ °	90	90	90
β/ °	94.4352(18)	104.966(3)	90
γ/ °	90	90	90
V/ Å^3	1443.24(7)	985.25(7)	2146.99(4)
T/ K	298	298	298
Refined parameters	44	52	44
D_{calc}/ g·cm^{-3}	1.352	1.387	1.703
R_{wp}/ % [a]	3.20	3.69	2.75
R_p/ % [a]	2.34	2.68	1.95
R_{Bragg}/ % [a]	1.63	1.70	2.88
Starting angle measured/° 2θ	0	0	3
Final angle measured/° 2θ	50	50	80
Starting angle used/° 2θ	3	3	3
Final angle used/° 2θ	40	40	80
Step width/° 2θ	0.015	0.015	0.015

[a] As defined in section 2.2.3.

(Δ_{exp}= 18.4 wt-% and 17.4 wt-%, Figure 7.12, (2a-3a)). The TG curve of

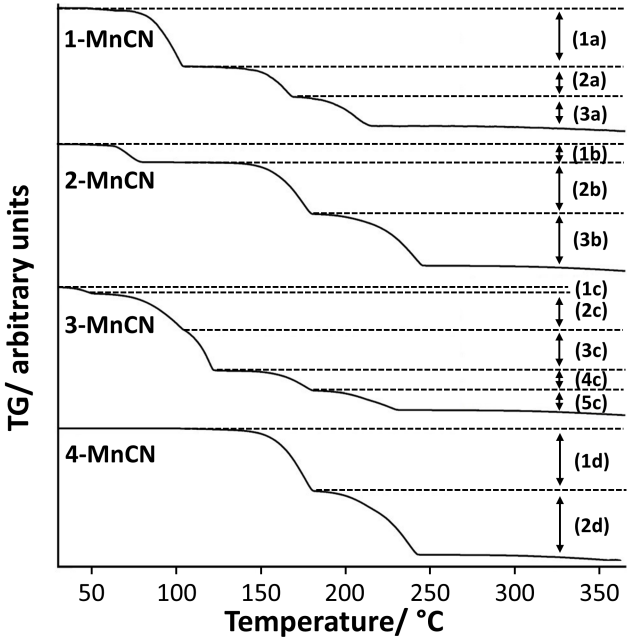

Figure 7.12. From top to bottom: TG curves for **1-MnCN**, **2-MnCN**, **3-MnCN**, and **4-MnCN** measured under a dynamic nitrogen atmosphere. Adapted from [169].

the hydrated compound **2-MnCN** shows three mass losses corresponding to the removal of two water molecules in one step (Δ_{calc}= 8.7 wt-%, Δ_{exp}= 9.0 wt-%, Figure 7.12, (1b)) and two CNpy ligands (Δ_{exp1}= 25.0 wt-%, Δ_{exp2}= 25.0 wt-%, Figure 7.12, (2b-3b)). The TG curve of the solvated compound **3-MnCN** reveals five mass losses. The first one (Δ_{exp}= 4.6 wt-%, Figure 7.12, (1c)) corresponds to the removal of two water molecules (Δ_{calc}= 4.3 wt-%), the second and third one (Δ_{exp}= 22.9 wt-% and 27.8 wt-%, Figure 7.12, (2c-3c)) to the removal of the two noncoordinated CNpy co-ligands each, whereas the fourth and fifth steps (Δ_{exp}= 22.9 wt-% and 27.8 wt-%, Figure 7.12, (4c-5c)) to the removal of one coordinated CNpy coligand each Δ_{calc}= 12.5 wt-%). These results reveal the possibility of transitions from crystalline

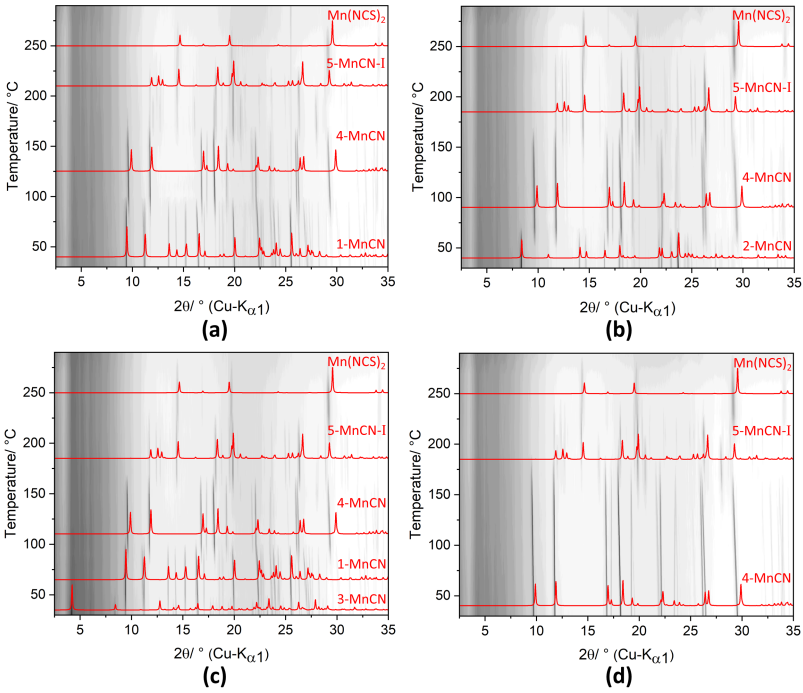

Figure 7.13. Temperature dependent *in situ* XRPD measurements of **1-MnCN** (a), **2-MnCN** (b), **3-MnCN** (c) and **4-MnCN** (d). The calculated XRPD patterns of **1-MnCN**, **2-MnCN**, **3-MnCN**, **4-MnCN**, **5-MnCN-I** and **$Mn(NCS)_2$** are given in red. Since the crystal structures used to calculate the XRPD patterns were determined at low temperatures, differences in peak positions can be observed. Adapted from [169].

CNpy- and/or water-rich- to CNpy-deficient manganese thyocyanate coordination compounds. To demonstrate the existence of these structural changes, temperature-dependent *in situ* XRPD measurements were performed on the same compounds previously investigated through TG analysis. The *in situ* measurements of **1-MnCN** and **2-MnCN** show the same thermal behaviour with the exception of the transition temperatures. Both compounds transform first to the CNpy-deficient complex **4-MnCN** and then to **5-MnCN-I**. Upon further heating, Bragg peaks related to $Mn(NCS)_2$ were observed (Fig-

ure 7.13, a-b). *In situ* measurements on the solvated compound **3-MnCN** showed a direct transformation into **1-MnCN**. This was surprising, as a gradual release of the coordinating water, as well as 4-cyanopyridine with an intermediate phase was expected. However, both are simultaneously released, forming **1-MnCN**, which is stable up to about 100 °C. Upon further heating, it was observed the same thermal behaviour as just discussed for pure **1-MnCN** (Figure 7.13, c). Interestingly, none of these measurements show the formation of the second polymorph **5-MnCN-II**, whose crystalline powder was accidentally obtained in a time-resolved experiment from solution. Temperature-dependent *in situ* XRPD measurements of **4-MnCN** were performed to investigate whether a transition to the polymorph **5-MnCN-II** can be obtained. However, as in the previous measurements, only crystalline **5-MnCN-I** is formed, followed by decomposition into $Mn(NCS)_2$ (Figure 7.13, d).

7.3 Conclusions

In this chapter, a major contribution to the structure determination of new crystalline forms and to the development of new synthetic routes in the solid state of Cd(II), Fe(II), Ni(II), and Mn(II) thiocyanate coordination compounds has been given. In particular, *ab initio* structure determinations (via simulated annealing approach) and Rietveld refinements against laboratory XRPD data were performed to reveal the structural features of the metal coordination compounds obtained from solution and controlled thermal decomposition. In some cases, rare structural motifs (as in **3-Fe**) have been identified. Furthermore, temperature-dependent *in situ* XRPD measurements revealed structural relationships among the studied crystalline forms and the formation of new ones. This method, in combination with thermal analysis, contributed to the development of new solvent-free synthetic strategies to obtain previously unknown crystalline modifications in the solid, which in most of the cases are not possible via solution.

7.4 Experimental section

Samples

All the samples analysed in this project are synthesized and characterized (elemental analysis, IR spectroscopy, SC-XRD) by the research group of Prof. Näther according to the publications [165–169].

XRPD measurements

XRPD measurements for structure solution and Rietveld refinement of the investigated compounds were carried out at room temperature on two Stadi-P Diffractometers (Stoe) in Debye-Scherrer geometry with Cu-$K_{\alpha 1}$ and Mo-$K_{\alpha 1}$ radiation from primary Ge(111)-Johann-type monochromators and 3 Mythen 1K detectors (Dectris). The samples were loaded into 0.5 mm diameter boroglass capillaries (WJM-Glas/Mueller GmbH), which were spun during the measurement.

Temperature dependent *in situ* X-ray powder diffraction

Temperature dependent *in situ* XRPD measurements of the investigated samples were carried out on two Bruker D8-Advance powder diffractometers in Debye-Scherrer geometry with two different radiation sources. The former one has a Cu-$K_{\alpha 1}$ radiation from primary Ge(111)-Johannson-type monochromator and Våntec detector. The latter, a Mo-$K_{\alpha 1}$ radiation from primary Ge(220)-Johannson-type monochromator and LYNXEYE detector. The samples were loaded into 0.5 mm diameter quartz capillaries, which were spun during the measurements. The temperature was adjusted using a TC-transmission furnace (mri).

Indexing, space group determination, Pawley refinement, crystal structure solution through Simulated Annealing and Rietveld refinement were performed with the program TOPAS 6.0 [64].

8 Conclusions

The focus of this PhD thesis lies in the investigation of the crystal structures and the structural changes upon temperature and pressure of a variety of organic, organometallic, and inorganic compounds. These studies were carried out predominantly by using X-ray powder diffraction (XRPD), a well-established technique for identification, quantification, and structural characterization of microcrystalline materials. Furthermore, the pair distribution function (PDF), obtained from total scattering XRPD experiments, was used to confirm the crystal structure and extract additional information about crystalline and amorphous species. These tools were also employed to study reactions *in situ* in the solid state. In particular, *in situ* XRPD and PDF experiments were performed to monitor and elucidate the synthetic processes and the behaviour of materials while they are exposed to external *stimuli* such as temperature and pressure (*vacuum*). For this purpose, three reactors for *in situ* and *operando* XRPD studies were designed and built. The first two reactors, similar but different in capacity, were realized for studying synthetic processes of crystalline compounds in relative large-volume suspensions where heating, mixing, step-wise addition of reactants, and injection of inert gas are needed while temperature and pH must be monitored. The other reactor is a miniaturized autoclave, which was realized for studying synthetic processes where a sealed reaction chamber is indispensable, such for the hydrothermal synthesis of zeolites and MOFs. These reactors allow details of the crystallization processes of compounds in a liquid medium (*e.g.* suspensions) or in

the solid state to be revealed.

The results from each of the case studies presented in this thesis demonstrate clearly how XRPD alone or combined with PDF analysis are essential in retrieving atomistic details, reactions information, and properties of compounds, regardless of their class of materials and their degree of structural order.

In the third chapter, characterization and thermal behaviour studies demonstrate that the combination of XRPD with PDF, SEM, IR/Raman spectroscopy, and TGA/DTA, is powerful in elucidating the morphology, the crystal structure, and the thermal behaviour of an organic compound and an iron supplement coming from industries. This information can be used as a cornerstone for improving these materials, extracting storage and drying conditions but also as a reference for detecting fraud and abuse, such as product counterfeiting.

In the process of investigating multifunctional materials, the studies about anisotropic thermal expansion, included in the fourth chapter, showed how temperature-dependent *in situ* XRPD measurements are a crucial tool in elucidating this phenomenon. Structural changes were monitored and crystallographic parameters extracted. This information, together with an analysis of the crystal structure and the interatomic interactions, was used to explain the expansion in several crystalline organometallic materials, such as photosalient crystals and MOFs.

Furthermore, *in situ* experiments were used to study two synthetic approaches, solvent-free and solvent-based, for obtaining industrially important crystalline Chabazite zeolite. After designing the suitable reaction environment, crucial for these reaction systems, time-dependent *in situ* PDF and XRPD measurements at 190°C were carried out using either laboratory or synchrotron light sources. The crystallization process was followed by fast measurements, and the reactants and the product were monitored as function of time. PDF analysis confirmed the results obtained by reciprocal-space XRPD analysis, and in particular, allowed the amorphous reactants, present in the solvent-free approach, to be detected and quantified.

XRPD technique was also successfully applied to investigate the molecular and crystal structure of a polymer. Due to the comparatively high crystallinity of the compound, the crystal structure of poly(*p*-dinitrosobenzene), showing possible semiconducting properties, was determined *ab initio* through the simulated annealing approach. Thermal analysis and temperature-dependent *in situ* XRPD measurements confirmed the thermal stability up to 150°C.

The final part of the thesis, dedicated to a meticulous study of the thiocyanate coordination compounds of cadmium, iron, manganese, and nickel, evidenced how XRPD analysis was decisive in determining the crystal structures and the thermal behaviour of those compounds. In particular, crystal structures were determined by *ab initio* structure determination and Rietveld refinements using laboratory XRPD data, whereas new compounds were obtained *in situ*. Thanks to this contribution, a library of previously unknown thiocyanate coordination compounds was obtained, and new solvent-free strategies were developed allowing rare crystalline modifications to be synthesized and characterized.

In conclusion, these results showed that powder diffraction is still an underrated method with high potential for extracting structural information and atomic details from compounds at ambient condition or when they are subjected to external *stimuli* (*e.g.* temperature or pressure), regardless of the structural order (*e.g.* amorphous or crystalline) and medium (*e.g.* solid or liquid).

A Appendix

Giant anisotropic thermal expansion

Photosalient crystals

Table A.1. Crystallographic data extracted from SC-XRD for Cu(benzoate)(4spy)$_2$ (**1**), Cu(benzoate)(2F-4spy)$_2$ (**2**), and Cu(benzoate)(3F-4spy)$_2$ (**3**).

Compound	**1**	**2**	**3**
Crystal system	monoclinic	monoclinic	monoclinic
Space group	*C*2/*c*	*C*2/*c*	*C*2/*c*
a/ Å	24.633(11)	24.9699(8)	24.480(2)
b/ Å	12.093(4)	12.1074(4)	12.0004(9)
c/ Å	15.509(6)	15.4675(4)	15.598(1)
β/°	108.48(1)	108.809(1)	108.802(2)
V/ Å^3	4381(3)	4426.4(2)	4461.7(5)
Z	4	4	4
T/ K	100(2)	100(2)	100(2)
R_1	0.0335	0.0309	0.0278
wR_2	0.0821	0.0731	0.0738
GOF	1.030	1.025	1.126

Table A.2. Selected thermal expansion coefficients of the volume and along the principal axes from literature.

Compound	T range/ K	Axial TE, α_x/ $10^{-1}\cdot K^{-1}$	VTE, α_V/ $10^{-1}\cdot K^{-1}$	Ref.
Metal complexes				
PHA	220-350	260.4, 39.4, -79.9	247.8 (α form)	[110]
	100-270	124.0, 105.4, 114.9	255.5 (β form)	
$Cu(acac)_2$	100-300	42, 44, 70	213.15	[112]
$(Himd)_2[CuCl_4]$	273-353	-38, 568, -184	346	[28]
MOFs				
$Cu_3(btc)_2$	80-500		-4.1(1)	[198]
FMOF1*	295-90	230	300	[199]
MCF-82 **1***	112-300	61(1), 482(12), -218(3)	319(13)	[200]
1-DMF		171(4), 60(3), -56(2)	175(2)	[200]
1-DMA		85(1), 103(4), -51(3)	138(2)	[200]
$Ag_3[Co(CN)_6]$	10-500	150	160	[27]
Organics				
(S,S)-octa-3,5-diyn-2,7-diol*	225-330	$156<\alpha_a>516$, $-32<\alpha_b>-85$, $-48<\alpha_c>-204$		[30]
18-crown-6-nitromethane*	180-273	-129(15), 144(14), 282(16)	311	[99]
Organic salt				
imidazolium 4-hydrocybenzoate	100-360	-115, 18, 210	110	[201]
Co-crystals				
ABN:DMABN (1:2)	100-300	24.3, 90.9, 105	222	[202]
CBTA:BPE (1:2)	120-298	4(5), 25(4), 147(8)	183 (monoclinic)	[203]
4PAzP:(4,6-diCl res) (2:1)	290-260	-116, 29, 316	229	[204]
4PAzP:(4,6-diBr res) (2:1)	170-250	-2(4), 9(3), 172(6)	181(2)	[205]

*These materials do not show linear expansion during heating.

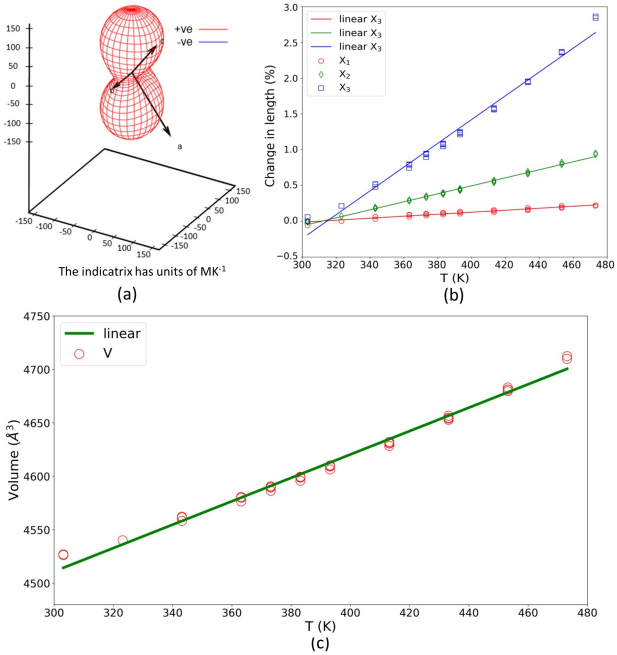

Figure A.1. Results from PASCal program for compound **1**: a) expansivity indicatrix (units: MK^{-1}), b) plot of the axes variations as function of the temperature and c) plot of the volume expansion as function of the temperature.

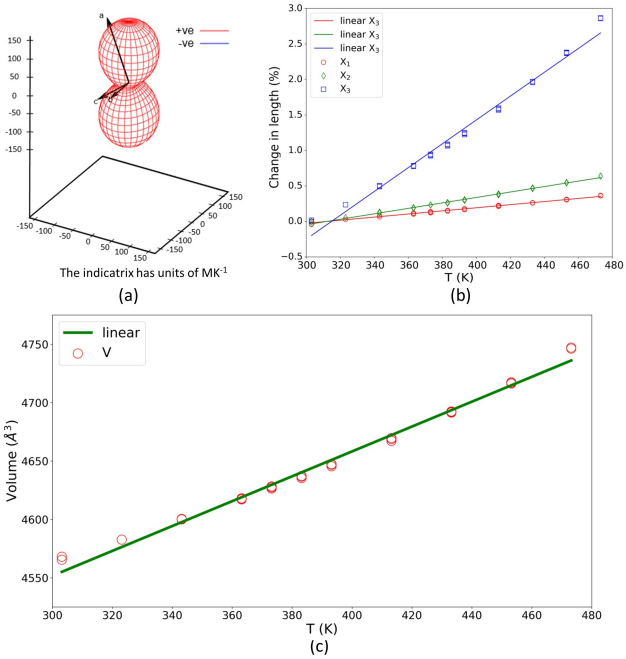

Figure A.2. Results from PASCal program for compound **2**: a) expansivity indicatrix (units: MK^{-1}), b) plot of the axes variations as function of the temperature and c) plot of the volume expansion as function of the temperature.

Interpenetrated Metal-Organic Framework

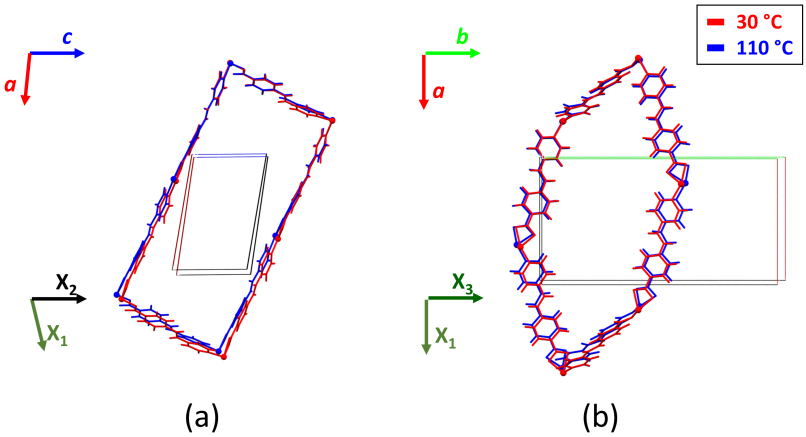

Figure A.3. Comparison between the rectangular motifs of **1** at 30°C (red) and 110°C (blue) along (a) *b*-axis and (b) *c*-axis showing PTE and NTE. The principal and crystallographic axes are also given.

B List of publications

15. G. Gallo, M. W. Terban, I. Moudrakovski, T. Huber, M. Ernst, B. Hinrichsen, and R. E. Dinnebier, "Crystal structure of a novel cyclic alkanolamine and molecular ranking using the pair distribution function", *close to submission*.

14. B. Notash, R. Farhadi, G. Gallo, and R. Dinnebier, "Humidity-Induced Structural Transformation in Pseudo-Polymorph Coordination Polymers", *in submission*.

13. G. Bolla, G. Gallo, I-H. Park, K. C. Kwon, X. Wu, Q-H. Xu, K. P. Loh, S. Chen, R. Dinnebier, W. Ji, and J.J. Vittal, "Multi-functional properties of a Zn(II) coordination complex", *in submission*.

12. B. Rath, G. Gallo, R. E. Dinnebier, and J. J. Vittal, "Reversible Thermosalience in a One-Dimensional Coordination Polymer Preceded by Anisotropic Thermal Expansion and Shape Memory Effect", *Journal of the American Chemical Society*, *accepted*.

11. G. Gallo, A. Mihanović, I. Rončević, R. E. Dinnebier, and H. Vančik, "Crystal structure and ON-OFF polymerization mechanism of Poly(1,4-phenyleneazine-*N*,*N*-di-oxide), a possible wide bandgap semiconductor", *POLYMER*, 2020.

10. I. Jess, T. Neumann, H. Terraschke, G. Gallo, R. Dinnebier, and C. Näther, "Synthesis, structures, thermal and luminescence properties

of Zn and Cd halide coordination polymers with 2-cyanopyrazine", *Zeitschrift für anorganische und allgemeine Chemie*, vol. 646, pp. 1046-1054, 2020.

9. C. Wellm, T. Neumann, G. Gallo, A. M. Dziubyna, M. Rams, R. E. Dinnebier, and C. Näther, "Structural variety in Mn $(NCS)_2$ 4-cyanopyridine coordination compounds: Synthesis, structures, isomerism, and magnetic properties", *Crystal Growth & Design*, vol. 20, no. 5, pp. 3374–3385, 2020.

8. T. Neumann, G. Gallo, R. E. Dinnebier, and C. Näther, "Synthesis, crystal structures, and properties of Mn $(NCS)_2$ coordination compounds with 4-picoline as coligand and crystal structure of Mn $(NCS)_2$", *Zeitschrift für anorganische und allgemeine Chemie*, vol. 646, no. 3, pp. 88–94, 2020.

7. Z. Chen, G. Gallo, V. A. Sawant, T. Zhang, M. Zhu, L. Liang, A. Chanthapally, G. Bolla, H. S. Quah, X. Liu, K. P. Loh, R. E. Dinnebier, Q.-H. Xu, and J. J. Vittal, "Giant enhancement of second harmonic generation accompanied by the structural transformation of 7-Fold to 8-Fold Interpenetrated Metal–Organic Frameworks (MOFs)", *Angewandte Chemie International Edition*, vol. 59, no. 2, pp. 833–838, 2020.

6. C. Wellm, T. Neumann, M. Ceglarska, G. Gallo, M. Rams, R. E. Dinnebier, and C. Näther, "New isomeric Ni$(NCS)_2$ coordination compounds: crystal structures, magnetic properties as well as ex situ and in situ investigations on their synthesis and transition behaviour", *CrystEngComm*, vol. 22, no. 13, pp. 2350–2360, 2020.

5. K. Yadava, G. Gallo, S. Bette, C. E. Mulijanto, D. P. Karothu, I.-H. Park, R. Medishetty, P. Naumov, R. E. Dinnebier, and J. J. Vittal, "Extraordinary anisotropic thermal expansion in photosalient crystals", *IUCrJ*, vol. 7, pp. 83–89, 2020.

4. T. Neumann, G. Gallo, I. Jess, R. E. Dinnebier, and C. Näther, "Thermodynamically stable and metastable coordination polymers synthesized from solution and the solid state", *CrystEngComm*, vol. 22, no. 2, pp. 184–194, 2020.

3. G. Gallo, S. Bette, and R. E. Dinnebier, "Characterization and thermal behavior of the iron dietary supplement ferrous glycine sulfate pentahydrate", *Zeitschrift für anorganische und allgemeine Chemie*, vol. 645, no. 24, pp. 1350–1357, 2019.

2. S. Glante, S. Bette, G. Gallo, R. E. Dinnebier, M. Hartmann, "Crystal structure and de-and rehydration behavior of two new chloride-containing Zeolitic Imidazolate Frameworks", *Crystal Growth & Design*, vol. 19, no. 8, pp. 4844-4853, 2019.

1. A. Jochim, G. Gallo, R. Dinnebier, and C. Näther, "Synthesis, crystal structure and properties of $Cd(NCS)_2$ coordination compounds with two different cd coordination modes", *Zeitschrift für Naturforschung B*, vol. 74, no. 1, pp. 49–58, 2019.

C Acknowledgement

Also this journey, full of new experiences and exciting results, has come to an end.
First of all, I would like to thank Bernd for believing in me from the very beginning and giving me the opportunity to do this PhD. This PhD would have not possible without the support of Robert who hosted me in his research group and was a valuable guiding figure and Prof. Tedesco who supported me during my whole academic career.
I kindly acknowledge BASF SE for financial support and for the possibilities I had during my traineeship and my PhD.
I thank all the people in industries and universities who have collaborated with me during these years, in particular Prof. Näther, Prof. Vittal, and their research groups, for having contributed to expand my knowledge in chemistry and materials characterization.
Special thanks to my colleagues, or rather, my friends, Giovanni, Luzia, Max, Sebastian, Christine, and Frank for helping me to improve myself, sharing moments of stress and joy, and being a constant source of inspiration during these three years.
I am grateful to my relatives and cousins in Böblingen for sharing some of the days during my stay in Germany.
Last but not least, I am grateful to my family for showing me the true value of work and Sara for teaching and helping me to work on myself. This PhD is mostly dedicated to them.

List of Figures

List of Tables

Bibliography

[1] J. Wright, C. Giacobbe, and M. Majkut, "New opportunities at the materials science beamline at esrf to exploit high energy nano-focus x-ray beams," *Current Opinion in Solid State and Materials Science*, p. 100818, 2020.

[2] M. L. Minus, H. G. Chae, and S. Kumar, "Observations on Solution Crystallization of Poly (vinyl alcohol) in the Presence of Single-Wall Carbon Nanotubes," *Macromolecular rapid communications*, vol. 31, no. 3, pp. 310–316, 2010.

[3] M. Ataka and M. Asai, "Systematic studies on the crystallization of lysozyme: Determination and use of phase diagrams," *Journal of Crystal Growth*, vol. 90, no. 1-3, pp. 86–93, 1988.

[4] R. E. Dinnebier and S. J. Billinge, "Principles of powder diffraction," *Powder Diffraction: Theory and Practice*, 2008.

[5] K. D. M. Harris and E. Y. Cheung, "How to determine structures when single crystals cannot be grown: opportunities for structure determination of molecular materials using powder diffraction data," *Chemical Society Reviews*, vol. 33, no. 8, pp. 526–538, 2004.

[6] B. L. Nannenga and T. Gonen, "The cryo-EM method microcrystal electron diffraction (MicroED)," *Nature methods*, vol. 16, no. 5, pp. 369–379, 2019.

[7] T. Gruene, J. T. Wennmacher, C. Zaubitzer, J. J. Holstein, J. Heidler, A. Fecteau-Lefebvre, S. De Carlo, E. Müller, K. N. Goldie, I. Regeni, *et al.*, "Rapid structure determination of microcrystalline molecular compounds using electron diffraction," *Angewandte Chemie International Edition*, vol. 57, no. 50, pp. 16313–16317, 2018.

[8] W. Liu, D. Wacker, C. Gati, G. W. Han, D. James, D. Wang, G. Nelson, U. Weierstall, V. Katritch, A. Barty, *et al.*, "Serial femtosecond crystallography of G protein-coupled receptors," *Science*, vol. 342, no. 6165, pp. 1521–1524, 2013.

[9] W. Friedrich, P. Knipping, M. v. Laue, and I.-E. bei Röntgenstrahlen, "Sitzungsberichte der königlich bayerischen akademie der wissenschaften," *Mathematisch–physikalische Klasse*, pp. 303–322, 1912.

[10] W. Friedrich, "Eine neue Interferenzerscheinung bei Röntgenstrahlen," *Physikalische Zeitschrift*, vol. 14, pp. 317–19, 1913.

[11] H. Rietveld, "A profile refinement method for nuclear and magnetic structures," *Journal of applied Crystallography*, vol. 2, no. 2, pp. 65–71, 1969.

[12] H. Rietveld, "Line profiles of neutron powder-diffraction peaks for structure refinement," *Acta Crystallographica*, vol. 22, no. 1, pp. 151–152, 1967.

[13] W. I. F. David and K. Shankland, "Structure determination from powder diffraction data," *Acta Crystallographica Section A*, vol. 64, no. 1, pp. 52–64, 2008.

[14] S. Bette, B. Hinrichsen, D. Pfister, and R. E. Dinnebier, "A routine for the determination of the microstructure of stacking-faulted nickel cobalt aluminium hydroxide precursors for lithium nickel cobalt aluminium oxide battery materials," *Journal of applied crystallography*, vol. 53, no. 1, 2020.

[15] W.-J. Yin, J.-H. Yang, J. Kang, Y. Yan, and S.-H. Wei, "Halide perovskite materials for solar cells: a theoretical review," *Journal of Materials Chemistry A*, vol. 3, no. 17, pp. 8926–8942, 2015.

[16] D. Hou, C. Zhao, A. R. Paterson, S. Li, and J. L. Jones, "Local structures of perovskite dielectrics and ferroelectrics via pair distribution function analyses," *Journal of the European Ceramic Society*, vol. 38, no. 4, pp. 971–987, 2018.

[17] D. H. Brouwer and G. D. Enright, "Probing Local Structure in Zeolite Frameworks : Ultrahigh-Field NMR Measurements and Accurate First-Principles Calculations of Zeolite ^{29}Si Magnetic Shielding Tensors," *Journal of the American Chemical Society*, vol. 130, no. 10, pp. 3095–3105, 2008.

[18] O. Q. De Clercq, L. I. Martin, K. Korthout, J. Kusakovskij, H. Vrielinck, and D. Poelman, "Probing the local structure of the near-infrared emitting persistent phosphor $LiGa_5O_8$:Cr^{3+}," *Journal of Materials Chemistry C*, vol. 5, no. 41, pp. 10861–10868, 2017.

[19] J. D. Smith, C. D. Cappa, B. M. Messer, W. S. Drisdell, R. C. Cohen, and R. J. Saykally, "Probing the Local Structure of Liquid Water by X-ray Absorption Spectroscopy," *The Journal of Physical Chemistry B*, vol. 110, no. 40, pp. 20038–20045, 2006.

[20] F. t. Zernike and J. Prins, "Die Beugung von Röntgenstrahlen in Flüssigkeiten als Effekt der Molekülanordnung," *Zeitschrift für Physik A Hadrons and nuclei*, vol. 41, no. 2-3, pp. 184–194, 1927.

[21] P. Debye and H. Menke, "The determination of the inner structure of liquids by X-ray means," *Phys Z*, vol. 31, pp. 797–798, 1930.

[22] M. W. Terban, E. Y. Cheung, P. Krolikowski, and S. J. Billinge, "Recrystallization, phase composition, and local structure of amorphous lactose from the total scattering pair distribution function," *Crystal Growth & Design*, vol. 16, no. 1, pp. 210–220, 2016.

[23] S. Banerjee, C.-H. Liu, J. D. Lee, A. Kovyakh, V. Grasmik, O. Prymak, C. Koenigsmann, H. Liu, L. Wang, A. M. Abeykoon, *et al.*, "Improved models for metallic nanoparticle cores from atomic pair distribution function (PDF) analysis," *The Journal of Physical Chemistry C*, vol. 122, no. 51, pp. 29498–29506, 2018.

[24] M. W. Terban, M. Johnson, M. Di Michiel, and S. J. Billinge, "Detection and characterization of nanoparticles in suspension at low concentrations using the X-ray total scattering pair distribution function technique," *Nanoscale*, vol. 7, no. 12, pp. 5480–5487, 2015.

[25] I. Halasz, S. A. Kimber, P. J. Beldon, A. M. Belenguer, F. Adams, V. Honkimäki, R. C. Nightingale, R. E. Dinnebier, and T. Friščić, "In situ and real-time monitoring of mechanochemical milling reactions using synchrotron X-ray diffraction," *Nature protocols*, vol. 8, no. 9, p. 1718, 2013.

[26] A. Westgren and A. E. Lindh, "Zum kristallbau des eisens und stahls," *Zeitschrift für Physikalische Chemie*, vol. 98, no. 1, pp. 181–210, 1921.

[27] A. L. Goodwin, M. Calleja, M. J. Conterio, M. T. Dove, J. S. Evans, D. A. Keen, L. Peters, and M. G. Tucker, "Colossal positive and negative thermal expansion in the framework material $Ag_3[Co(CN)_6]$," *Science*, vol. 319, no. 5864, pp. 794–797, 2008.

[28] Z.-S. Yao, H. Guan, Y. Shiota, C.-T. He, X.-L. Wang, S.-Q. Wu, X. Zheng, S.-Q. Su, K. Yoshizawa, X. Kong, *et al.*, "Giant anisotropic thermal expansion actuated by thermodynamically assisted reorientation of imidazoliums in a single crystal," *Nature communications*, vol. 10, no. 1, pp. 1–8, 2019.

[29] J. Chen, L. Hu, J. Deng, and X. Xing, "Negative thermal expansion in functional materials: controllable thermal expansion by chemical modifications," *Chemical Society Reviews*, vol. 44, no. 11, pp. 3522–3567, 2015.

[30] D. Das, T. Jacobs, and L. J. Barbour, "Exceptionally large positive and negative anisotropic thermal expansion of an organic crystalline material," *Nature materials*, vol. 9, no. 1, pp. 36–39, 2010.

[31] J. Becker, M. Bremholm, C. Tyrsted, B. Pauw, K. Jensen, J. Eltzholt, M. Christensen, and B. B. Iversen, "Experimental setup for in situ X-ray SAXS/WAXS/PDF studies of the formation and growth of nanoparticles in near-and supercritical fluids," *Journal of Applied Crystallography*, vol. 43, no. 4, pp. 729–736, 2010.

[32] P. Scherrer, "Bestimmung der inneren Struktur und der Größe von Kolloidteilchen mittels Röntgenstrahlen," in *Kolloidchemie Ein Lehrbuch*, pp. 387–409, 1912.

[33] A. Patterson, "The scherrer formula for X-ray particle size determination," *Physical review*, vol. 56, no. 10, p. 978, 1939.

[34] T. Egami and S. J. Billinge, *Underneath the Bragg peaks: structural analysis of complex materials*. Elsevier, 2003.

[35] B. E. Warren, "X-ray diffraction study of carbon black," *The journal of chemical physics*, vol. 2, no. 9, pp. 551–555, 1934.

[36] R. E. Franklin, "The interpretation of diffuse x-ray diagrams of carbon," *Acta crystallographica*, vol. 3, no. 2, pp. 107–121, 1950.

[37] S. Bates, G. Zografi, D. Engers, K. Morris, K. Crowley, and A. Newman, "Analysis of amorphous and nanocrystalline solids from their x-ray diffraction patterns," *Pharmaceutical research*, vol. 23, no. 10, pp. 2333–2349, 2006.

[38] M. W. Terban, R. Dabbous, A. D. Debellis, E. Pöselt, and S. J. Billinge, "Structures of hard phases in thermoplastic polyurethanes," *Macromolecules*, vol. 49, no. 19, pp. 7350–7358, 2016.

[39] K. Kodama, S. Iikubo, T. Taguchi, and S. i. Shamoto, "Finite size effects of nanoparticles on the atomic pair distribution functions," *Acta*

Crystallographica Section A: Foundations of Crystallography, vol. 62, no. 6, pp. 444–453, 2006.

[40] G. Pawley, "Unit-cell refinement from powder diffraction scans," *Journal of Applied Crystallography*, vol. 14, no. 6, pp. 357–361, 1981.

[41] A. Le Bail, H. Duroy, and J. L. Fourquet, "Ab-initio structure determination of LiSbWO6 by x-ray powder diffraction," *Materials Research Bulletin*, vol. 23, no. 3, pp. 447–452, 1988.

[42] R. E. Dinnebier, A. Leineweber, and J. S. Evans, *Rietveld refinement: practical powder diffraction pattern analysis using TOPAS*. Walter de Gruyter GmbH & Co KG, 2018.

[43] M. A. Banares, "Operando spectroscopy-preface," *Catalysis Today*, vol. 126, no. 1-2, pp. 1–2, 2007.

[44] B. M. Weckhuysen, "Snapshots of a working catalyst: possibilities and limitations of in situ spectroscopy in the field of heterogeneous catalysis," *Chemical Communications*, no. 2, pp. 97–110, 2002.

[45] G. Gallo, S. Bette, and R. E. Dinnebier, "Characterization and thermal behavior of the iron dietary supplement ferrous glycine sulfate pentahydrate," *Zeitschrift für anorganische und allgemeine Chemie*, vol. 645, no. 24, pp. 1350–1357, 2019.

[46] M. Gabrashanska, S. Tepavitcharova, C. Balarew, M. Galvez-Morros, and P. Arambarri, "The effect of excess dietary manganese on uninfected and ascaridia galli infected chicks," *Journal of Helminthology*, vol. 73, no. 4, p. 313–316, 1999.

[47] M. Gabrashanska, M. Y. Manga-Gonzalez, S. Ermidou-PoIIet, M. Anisimova, and S. Tepavitcharova, "Effect of $2\mathrm{GlyZnCl_2} \cdot 2\mathrm{H_2O}$ on antioxidant status in rats under fasciolosis," *Trace Elements and Electrolytes*, vol. 25, no. 4, pp. 199 – 205, 2008.

[48] M. Gabrashanska, S. Teodorova, M. Galvez-Morros, and M. Mitov, "Effects of glycine–metal compounds on Ascaridia galli-infected chickens expressed by a kinetic model," *Journal of Helminthology*, vol. 78, no. 1, p. 25–32, 2004.

[49] O. Pineda and H. D. Ashmead, "Effectiveness of treatment of iron-deficiency anemia in infants and young children with ferrous bis-glycinate chelate," *Nutrition*, vol. 17, pp. 381–384, 2001.

[50] L. H. Allen, "Iron supplements: Scientific issues concerning efficacy and implications for research and programs," *The Journal of Nutrition*, vol. 132, no. 4, pp. 813S–819S, 2002.

[51] C. Balarew, V. Spasov, and S. Tepavitcharova, "Pyro- and ferroelectric properties of $\mathrm{nGly/cdotMeCl_2 \cdot 2H_2O}$ (Me = Mn, Co; n = 1, 2)," *Ferroelectrics*, vol. 158, no. 1, pp. 157–162, 1994.

[52] Z. Weng, Z. Chen, and F. Liang, "Glycine-Templated Manganese Sulfate with New Topology and Canted Antiferromagnetism," *Inorganic Chemistry*, vol. 48, no. 18, pp. 8703–8708, 2009.

[53] P. Dhanaraj and N. Rajesh, "Studies on the growth and characterization of tris (glycine) calcium(II) dichloride - a non linear optical crystal," *Physica B: Condensed Matter*, vol. 406, no. 1, pp. 12 – 18, 2011.

[54] M. Esthaku Peter and P. Ramasamy, "Synthesis, growth and characterization of a novel semiorganic NLO crystal: Triglycine calcium dibromide," *Journal of Crystal Growth*, vol. 312, no. 12, pp. 1952 – 1956, 2010.

[55] S. Tepavitcharova, D. Rabadjieva, D. Havlíček, I. Němec, P. Vojtíšek, J. Plocek, and Z. Koleva, "Crystallization and characterization of the compounds $\mathrm{Gly \cdot MSO_4 \cdot mH_2O(M = Mg^{2+}, Mn^{2+}, Fe^{2+}, Co^{2+}, Ni^{2+}, Zn^{2+}; m = 0, 3, 5, 6)}$," *Journal of Molecular Structure*, vol. 1018, pp. 113 – 121, 2012.

[56] S. Bette, B. Hinrichsen, and R. E. Dinnebier, "On two glycine zinc sulfate phases with exotic cation coordination geometries," *Zeitschrift für anorganische und allgemeine Chemie*, vol. 643, no. 23, pp. 1855–1860, 2017.

[57] K. Alymkulova and K. Soleeva, "Koordinatsionnye soedinenija metallov s bioligandami," p. 77, 1987.

[58] R. E. Dinnebier, T. Runčevski, and B. Hinrichsen, "Crystal structure of the dietary supplement ferrous glycine sulfate," *Zeitschrift für anorganische und allgemeine Chemie*, vol. 642, no. 4, pp. 306–310, 2016.

[59] I. Lindqvist and R. Rosenstein, "The crystal structure of iron (II) sulphate pentahydrate glycine," 1960.

[60] S. Oguey, Y. Jacquier, A. Neels, and H. Stoeckli-Evans, "deposition number ccdc 936393," *CCDC, Union Road, Cambridge, England*, 2013.

[61] Z.-H. Zhang, Z. Han, X.-A. Zeng, and M.-S. Wang, "The preparation of Fe-glycine complexes by a novel method (pulsed electric fields)," *Food Chemistry*, vol. 219, pp. 468–476, 2017.

[62] D. Dodd, "Effects of X-irradiation on the near ultraviolet absorption spectrum of ferroelectric triglycine sulfate," *Spectrochimica Acta*, vol. 16, no. 4, pp. 413–418, 1960.

[63] S. Oguey, Y. Jacquier, A. Neels, and H. Stoeckli-Evans, "deposition number ccdc 936394," *CCDC, Union Road, Cambridge, England*, 2013.

[64] A. A. Coelho, "TOPAS and TOPAS-Academic: an optimization program integrating computer algebra and crystallographic objects written in C++," *Journal of Applied Crystallography*, vol. 51, no. 1, pp. 210–218, 2018.

[65] P. Roose, K. Eller, E. Henkes, R. Rossbacher, and H. Höke, "Amines, aliphatic," *Ullmann's Encyclopedia of Industrial Chemistry*, pp. 1–55, 2015.

[66] D. Ginsburg, *Concerning Amines: Their properties, preparation and reactions*. Elsevier, 2014.

[67] A. Butlerow, "Ueber ein neues methylenderivat," *Justus Liebigs Annalen der Chemie*, vol. 115, no. 3, pp. 322–327, 1860.

[68] E. Baur and W. Rüetschi, "Über bildung und zerfall von. hexamethylentetramin.," *Helvetica Chimica Acta*, vol. 24, pp. 754–767, 1941.

[69] O. Aschan *Berichte der Deutschen Chemischen Gesellschaft*, vol. 48, p. 874, 1915.

[70] E. Lund, "The structure of acetaldehyde-ammonia, and a note on its anhydrous form," 1951.

[71] P. Neelakantan, "The raman spectrum of cyclohexanol," in *Proceedings of the Indian Academy of Sciences-Section A*, vol. 57, pp. 94–102, 1963.

[72] T. Hirokawa, K. Ohno, T. Kimura, and H. Murata, "The vibrational spectra of α, β, and γ-picolines adsorbed on aerosil silica," *Chemistry Letters*, vol. 6, no. 5, pp. 457–460, 1977.

[73] Y. Kobayashi, H. Takahara, H. Takahashi, and K. Higasi, "Infiiared and raman studies of the structure of crystalline glygolaldehyde," *Journal of Molecular Structure*, vol. 32, no. 2, pp. 235–246, 1976.

[74] K. Dwarakanath and D. Sathyanarayana, "Vibrational spectra and assignments for the fundamental vibrations of imidazolidine-2-thione and-2-selenone," *Bulletin of the Chemical Society of Japan*, vol. 52, no. 9, pp. 2699–2704, 1979.

[75] S. Muthu and E. Isac Paulraj, "Molecular structure and spectroscopic characterization of ethyl 4-aminobenzoate with experimental techniques and DFT quantum chemical calculations," *Spectrochimica Acta Part A: Molecular and Biomolecular Spectroscopy*, vol. 112, pp. 169–181, 2013.

[76] S. Thomas, N. Biswas, S. Venkateswaran, S. Kapoor, R. D'Cunha, and T. Mukherjee, "Raman, infrared, SERS and DFT calculations of a triazole derivative (akacid)," *Chemical physics letters*, vol. 402, no. 4-6, pp. 361–366, 2005.

[77] A. T. Nielsen, R. L. Atkins, D. W. Moore, R. Scott, D. Mallory, and J. M. LaBerge, "Structure and chemistry of the aldehyde ammonias. 1-amino-1-alkanols, 2, 4, 6-trialkyl-1, 3, 5-hexahydrotriazines, and N, N-dialkylidene-1, 1-diaminoalkanes," *The Journal of Organic Chemistry*, vol. 38, no. 19, pp. 3288–3295, 1973.

[78] V. P. Tuguldurova, A. V. Fateev, V. S. Malkov, O. K. Poleshchuk, and O. V. Vodyankina, "Acetaldehyde–ammonia interaction: A DFT study of reaction mechanism and product identification," *The Journal of Physical Chemistry A*, vol. 121, no. 16, pp. 3136–3141, 2017.

[79] M. A. Fox and J. K. Whitesell, *Organische Chemie: Grundlagen, Mechanismen, Bioorganische Anwendungen*. Spektrum Akad. Verlag, 1995.

[80] C. F. Macrae, I. Sovago, S. J. Cottrell, P. T. Galek, P. McCabe, E. Pidcock, M. Platings, G. P. Shields, J. S. Stevens, M. Towler, *et al.*, "Mercury 4.0: from visualization to analysis, design and prediction," *Journal of Applied Crystallography*, vol. 53, no. 1, pp. 226–235, 2020.

[81] D. J. Nelson and C. N. Brammer, "Toward consistent terminology for cyclohexane conformers in introductory organic chemistry," *Journal of Chemical Education*, vol. 88, no. 3, pp. 292–294, 2011.

[82] S. Palacin, D. N. Chin, E. E. Simanek, J. C. MacDonald, G. M. Whitesides, M. T. McBride, and G. T. R. Palmore, "Hydrogen-bonded tapes based on symmetrically substituted diketopiperazines: a robust structural motif for the engineering of molecular solids," *Journal of the American Chemical Society*, vol. 119, no. 49, pp. 11807–11816, 1997.

[83] J. D. Hoeschele, H. H. Showalter, A. J. Kraker, W. L. Elliott, B. J. Roberts, and J. W. Kampf, "Synthesis, structural characterization, and antitumor properties of a novel class of large-ring platinum (ii) chelate complexes incorporating the cis-1, 4-diaminocyclohexane ligand in a unique locked boat conformation," *Journal of medicinal chemistry*, vol. 37, no. 17, pp. 2630–2636, 1994.

[84] P. Debye, "Dispersion of roentgen rays," *Ann. Phys*, vol. 46, no. 809, p. 21, 1915.

[85] S. Billinge, "Nanometre-scale structure from powder diffraction: total scattering and atomic pair distribution function analysis," 2019.

[86] I.-K. Jeong, T. Proffen, F. Mohiuddin-Jacobs, and S. J. Billinge, "Measuring correlated atomic motion using X-ray diffraction," *The Journal of Physical Chemistry A*, vol. 103, no. 7, pp. 921–924, 1999.

[87] D. Prill, P. Juhás, M. U. Schmidt, and S. J. Billinge, "Modelling pair distribution functions (PDFs) of organic compounds: describing both intra-and intermolecular correlation functions in calculated PDFs," *Journal of Applied Crystallography*, vol. 48, no. 1, pp. 171–178, 2015.

[88] M. W. Terban, L. Russo, T. N. Pham, D. H. Barich, Y. T. Sun, M. D. Burke, J. Brum, and S. J. Billinge, "Local structural effects due to micronization and amorphization on an HIV treatment active pharmaceutical ingredient," *Molecular Pharmaceutics*, 2020.

[89] A. Hammersley, S. Svensson, M. Hanfland, A. Fitch, and D. Hausermann, "Two-dimensional detector software: from real detector to idealised image or two-theta scan," *International Journal of High Pressure Research*, vol. 14, no. 4-6, pp. 235–248, 1996.

[90] X. Yang, P. Juhas, C. L. Farrow, and S. J. Billinge, "xpdfsuite: an end-to-end software solution for high throughput pair distribution function transformation, visualization and analysis," *arXiv preprint arXiv:1402.3163*, 2014.

[91] Z. Liu, Q. Gao, J. Chen, J. Deng, K. Lin, and X. Xing, "Negative thermal expansion in molecular materials," *Chemical Communications*, vol. 54, no. 41, pp. 5164–5176, 2018.

[92] K. Röttger, A. Endriss, J. Ihringer, S. Doyle, and W. F. Kuhs, "Lattice constants and thermal expansion of H_2O and D_2O ice I*h* between 10 and 265 K," *Acta Crystallographica Section B*, vol. 50, pp. 644–648, Dec 1994.

[93] R. K. Das, H. Aggarwal, and L. J. Barbour, "Anomalous anisotropic thermal expansion in a one-dimensional coordination polymer driven by conformational flexibility," *Inorganic chemistry*, vol. 54, no. 17, pp. 8171–8173, 2015.

[94] C. S. Haines, M. D. Lima, N. Li, G. M. Spinks, J. Foroughi, J. D. Madden, S. H. Kim, S. Fang, M. J. De Andrade, F. Göktepe, *et al.*, "Artificial muscles from fishing line and sewing thread," *science*, vol. 343, no. 6173, pp. 868–872, 2014.

[95] Y. H. Bae, T. Okano, R. Hsu, and S. W. Kim, "Thermo-sensitive polymers as on-off switches for drug release," *Die Makromolekulare Chemie, Rapid Communications*, vol. 8, no. 10, pp. 481–485, 1987.

[96] X. Shen, C. Viney, E. R. Johnson, C. Wang, and J. Q. Lu, "Large negative thermal expansion of a polymer driven by a submolecular conformational change," *Nature chemistry*, vol. 5, no. 12, p. 1035, 2013.

[97] I. d. de Pedro, A. Garcia-Saiz, J. Dupont, P. Migowski, O. Vallcorba, J. Junquera, J. Rius, and J. Rodriguez Fernandez, "On the colossal and highly anisotropic thermal expansion exhibited by imidazolium salts," *Crystal Growth and Design*, vol. 15, no. 11, pp. 5207–5212, 2015.

[98] Y. Kim, R. Haldar, H. Kim, J. Koo, and K. Kim, "The guest-dependent thermal response of the flexible mof zn 2 (bdc) 2 (dabco)," *Dalton Transactions*, vol. 45, no. 10, pp. 4187–4192, 2016.

[99] E. R. Engel, V. J. Smith, C. X. Bezuidenhout, and L. J. Barbour, "Uniaxial negative thermal expansion facilitated by weak host-guest interactions," *Chemical Communications*, vol. 50, no. 32, pp. 4238–4241, 2014.

[100] Z. Liu, C. Liu, Q. Li, J. Chen, and X. Xing, "Spring-like motion caused large anisotropic thermal expansion in nonporous M (eim) 2 (M= Zn, Cd)," *Physical Chemistry Chemical Physics*, vol. 19, no. 36, pp. 24436–24439, 2017.

[101] R. H. Baughman, S. Stafström, C. Cui, and S. O. Dantas, "Materials with negative compressibilities in one or more dimensions," *Science*, vol. 279, no. 5356, pp. 1522–1524, 1998.

[102] F. M. Mulder, B. Assfour, J. Huot, T. J. Dingemans, M. Wagemaker, and A. Ramirez-Cuesta, "Hydrogen in the metal- organic framework cr mil-53," *The Journal of Physical Chemistry C*, vol. 114, no. 23, pp. 10648–10655, 2010.

[103] M. J. Cliffe and A. L. Goodwin, "Pascal: a principal axis strain calculator for thermal expansion and compressibility determination," *Journal of Applied Crystallography*, vol. 45, no. 6, pp. 1321–1329, 2012.

[104] K. Yadava, G. Gallo, S. Bette, C. E. Mulijanto, D. P. Karothu, I.-H. Park, R. Medishetty, P. Naumov, R. E. Dinnebier, and J. J. Vittal, "Extraordinary anisotropic thermal expansion in photosalient crystals," *IUCrJ*, vol. 7, pp. 83–89, Jan 2020.

[105] P. Naumov, S. Chizhik, M. K. Panda, N. K. Nath, and E. Boldyreva, "Mechanically responsive molecular crystals," *Chemical Reviews*, vol. 115, pp. 12440–12490, 2015.

[106] O. S. Bushuyev, T. C. Corkery, C. J. Barrett, and T. Friščić, "Photomechanical azobenzene cocrystals and in situ x-ray diffraction monitoring of their optically-induced crystal-to-crystal isomerisation," *Chemical Science*, vol. 5, no. 8, pp. 3158–3164, 2014.

[107] N. K. Nath, M. K. Panda, S. C. Sahoo, and P. Naumov, "Thermally induced and photoinduced mechanical effects in molecular single crystals—a revival," *CrystEngComm*, vol. 16, no. 10, pp. 1850–1858, 2014.

[108] M. Lusi and J. Bernstein, "On the propulsion mechanism of "jumping" crystals," *Chemical Communications*, vol. 49, no. 81, pp. 9293–9295, 2013.

[109] R. Medishetty, A. Husain, Z. Bai, T. Runčevski, R. E. Dinnebier, P. Naumov, and J. J. Vittal, "Single crystals popping under uv light: A photosalient effect triggered by a [2+ 2] cycloaddition reaction," *Angewandte Chemie International Edition*, vol. 53, no. 23, pp. 5907–5911, 2014.

[110] M. K. Panda, T. Runčevski, S. C. Sahoo, A. A. Belik, N. K. Nath, R. E. Dinnebier, and P. Naumov, "Colossal positive and negative thermal expansion and thermosalient effect in a pentamorphic organometallic martensite," *Nature communications*, vol. 5, no. 1, pp. 1–8, 2014.

[111] G. Schmidt, "Photodimerization in the solid state," *Pure and Applied Chemistry*, vol. 27, no. 4, pp. 647–678, 1971.

[112] A. J. Brock, J. J. Whittaker, J. A. Powell, M. C. Pfrunder, A. Grosjean, S. Parsons, J. C. McMurtrie, and J. K. Clegg, "Elastically flexible crystals have disparate mechanisms of molecular movement induced

by strain and heat," *Angewandte Chemie International Edition*, vol. 57, no. 35, pp. 11325–11328, 2018.

[113] Z. Chen, G. Gallo, V. A. Sawant, T. Zhang, M. Zhu, L. Liang, A. Chanthapally, G. Bolla, H. S. Quah, X. Liu, K. P. Loh, R. E. Dinnebier, Q.-H. Xu, and J. J. Vittal, "Giant enhancement of second harmonic generation accompanied by the structural transformation of 7-Fold to 8-Fold Interpenetrated Metal–Organic Frameworks (MOFs)," *Angewandte Chemie International Edition*, vol. 59, no. 2, pp. 833–838, 2020.

[114] S. L. James, "Metal-organic frameworks," *Chemical Society Reviews*, vol. 32, no. 5, pp. 276–288, 2003.

[115] J. L. Rowsell and O. M. Yaghi, "Metal-organic frameworks: a new class of porous materials," *Microporous and mesoporous materials*, vol. 73, no. 1-2, pp. 3–14, 2004.

[116] O. M. Yaghi, G. Li, and H. Li, "Selective binding and removal of guests in a microporous metal-organic framework," *Nature*, vol. 378, no. 6558, pp. 703–706, 1995.

[117] J. Lee, O. K. Farha, J. Roberts, K. A. Scheidt, S. T. Nguyen, and J. T. Hupp, "Metal-organic framework materials as catalysts," *Chemical Society Reviews*, vol. 38, no. 5, pp. 1450–1459, 2009.

[118] H. K. Chae, D. Y. Siberio-Perez, J. Kim, Y. Go, M. Eddaoudi, A. J. Matzger, M. O'Keeffe, and O. M. Yaghi, "A route to high surface area, porosity and inclusion of large molecules in crystals," *Nature*, vol. 427, no. 6974, pp. 523–527, 2004.

[119] M. Zhang, B. Li, Y. Li, Q. Wang, W. Zhang, B. Chen, S. Li, Y. Pan, X. You, and J. Bai, "Finely tuning mofs towards high performance in c 2 h 2 storage: synthesis and properties of a new mof-505 analogue with an inserted amide functional group," *Chemical Communications*, vol. 52, no. 45, pp. 7241–7244, 2016.

[120] H. Li, M. Eddaoudi, M. O'Keeffe, and O. M. Yaghi, "Design and synthesis of an exceptionally stable and highly porous metal-organic framework," *nature*, vol. 402, no. 6759, pp. 276–279, 1999.

[121] S. R. Batten and R. Robson, "Interpenetrating nets: ordered, periodic entanglement," *Angewandte Chemie International Edition*, vol. 37, no. 11, pp. 1460–1494, 1998.

[122] L. Carlucci, G. Ciani, and D. M. Proserpio, "Polycatenation, polythreading and polyknotting in coordination network chemistry," *Coordination Chemistry Reviews*, vol. 246, no. 1-2, pp. 247–289, 2003.

[123] H. Wu, J. Yang, Z.-M. Su, S. R. Batten, and J.-F. Ma, "An exceptional 54-fold interpenetrated coordination polymer with 103-srs network topology," *Journal of the American Chemical Society*, vol. 133, no. 30, pp. 11406–11409, 2011.

[124] J. Zhang, L. Wojtas, R. W. Larsen, M. Eddaoudi, and M. J. Zaworotko, "Temperature and concentration control over interpenetration in a metal-organic material," *Journal of the American Chemical Society*, vol. 131, no. 47, pp. 17040–17041, 2009.

[125] O. Shekhah, H. Wang, M. Paradinas, C. Ocal, B. Schüpbach, A. Terfort, D. Zacher, R. A. Fischer, and C. Wöll, "Controlling interpenetration in metal-organic frameworks by liquid-phase epitaxy," *Nature materials*, vol. 8, no. 6, pp. 481–484, 2009.

[126] H. Aggarwal, P. Lama, and L. J. Barbour, "Transformation from non-to double-interpenetration in robust cd (II) doubly-pillared-layered metal-organic frameworks," *Chemical Communications*, vol. 50, no. 93, pp. 14543–14546, 2014.

[127] S. B. Choi, H. Furukawa, H. J. Nam, D.-Y. Jung, Y. H. Jhon, A. Walton, D. Book, M. O'Keeffe, O. M. Yaghi, and J. Kim, "Reversible interpenetration in a metal-organic framework triggered by ligand removal and

addition," *Angewandte Chemie International Edition*, vol. 51, no. 35, pp. 8791–8795, 2012.

[128] H. Aggarwal, P. M. Bhatt, C. X. Bezuidenhout, and L. J. Barbour, "Direct evidence for single-crystal to single-crystal switching of degree of interpenetration in a metal-organic framework," *Journal of the American Chemical Society*, vol. 136, no. 10, pp. 3776–3779, 2014.

[129] D. Dini, M. J. Calvete, and M. Hanack, "Nonlinear optical materials for the smart filtering of optical radiation," *Chemical reviews*, vol. 116, no. 22, pp. 13043–13233, 2016.

[130] L. Mingabudinova, V. Vinogradov, V. Milichko, E. Hey-Hawkins, and A. Vinogradov, "Metal-organic frameworks as competitive materials for non-linear optics," *Chemical Society Reviews*, vol. 45, no. 19, pp. 5408–5431, 2016.

[131] A. Cronstedt, "Natural zeolite and minerals," *Svenska Vetenskaps Akademiens Handlingar Stockholm*, vol. 17, p. 120, 1756.

[132] Y. Zheng, X. Li, and P. K. Dutta, "Exploitation of unique properties of zeolites in the development of gas sensors," *Sensors*, vol. 12, no. 4, pp. 5170–5194, 2012.

[133] D. W. Breck, *Zeolite molecular sieves: structure, chemistry and use*. Krieger, 1984.

[134] D. Papaioannou, P.-D. Katsoulos, N. Panousis, and H. Karatzias, "The role of natural and synthetic zeolites as feed additives on the prevention and/or the treatment of certain farm animal diseases: A review," *Microporous and mesoporous materials*, vol. 84, no. 1-3, pp. 161–170, 2005.

[135] M. Álvaro, J. F. Cabeza, D. Fabuel, H. García, E. Guijarro, and J. L. Martínez de Juan, "Electrical conductivity of zeolite films: Influence of charge balancing cations and crystal structure," *Chemistry of materials*, vol. 18, no. 1, pp. 26–33, 2006.

[136] M. Franus, M. Wdowin, L. Bandura, and W. Franus, "Removal of environmental pollutions using zeolites from fly ash: A review," *Fresenius Environ. Bull*, vol. 24, pp. 854–866, 2015.

[137] "Zeolites marketing research report in chemical economics handbook," *IHS*, 2016.

[138] E. Passaglia and G. Vezzalini, "Crystal chemistry of diagenetic zeolites in volcanoclastic deposits of italy," *Contributions to Mineralogy and Petrology*, vol. 90, no. 2-3, pp. 190–198, 1985.

[139] C. S. Cundy and P. A. Cox, "The hydrothermal synthesis of zeolites: Precursors, intermediates and reaction mechanism," *Microporous and mesoporous materials*, vol. 82, no. 1-2, pp. 1–78, 2005.

[140] Q. Sun, N. Wang, G. Guo, and J. Yu, "Ultrafast synthesis of nano-sized zeolite sapo-34 with excellent mto catalytic performance," *Chemical Communications*, vol. 51, no. 91, pp. 16397–16400, 2015.

[141] Z. Liu, J. Zhu, T. Wakihara, and T. Okubo, "Ultrafast synthesis of zeolites: breakthrough, progress and perspective," *Inorganic Chemistry Frontiers*, vol. 6, no. 1, pp. 14–31, 2019.

[142] J. H. Kwak, R. G. Tonkyn, D. H. Kim, J. Szanyi, and C. H. Peden, "Excellent activity and selectivity of Cu-SSZ-13 in the selective catalytic reduction of NO_x with NH_3," *Journal of Catalysis*, vol. 275, no. 2, pp. 187–190, 2010.

[143] G. Gallo, A. Mihanović, I. Rončević, R. Dinnebier, and H. Vančik, "Crystal structure and ON-OFF polymerization mechanism of Poly(1,4-phenyleneazine-N,N-dioxide), a possible wide bandgap semiconductor," *Polymer*, p. 123235, 2020.

[144] H. Vančik, *Aromatic C-nitroso compounds*. Springer, 2013.

[145] D. Beaudoin and J. D. Wuest, "Dimerization of aromatic c-nitroso compounds," *Chemical reviews*, vol. 116, no. 1, pp. 258–286, 2016.

[146] Y. Yamamoto and H. Yamamoto, "Recent advances in asymmetric nitroso Diels-Alder reactions," *European journal of organic chemistry*, vol. 2006, no. 9, pp. 2031–2043, 2006.

[147] S. Carosso and M. J. Miller, "Nitroso diels-alder (NDA) reaction as an efficient tool for the functionalization of diene-containing natural products," *Organic & biomolecular chemistry*, vol. 12, no. 38, pp. 7445–7468, 2014.

[148] L. Peng and R. J. Turesky, "Optimizing proteolytic digestion conditions for the analysis of serum albumin adducts of 2-amino-1-methyl-6-phenylimidazo [4, 5-b] pyridine, a potential human carcinogen formed in cooked meat," *Journal of proteomics*, vol. 103, pp. 267–278, 2014.

[149] C. Trefzer, M. Rengifo-Gonzalez, M. J. Hinner, P. Schneider, V. Makarov, S. T. Cole, and K. Johnsson, "Benzothiazinones: prodrugs that covalently modify the decaprenylphosphoryl-β-D-ribose 2'-epimerase DprE1 of Mycobacterium tuberculosis," *Journal of the American Chemical Society*, vol. 132, no. 39, pp. 13663–13665, 2010.

[150] C. L. Hawkins and M. J. Davies, "Detection and characterisation of radicals in biological materials using EPR methodology," *Biochimica et Biophysica Acta (BBA)-General Subjects*, vol. 1840, no. 2, pp. 708–721, 2014.

[151] C. L. Hawkins *et al.*, "EPR spin trapping of protein radicals," *Free Radical Biology and Medicine*, vol. 36, no. 9, pp. 1072–1086, 2004.

[152] H. Vancik, V. Šimunić-Mežnarić, I. Ćaleta, E. Meštrović, S. Milovac, K. Mlinarić-Majerski, and J. Veljković, "Solid State Photochromism and Thermochromism in Nitroso Monomer-Dimer Equilibrium," *The Journal of Physical Chemistry B*, vol. 106, no. 7, pp. 1576–1580, 2002.

[153] L. Anderson, M. Cameron, B. G. Gowenlock, and I. J. McEwen, "Properties and spectroscopic studies of polymeric dinitrosobenzenes,"

Journal of the Chemical Society, Perkin Transactions 2, no. 2, pp. 243–245, 1992.

[154] N. P. Hacker, "Investigation of the polymerization of 1, 4-dinitrosobenzene by low-temperature infrared and UV absorption spectroscopy," *Macromolecules*, vol. 26, no. 22, pp. 5937–5942, 1993.

[155] T. H. Baum, C. E. Larson, and N. P. Hacker, "Poly (1, 4-phenyleneazine N, N-dioxide): a recyclable material for a solventless laser-imageable resist process," *Chemistry of materials*, vol. 6, no. 11, pp. 1978–1981, 1994.

[156] P. Bibulić, I. Rončević, K. Varga, Z. Mihalić, and H. Vančik, "Structure and topochemistry of azodioxide oligomers in solid state," *Journal of Molecular Structure*, vol. 1104, pp. 85–90, 2016.

[157] P. Bibulic, I. Roncevic, V. Bermanec, and H. Vancik, "Polymerization of 1, 4-dinitrosobenzene: Kinetics and submicrocrystal structure," *Croatica Chemica Acta*, vol. 90, no. 3, pp. 383–390, 2017.

[158] I. Halasz, E. Mestrovic, H. Cicak, Z. Mihalic, and H. Vancik, "Solid-State Reaction Mechanisms in Monomer-Dimer interconversions of p-Bromonitrosobenzene. single-Crystal-to-Single-Crystal Photodissociation and Formation of New Non-van der Waals Close Contacts," *The Journal of organic chemistry*, vol. 70, no. 21, pp. 8461–8467, 2005.

[159] C. Wechwithayakhlung, D. M. Packwood, J. Chaopaknam, P. Worakajit, S. Ittisanronnachai, N. Chanlek, V. Promarak, K. Kongpatpanich, D. J. Harding, and P. Pattanasattayavong, "Tin (II) thiocyanate Sn (NCS) 2–a wide band gap coordination polymer semiconductor with a 2D structure," *Journal of Materials Chemistry C*, vol. 7, no. 12, pp. 3452–3462, 2019.

[160] D. Yang and D. Ma, "Development of organic semiconductor photodetectors: from mechanism to applications," *Advanced Optical Materials*, vol. 7, no. 1, p. 1800522, 2019.

[161] Y. Ma, Z. Kang, and Q. Zheng, "Recent advances in wide bandgap semiconducting polymers for polymer solar cells," *Journal of Materials Chemistry A*, vol. 5, no. 5, pp. 1860–1872, 2017.

[162] P. W. Stephens, "Phenomenological model of anisotropic peak broadening in powder diffraction," *Journal of Applied Crystallography*, vol. 32, no. 2, pp. 281–289, 1999.

[163] B. Warren, "X-ray diffraction in random layer lattices," *Physical Review*, vol. 59, no. 9, p. 693, 1941.

[164] T. Welberry and B. Butler, "Interpretation of diffuse X-ray scattering via models of disorder," *Journal of applied crystallography*, vol. 27, no. 3, pp. 205–231, 1994.

[165] A. Jochim, G. Gallo, R. Dinnebier, and C. Näther, "Synthesis, crystal structure and properties of $Cd(NCS)_2$ coordination compounds with two different cd coordination modes," *Zeitschrift für Naturforschung B*, vol. 74, no. 1, pp. 49–58, 2019.

[166] T. Neumann, G. Gallo, I. Jess, R. E. Dinnebier, and C. Näther, "Thermodynamically stable and metastable coordination polymers synthesized from solution and the solid state," *CrystEngComm*, vol. 22, no. 2, pp. 184–194, 2020.

[167] C. Wellm, T. Neumann, M. Ceglarska, G. Gallo, M. Rams, R. E. Dinnebier, and C. Näther, "New isomeric $Ni(NCS)_2$ coordination compounds: crystal structures, magnetic properties as well as ex situ and in situ investigations on their synthesis and transition behaviour," *CrystEngComm*, vol. 22, no. 13, pp. 2350–2360, 2020.

[168] T. Neumann, G. Gallo, R. E. Dinnebier, and C. Näther, "Synthesis, crystal structures, and properties of Mn $(NCS)_2$ coordination compounds with 4-picoline as coligand and crystal structure of Mn $(NCS)_2$," *Zeitschrift für anorganische und allgemeine Chemie*, vol. 646, no. 3, pp. 88–94, 2020.

[169] C. Wellm, T. Neumann, G. Gallo, A. M. Dziubyna, M. Rams, R. E. Dinnebier, and C. Näther, "Structural variety in Mn $(NCS)_2$ 4-cyanopyridine coordination compounds: Synthesis, structures, isomerism, and magnetic properties," *Crystal Growth & Design*, vol. 20, no. 5, pp. 3374–3385, 2020.

[170] I. Jess, T. Neumann, H. Terraschke, G. Gallo, R. Dinnebier, and C. Näther, "Synthesis, structures, thermal and luminescence properties of Zn and Cd halide coordination polymers with 2-cyanopyrazine," *Zeitschrift für anorganische und allgemeine Chemie*, 2020.

[171] A. Norbury, "Coordination chemistry of the cyanate, thiocyanate, and selenocyanate ions," in *Advances in inorganic chemistry and radiochemistry*, vol. 17, pp. 231–386, Elsevier, 1975.

[172] M. Kabešová, R. Boča, M. Melník, D. Valigura, and M. Dunaj-Jurčo, "Bonding properties of thiocyanate groups in copper (ii) and copper (i) complexes," *Coordination chemistry reviews*, vol. 140, pp. 115–135, 1995.

[173] D. Buckingham, "The linkage isomerism of thiocyanate bonded to cobalt (iii)," *Coordination Chemistry Reviews*, vol. 135, pp. 587–621, 1994.

[174] K. Müller-Buschbaum, "The utilization of solid state chemistry reaction routes as new syntheses strategies for the coordination chemistry of rare earth amides," *Zeitschrift für anorganische und allgemeine Chemie*, vol. 631, no. 5, pp. 811–828, 2005.

[175] C. J. Hoeller and K. Mueller-Buschbaum, "The first dinitrile frameworks of the rare earth elements: infinity (3)[LnCl3 (1, 4-Ph (CN) 2)] and infinity (3)[Ln2Cl6 (1, 4-Ph (CN) 2)], Ln= Sm, Gd, Tb, Y; access to novel metal-organic frameworks by solvent free synthesis in molten 1, 4-benzodinitrile.," *Inorganic chemistry*, vol. 47, no. 21, pp. 10141–10149, 2008.

[176] A. Zurawski, J.-C. Rybak, L. V. Meyer, P. R. Matthes, V. Stepanenko, N. Dannenbauer, F. Würthner, and K. Müller-Buschbaum, "Alkaline earth imidazolate coordination polymers by solvent free melt synthesis as potential host lattices for rare earth photoluminescence: x=[AE (Im) 2 (ImH) 2–3], Mg, Ca, Sr, Ba, x= 1–2," *Dalton Transactions*, vol. 41, no. 14, pp. 4067–4078, 2012.

[177] D. Braga, M. Curzi, F. Grepioni, and M. Polito, "Mechanochemical and solution reactions between AgCH 3 COO and [H 2 NC 6 H 10 NH 2] yield three isomers of the coordination network {Ag [H 2 NC 6 H 10 NH 2]+}," *Chemical Communications*, no. 23, pp. 2915–2917, 2005.

[178] J.-L. Do and T. Friščić, "Mechanochemistry: a force of synthesis," *ACS central science*, vol. 3, no. 1, pp. 13–19, 2017.

[179] A. D. Katsenis, A. Puškarić, V. Štrukil, C. Mottillo, P. A. Julien, K. Užarević, M.-H. Pham, T.-O. Do, S. A. Kimber, P. Lazić, *et al.*, "In situ X-ray diffraction monitoring of a mechanochemical reaction reveals a unique topology metal-organic framework," *Nature communications*, vol. 6, no. 1, pp. 1–8, 2015.

[180] H. Ohtsu and M. Kawano, "Kinetic assembly of coordination networks," *Chemical Communications*, vol. 53, no. 63, pp. 8818–8829, 2017.

[181] T. Neumann, M. Ceglarska, L. S. Germann, M. Rams, R. E. Dinnebier, S. Suckert, I. Jess, and C. Näther, "Structures, thermodynamic relations, and magnetism of stable and metastable Ni (NCS) 2 coordination polymers," *Inorganic chemistry*, vol. 57, no. 6, pp. 3305–3314, 2018.

[182] S. Wöhlert, T. Runčevski, R. E. Dinnebier, S. G. Ebbinghaus, and C. Näther, "Synthesis, structures, polymorphism, and magnetic properties of transition metal thiocyanato coordination compounds," *Crystal growth & design*, vol. 14, no. 4, pp. 1902–1913, 2014.

[183] H.-Y. Bie, J.-H. Yu, J.-Q. Xu, J. Lu, Y. Li, X.-B. Cui, X. Zhang, Y.-H. Sun, and L.-Y. Pan, "Synthesis, structure and non-linear optical property of a copper (II) thiocyanate three-dimensional supramolecular compound," *Journal of molecular structure*, vol. 660, no. 1-3, pp. 107–112, 2003.

[184] C. Näther, J. Greve, I. Jeß, and C. Wickleder, "Copper (I) thiocyanate coordination polymers with dimethylpyrazine: synthesis, crystal structures, thermal and luminescence properties," *Solid state sciences*, vol. 5, no. 8, pp. 1167–1176, 2003.

[185] D.-B. Dang, W.-L. Shang, Y. Bai, J.-D. Sun, and H. Gao, "Synthesis, crystal structure and luminescent properties of two cadmium thiocyanate coordination polymers with benzylpyridyl cations," *Inorganica Chimica Acta*, vol. 362, no. 7, pp. 2391–2395, 2009.

[186] S.-W. Liang, M.-X. Li, M. Shao, and X. He, "Synthesis, crystal structure and fluorescent property of two-dimensional cu (i) coordination polymers with cyanide, thiocyanate and triazole bridges," *Journal of Molecular Structure*, vol. 875, no. 1-3, pp. 17–21, 2008.

[187] H.-Y. Bie, J. Lu, J.-H. Yu, J.-Q. Xu, K. Zhao, and X. Zhang, "Syntheses of fluorescent thiocyanate supramolecular compounds with unusual two-dimensional structures," *Journal of Solid State Chemistry*, vol. 178, no. 5, pp. 1445–1451, 2005.

[188] J. D. Harris, W. E. Eckles, A. F. Hepp, S. A. Duraj, P. E. Fanwick, J. Richardson, and E. M. Gordon, "Room temperature dissolution of

metal powders by thiourea: a novel route to transition metal isothiocyanate complexes," *Materials & Design*, vol. 22, no. 7, pp. 625–634, 2001.

[189] J. D. Harris, W. E. Eckles, A. F. Hepp, S. A. Duraj, and P. E. Fanwick, "Synthesis and characterization of anionic transition metal isothiocyanate complexes prepared from metal powders and thiourea," *Inorganica Chimica Acta*, vol. 338, pp. 99–104, 2002.

[190] M. Taniguchi, M. Shimoi, and A. Ouchi, "The crystal and molecular structure of bis (4-methylpyridine) bis (thiocyanato) cadmium (II) in polymeric form,[Cd (SCN) 2 (CH3C5H4N) 2] n," *Bulletin of the Chemical Society of Japan*, vol. 59, no. 7, pp. 2299–2302, 1986.

[191] R. E. Marsh, "Some thoughts on choosing the correct space group," *Acta Crystallographica Section B: Structural Science*, vol. 51, no. 6, pp. 897–907, 1995.

[192] B. Machura, A. Świtlicka, J. Mroziński, B. Kalińska, and R. Kruszynski, "Structural diversity and magnetic properties of thiocyanate copper (II) complexes," *Polyhedron*, vol. 52, pp. 1276–1286, 2013.

[193] S. Wöhlert, I. Jess, and C. Näther, "New coordination compounds based on $Cd(NCS)_2(4\text{-ethylpyridine})_x$ (x= 4, 2, 1)," *Zeitschrift für anorganische und allgemeine Chemie*, vol. 639, no. 2, pp. 385–391, 2013.

[194] S. Wöhlert, J. Boeckmann, I. Jess, and C. Näther, "Synthesis of new stable and metastable thiocyanato coordination polymers by thermal decomposition and by solution reactions," *CrystEngComm*, vol. 14, no. 17, pp. 5412–5420, 2012.

[195] E. Ďurčanská, M. Jamnickỳ, M. Koman, I. Wnęk, and T. Głowiak, "Structural investigations of Ni(II) complexes. VI. two isomers of

tetrakis (3-ethylpyridine) bis (isothiocyanato) nickel (II)," *Acta Crystallographica Section C: Crystal Structure Communications*, vol. 42, no. 9, pp. 1157–1159, 1986.

[196] J. D. Harris, W. E. Eckles, A. F. Hepp, S. A. Duraj, D. G. Hehemann, P. E. Fanwick, and J. Richardson, "Novel route to transition metal isothiocyanate complexes using metal powders and thiourea," *Acta Crystallographica Section C: Crystal Structure Communications*, 2003.

[197] S. Suckert, M. Rams, L. S. Germann, D. M. Cegiełka, R. E. Dinnebier, and C. Näther, "Thermal transformation of a Zero-Dimensional thiocyanate precursor into a ferromagnetic Three-Dimensional coordination network via a layered intermediate," *Crystal Growth & Design*, vol. 17, no. 7, pp. 3997–4005, 2017.

[198] Y. Wu, A. Kobayashi, G. J. Halder, V. K. Peterson, K. W. Chapman, N. Lock, P. D. Southon, and C. J. Kepert, "Negative thermal expansion in the Metal-Organic Framework material Cu_3 (1, 3, 5-benzenetricarboxylate)$_2$," *Angewandte Chemie International Edition*, vol. 47, no. 46, pp. 8929–8932, 2008.

[199] C. Yang, X. Wang, and M. A. Omary, "Crystallographic observation of dynamic gas adsorption sites and thermal expansion in a breathable fluorous Metal-Organic Framework," *Angewandte Chemie International Edition*, vol. 48, no. 14, pp. 2500–2505, 2009.

[200] H.-L. Zhou, Y.-B. Zhang, J.-P. Zhang, and X.-M. Chen, "Supramolecular-jack-like guest in ultramicroporous crystal for exceptional thermal expansion behaviour," *Nature communications*, vol. 6, no. 1, pp. 1–7, 2015.

[201] B. Dwivedi, A. Shrivastava, L. Negi, and D. Das, "Colossal positive and negative axial thermal expansion induced by scissor-like motion

of a two-dimensional hydrogen bonded network in an organic salt," *Crystal Growth & Design*, vol. 19, no. 5, pp. 2519–2524, 2019.

[202] L. O. Alimi, P. Lama, V. J. Smith, and L. J. Barbour, "Large volumetric thermal expansion of a novel organic cocrystal over a wide temperature range," *CrystEngComm*, vol. 20, no. 5, pp. 631–635, 2018.

[203] S. Bhattacharya and B. K. Saha, "Interaction dependence and similarity in thermal expansion of a dimorphic 1d hydrogen-bonded organic complex," *Crystal growth & design*, vol. 13, no. 8, pp. 3299–3302, 2013.

[204] K. M. Hutchins, R. H. Groeneman, E. W. Reinheimer, D. C. Swenson, and L. R. MacGillivray, "Achieving dynamic behaviour and thermal expansion in the organic solid state via co-crystallization," *Chemical science*, vol. 6, no. 8, pp. 4717–4722, 2015.

[205] K. M. Hutchins, K. A. Kummer, R. H. Groeneman, E. W. Reinheimer, M. A. Sinnwell, D. C. Swenson, and L. R. MacGillivray, "Thermal expansion properties of three isostructural co-crystals composed of isosteric components: interplay between halogen and hydrogen bonds," *CrystEngComm*, vol. 18, no. 43, pp. 8354–8357, 2016.